Enabling Technologies for Functional Optical Coherence Tomography in Retinal Disease

by

ByungKun Lee

B. S. in Electrical Science and Engineering and in Mathematics
Massachusetts Institute of Technology, June 2011

M. Eng. in Electrical Engineering and Computer Science
Massachusetts Institute of Technology, June 2012

Submitted to the
DEPARTMENT OF ELECTRICAL ENGINEERING AND COMPUTER SCIENCE
in partial fulfillment of the requirements for the degree of
DOCTOR OF PHILOSOPHY

at the

MASSACHUSETTS INSTITUTE OF TECHNOLOGY

September 2018

Signature of Author Signature redacted
Department of Electrical Engineering and Computer Science
August 31, 2018

Certified by Signature redacted
James G. Fujimoto
Elihu Thomson Professor of Electrical Engineering and Computer Science
Thesis Supervisor

Accepted by Signature redacted
Leslie A. Kolodziejski
Professor of Electrical Engineering and Computer Science
Chair, Department Committee on Graduate Students

Enabling Technologies for Functional Optical Coherence Tomography in Retinal Disease

by

ByungKun Lee

Submitted to the Department of Electrical Engineering and Computer Science on August 31, 2018 in partial fulfillment of the requirements for the degree of Doctor of Philosophy

Abstract

Optical coherence tomography (OCT) imaging of retinal function has become increasingly important because alterations in the function may reflect earlier changes in ocular diseases than the alterations in the structure. Since diagnostic markers in structural OCT using commercial instruments already underwent extensive investigations, novel markers in retinal function implying disease onset or progression are important for further development of novel markers in OCT diagnostics of ocular disease.

Retinal OCT applications such as blood flow imaging and stimulus-response imaging often requires high imaging speed since repeated scans of the same position or densely sampled scans are used. Our group developed a high-speed swept-source/Fourier-domain OCT (SS-OCT) prototype to investigate retinal hemodynamics and vascular structures in major ocular diseases such as age-related macular degeneration (AMD), glaucoma, and diabetic retinopathy with OCT angiography or Doppler OCT. Our group also used an ultrahigh-resolution (UHR) spectral/Fourier-domain OCT (SD-OCT) instrument to investigate dark adaptation of the photoreceptors after a photobleach by measuring the changes in the distances between densely packed, bright bands in the outer retina. Dark adaptation can be an indicator of photoreceptor health and it is postulated that compromised dark adaptation is a manifestation of early AMD.

The current thesis reports two technical advancements in OCT imaging of retinal function: image processing algorithm for total retinal blood flow (TRBF) calculation with en face Doppler OCT using the high-speed SS-OCT prototype and the instrumentation of the newly deployed UHR SD-OCT prototype with effective depth range extension using reference arm length modulation (ReALM). These techniques aim for operator-friendly, robust, and repeatable assessment of retinal blood flow or the photoreceptor layer to provide powerful tools for future investigations of retinal function. The contents of the current thesis includes hardware and software approaches that overcomes inherent limitations of OCT such as signal penetration and depth range as well as preliminary imaging results and pilot study findings.

Thesis Supervisor: James G. Fujimoto

Title: Elihu Thomson Processor of Electrical Engineering and Computer Science

Acknowledgements

I would like to express my sincere gratitude to Prof. James G. Fujimoto, my research supervisor, for providing an excellent research environment and encouraging me to challenge complex engineering problems. The collaborative research infrastructure he offered was truly exceptional, allowing me to experience both the most technical aspect and the most clinical aspect of biomedical optics. He often suggested some of the most creative engineering ideas I have ever heard of; my work in technical advancement was in large part based on his innovative ideas.

I would like to thank Dr. Woo Jhon Choi, who was my senior graduate student in the first three years of my program. He was a great mentor who taught me instrument building and calibration skills, which were critical for most of my projects in later years. In fact, one of the major topics of this thesis was pioneered by him before I brought it to further development. Moreover, I have learned a strong-willed, persistent research mindset from him. He has shown me that the endeavor for perfection is one of the most important factors in high-quality engineering.

I could not have come to the completion of this thesis without the academic and mental support from my colleagues, Eric M. Moult and Yasin Alibhai. They were always there not only to discuss about research projects but also to listen to my personal feelings. They motivated me in the most difficult times and celebrated with me at the brightest moments. I feel truly grateful for the friendship we have built through the years of my stay.

I would like to show my appreciation for the spiritual fellowship with one of my best friends, RaeKyu Park. Rooming with me in the final three years of my stay, he has encouraged me by sharing his experience and spiritual insights at the darkest hour of my program to lighten me up. I always felt truly at home when I came back from a tiring day at work and chatted with him about what happened in the lab. I truly thank God for sending him to my life.

Remember my affliction and my wanderings,
the wormwood and the gall!
My soul continually remembers it
and is bowed down within me.
But this I call to mind, and therefore I have hope:
The steadfast love of the Lord never ceases;
his mercies never come to an end;
they are new every morning;
great is your faithfulness.
"The Lord is my portion," says my soul,
"therefore I will hope in him."

Lamentations 3:19-24

Peace I leave with you; my peace I give to you.
Not as the world gives do I give to you
Let not your hearts be troubled, neither let them be afraid.

John 14:27

Do not be anxious about anything, but in everything by prayer
and supplication with thanksgiving let your requests be made known to God.
And the peace of God, which surpasses all understanding,
will guard your hearts and your minds in Christ Jesus.

Philippians 4:6-7

Table of Contents

Chapter 1
Introduction

1.1 Introduction to Optical Coherence Tomography

1.1.1 Overview

The first section of the current thesis is designated to a condensed review of working principles of optical coherence tomography (OCT) [1] particularly in the context of retinal imaging applications [2]. The primary purpose of this section is to set up a common mathematical framework which would remain consistent throughout the thesis for describing core principles of Doppler OCT and ultrahigh-resolution OCT. Lengthy explanation for basic concepts of OCT would not have high academic value because there are well-known sources [3-6] which describes the theoretical foundation and the early implementations of OCT in a greater detail. Therefore, the verbal description in this section is greatly simplified and the mathematical equations are emphasized; readers may look into the cited sources for a more complete introduction to OCT.

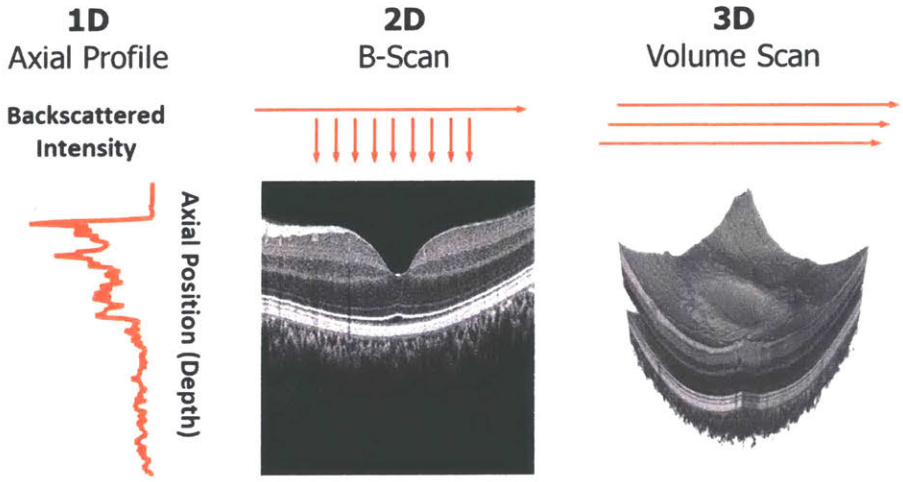

Fig 1.1. Basic drawings of of OCT A-scan, B-scan and volume scans. Information along the depth dimension is obtained by low-coherence interferometry without optical scanning.

OCT combines the technical elements of low-coherence interferometry and scanning confocal microscopy to perform non-invasive *in vivo* imaging of biological tissue at high speeds with micrometer-scale resolution. The low-coherence interferometer is used to measure the magnitude and the echo phase delay of the backscattered signal, which constructs the axial profile of the sample at a particular lateral location. The scanner moves the lateral location of the illumination beam to obtain cross-sectional or volumetric images of the biological tissue. The core theoretical concepts of OCT are explained in further detail below.

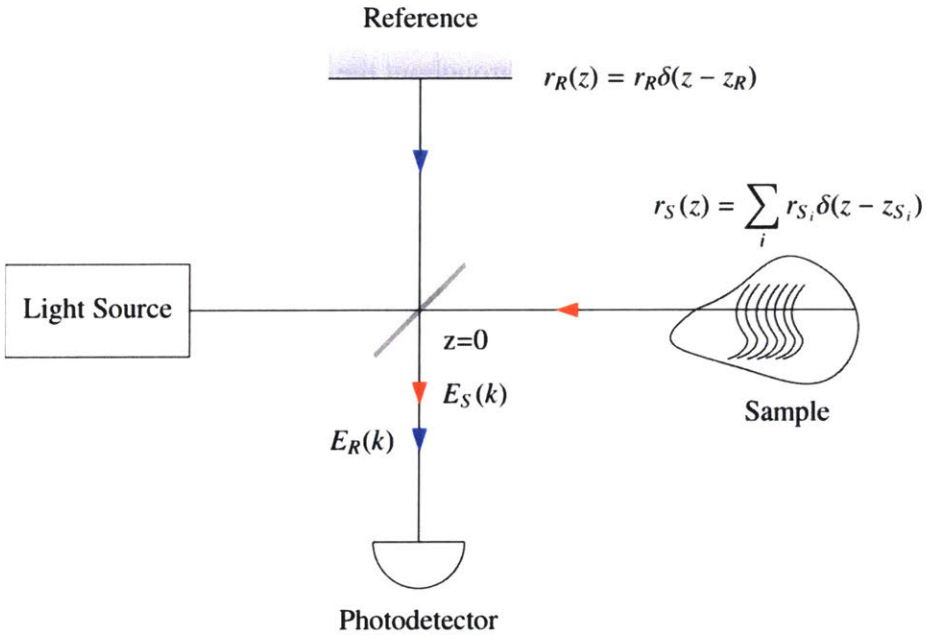

Fig 1.2 A schematic of a low-coherence interferometer using the Michelson configuration. The reflective coefficients r_R and r_{S_n} takes the beamsplitter into account.

1.1.2 Low-Coherence Interferometry

OCT uses free-space or fiber-optic implementations of modified Michelson or Mach-Zehnder interferometer powered by light sources with wide optical bandwidth. Fig. 1.2 shows a schematic of a low-coherence interferometer based on a fiber-optic Michelson interferometer. One end of the interferometer is terminated by a metallic mirror or a retro-reflector and serves as the reference optical path, simply referred as the reference arm. The other end of the interferometer

is terminated by the biological tissue, simply referred as the sample arm. One axial scan (A-scan) is completed by recording the interferogram between the back-reflected electromagnetic waves from the reference arm and the sample arm. The power spectral density at the photodetector can be written as below:

$$I(k) = \left| E_R(k) + E_S(k) \right|^2 \tag{1.1}$$

where k is the wavenumber in vacuum $E_R(k)$ and $E_S(k)$ are the Fourier-domain representations of the reference arm electromagnetic field and the sample arm electromagnetic field, respectively. For simplicity, scaling factor dependent on the unit system is neglected. The reference arm field is simply an attenuated and delayed copy of the input field and can be expressed as $E_R(k) = E(k) r_R e^{-j2kz_R}$, where z_R is the single-pass optical path length of the reference arm. The sample arm field is a superposition of the backscattered field from each reflective layers of the sample with reflectivity profile $r_S(z) = \sum_i r_{S_i} \delta(z - z_{S_i})$ and can be written as $E_S(k) = E(k) \sum_i r_{S_i} e^{-j2kz_{S_i}}$, where z_{S_i} is the single-pass optical path length to the i^{th} reflective layer in the sample.

Therefore, (1.1) may be rewritten as

$$I(k) = \left| E(k) \right|^2 \left| r_R e^{-j2kz_R} + \sum_i r_{S_i} e^{-j2kz_{S_i}} \right|^2 \tag{1.2}$$

For simplicity, the splitting ratio of the beamsplitter was included in the reflection coefficients. In typical OCT imaging applications, the backscattered power from the sample arm is 30 to 40 dB lower than the backrefleceted power from the reference arm. Therefore, when expanding the expression, it is safe to ignore the autocorrelation terms in between the sample arm reflections:

$$I(k) \approx \underbrace{|E(k)|^2 r_R^2}_{\text{Background}} + \underbrace{|E(k)|^2 \cdot 2r_R \sum_i r_{S_i} \cos 2k(z_{S_i} - z_R)}_{\text{Fringes}} \tag{1.3}$$

Here, we have assumed that the reflection coefficients are real for simplicity. As shown in (1.3), interferometric mixing of the sample arm field and the reference arm field generates a cross-correlation term between the two fields which is much larger than the field autocorrelation term of the sample arm itself. This effect enables highly sensitive detection of small backscattering signals, providing a powerful tool for accurate *in vivo* assessment of biological tissues.

The spectral interferogram (1.3) can be directly acquired in the Fourier domain, using a spectrometer or a tunable light source; its space-domain dual can also be acquired by scanning the reference arm length. The following subsections explain the two acquisition schemes OCT.

1.1.3 Time-Domain OCT

In the early development phase of OCT, spectrometer and tunable light source technologies for OCT were not available. Therefore, the spectral interferogam (1.3) was recorded in the space domain by scanning the reference arm length z_R; this approach is referred as time-domain OCT (TD-OCT). For TD-OCT, the recorded signal can be calculated by integrating the spectral interferogram (1.3) across the whole bandwidth:

$$\begin{aligned} S_{TD}(z_R) &= \int_{-\infty}^{\infty} I(k)dk \\ &= \int_{-\infty}^{\infty} |E(k)|^2 \left[r_R^2 + 2r_R \sum_i r_{S_i} \cos 2k(z_{S_i} - z_R) \right] dk \\ &= r_R^2 \int_{-\infty}^{\infty} |E(k)|^2 \, dk + r_R \sum_i r_{S_i} \int |E(k)|^2 [e^{j2k(z_{S_i} - z_R)} + e^{-j2k(z_{S_i} - z_R)}] dk \\ &= r_R^2 A(0) + r_R \sum_i r_{S_i} \left\{ A[-2(z_{S_i} - z_R)] + A[2(z_{S_i} - z_R)] \right\} \end{aligned} \tag{1.4}$$

where $A(z) \equiv \int_{-\infty}^{\infty} E(z')E^*(z'-z)dz'$ is the optical field autocorrelation function of the input light source. According to the Wiener-Khinchin-Einstein theorem, the field autocorrelation is the Fourier transform dual of the power spectral density:

$$A(z) = \int_{-\infty}^{\infty} |E(k)|^2 e^{jkz} dk . \tag{1.5}$$

If the power spectral density is pre-shaped to be symmetric about its center wavenumber k_0, $A(z)$ can be decomposed into the real-valued, even function $\gamma(z)$ called the coherence function and the oscillatory term at k_0:

$$A(z) = \gamma(z)e^{jk_0 z} . \tag{1.6}$$

Using this decomposition, the expression (1.4) becomes

$$S_{TD}(z_R) = \underbrace{r_R^2 \gamma(0)}_{\text{DC Offset}} + \underbrace{2r_R \sum_i r_{S_i} \gamma[2(z_{S_i} - z_R)] \cos 2k_0 (z_{S_i} - z_R)}_{\text{Fringe Bursts}} \tag{1.7}$$

Note that TD-OCT signal carries the oscillatory term $\cos 2k_0(z_{S_i} - z_R)$. Since the reference arm is scanning at a constant rate, $z_R(t) = v_R t$, the recorded signal as a function of time,

$$S_{TD}(t) = r_R^2 \gamma(0) + 2r_R \sum_i r_{S_i} \gamma[2(z_{S_i} - v_R t)] \cos 2k_0 (z_{S_i} - v_R t), \tag{1.8}$$

oscillates at the frequency $f_R = 4\pi k_0 v_R$. This necessitates the usage of an analog demodulator placed at the output of the photodetector if the analog bandwidth of the data acquisition digitizer is not high enough to capture the oscillatory term.

1.1.4 Fourier-domain OCT

The spectral interferogram (1.3) can be directly recorded in the Fourier domain using a spectrometer or a tunable light source and then Fourier-transformed to generate the axial profile.

This approach is referred as Fourier-domain OCT (FD-OCT). Implementations of FD-OCT using spectrometers are called spectral/Fourier-domain OCT (SD-OCT) and implementations using tunable light sources are called swept-source/Fourier-domain OCT (SS-OCT).

Let us revisit the spectral interferogram (1.3). The background term is independent of the sample's reflectivity and can be measured by recording the spectral interferogram without any sample and digitally subtracted from the spectral interferogram measured with the sample. The resulting background-subtracted spectral interferogram is

$$I_{BS}(k) = |E(k)|^2 \cdot 2r_R \sum_i r_{S_i} \cos 2k(z_{S_i} - z_R) \tag{1.9}$$

The FD-OCT image obtained after the Fourier transform is written as

$$\begin{aligned} S_{FD}(z) &= \int_{-\infty}^{\infty} I_{BS}(k) e^{jkz} dk \\ &= \int_{-\infty}^{\infty} |E(k)|^2 \cdot 2r_R \sum_i r_{S_i} \cos 2k(z_{S_i} - z_R) \cdot e^{jkz} dk \\ &= r_R \int_{-\infty}^{\infty} |E(k)|^2 \sum_i r_{S_i} \{ e^{jk[z-2(z_{S_i}-z_R)]} + e^{jk[z+2(z_{S_i}-z_R)]} \} dk \\ &= r_R \sum_i r_{S_i} \left\{ A[z-2(z_{S_i}-z_R)] + A[z+2(z_{S_i}-z_R)] \right\} \end{aligned} \tag{1.10}$$

Using the decomposition (1.6), (1.10) can be rewritten as

$$S_{FD}(z) = r_R e^{jk_0 z} \sum_i r_{S_i} \underbrace{\left\{ \gamma[z-2(z_{S_i}-z_R)] e^{-j2k_0(z_{S_i}-z_R)} \right.}_{\text{Positive Depth Image}} + \underbrace{\left. \gamma[z+2(z_{S_i}-z_R)] e^{j2k_0(z_{S_i}-z_R)} \right\}}_{\text{Negative Depth Image}} \tag{1.11}$$

Note that there are duplicate images at the positive and negative depth regions and it is impossible to determine which copy corresponds to the actual location of the reflection. This ambiguity arises because low-coherence interferometry only measures the component of the complex sample arm field in line with the reference arm field. Therefore, for typical practice of FD-OCT, the sample is assumed to be kept within the positive depth range, $z_{S_i} > z_R$, and the negative depth region $z < 0$ is excluded from the processed OCT image:

$$S_{FD}(z) = r_R e^{jk_0 z} \sum_i r_{S_i} \gamma[z - 2(z_{S_i} - z_R)] e^{-j2k_0(z_{S_i} - z_R)}. \quad (1.12)$$

There are two key advantages of FD-OCT over TD-OCT. First, FD-OCT achieves higher signal-to-noise ratio than that of TD OCT [4-6]. FD-OCT collects all of the backscattered light for each wavenumber, while TD-OCT only collects backscattered light from one specific depth at a time and loses the signal coming from all the other depths. Therefore, for similar axial scan rates, the signal to noise ratio of FD-OCT is higher than that of TD-OCT by roughly the number of samples per A-scan; this corresponds to a 25-35 dB advantage.

Another advantage of FD-OCT over TD-OCT is the removal of the scanning reference arm. Mechanical scanning methods such as piezoelectric stages or galvanometric scanners have maximum bandwidth of 1-2 kHz or less and can be a bottleneck for imaging speed. FD-OCT greatly simplifies the scan procedure by reducing the number of scanning dimensions, enabling rapid cross-sectional and volumetric scanning of the biological tissue at speeds unprecedented by conventional confocal scanning microscopy.

Advantages in imaging sensitivity and scanning simplicity enables FD-OCT to image the biological tissue at orders of magnitude higher speeds compared to traditional imaging techniques. High imaging speed of FD-OCT allows volumetric data acquisition with densely oversampled B-scans or rapidly repeated B-scans of the same anatomical location and thereby has opened up novel functional imaging techniques such as Doppler OCT and OCT angiography.

1.2 History and Principles of Doppler OCT

1.2.1 Overview

Doppler OCT is an imaging technique which measures the change in the echo phase delay in the OCT signal in order to measure axial velocity of moving particles. Since optical phase shift

directly translates to the sub-wavelength-scale changes in the optical path length, Doppler OCT is an effective tool for directly measuring the axial velocity of the scattering particles with high velocity resolution. In retinal imaging applications, Doppler OCT has been used for quantitative measurement of retinal blood flow.

Measurement of retinal blood flow *in vivo* is an important research area in ophthalmic imaging since alterations in retinal perfusion are suggested to play a role in pathogenesis of ocular diseases such as glaucoma [7-10] and diabetic retinopathy [11-14]. Quantitative assessment of total retinal blood flow (TRBF) enables objective comparison of retinal circulation among different subjects and simplifies longitudinal tracking of changes associated with disease progression. TRBF measurement can provide useful information for investigating ocular pathophysiology as well as for identifying potential early diagnostic markers.

Multiple imaging modalities such as video fluorescein angiography, laser speckle flowgraphy, laser Doppler velocimetry, scanning laser Doppler flowmetry, and ultrasound color Doppler imaging can be used to investigate quantitative retinal blood flow [15-22]. However, objective measurement of TRBF remains challenging. Video fluorescein angiography and laser speckle flowgraphy cannot directly measure blood flow velocity but yield indirect metrics such as arteriovenous passage time and mean blur rate. Scanning laser Doppler flowmetry (e.g. Heidelberg Retina Flowmeter, Heidelberg Engineering, Heidelberg, Germany) can map the flow velocity component along the probe beam direction over a two-dimensional scan area; however, the absolute flow velocity is required for quantitative flow rate measurement. Ultrasound color Doppler imaging can perform cross-sectional imaging and volumetric imaging of blood flow velocity but has ~200 μm spatial resolution which is insufficient to visualize detailed structure of the central retinal vasculature, complicating accurate blood flow calculation.

Among these techniques, bidirectional laser Doppler velocimetry (BLDV) combined with fundus photography is one of the best suited methods for quantitative TRBF measurement. This technique measures the maximum absolute flow velocity in a vessel by detecting the Doppler frequency shifts of the light backscattered in two different directions. The blood flow in the vessel is calculated as the product of the maximum absolute flow velocity and the effective vessel cross-sectional area, estimated from the vessel diameter measured in a fundus photograph. TRBF is then calculated as the sum of the blood flow in major retinal vessels near the optic disc. BLDV measurement of TRBF was validated in healthy subjects [23-26] and used for investigating TRBF in diabetic patients [27-30]. However, the calculation of effective vessel cross-section area relies on the assumption that the vessel shapes are circular and the blood flow velocity follows a parabolic profile. This assumption can be inaccurate in some subjects and may result in flow measurement errors. Moreover, measurement times can be preclusive because individual major retinal vessels must be measured separately, requiring 20 to 55 minutes per eye [31]. Due to this limitation, the number of patients in most TRBF studies using BLDV has been relatively small.

Limited capability and poor usability of traditional methods of TRBF measurement, motivates the development of TRBF measurement techniques powered by Doppler OCT. Doppler OCT promises simpler and more robust measurements of TRBF using depth-resolved information on vascular structure and axial flow velocity. In order to develop hardware and image processing methods for accurate assessment of TRBF, understanding the inherent characteristics of Doppler OCT image acquisition methods and Doppler phase signal is crucial. Therefore, this section reviews the underlying principle of Doppler OCT, and previously reported demonstrations of retinal blood flow measurements using Doppler OCT.

1.2.2 Time-Domain Doppler OCT

Early investigators of OCT have recognized that simple demodulation with an oscillator could not recover the TD-OCT signal inside the retinal blood vessels due to the axial movement of the scattering particles. Therefore, the investigators decided to perform coherent demodulation using a lock-in amplifier to detect the in-phase and out-of-phase, or quadrature, components of the oscillating TD-OCT signal [32-37]. The usage of a lock-in amplifier not only allowed the recovery of the full signal amplitude but also enabled Doppler velocimetry. Coherent demodulation reconstructs the analytical TD-OCT signal, enabling the measurement of the phase delay change during the A-scans. Let us recall the expression (1.8) for the TD-OCT signal. The analytical signal measured by the lock-in amplifier operating at $f_R = 4\pi k_0 v_R$ is

$$S_{TD}(t) = r_R \sum_i r_{S_i} \gamma[2(z_{S_i} - v_R t)] e^{j2k_0 z_{S_i}}. \tag{1.13}$$

The frequency of the post-demodulation residual oscillatory term $e^{j2k_0 z_{S_n}} = e^{j\phi}$ is equal to the Doppler frequency shift and directly translated to axial velocity of the scattering particles:

$$f_{S_i} = \frac{1}{2\pi}\frac{d\phi}{dt} = \frac{k_0}{\pi}\frac{dz_{S_i}}{dt} = \frac{2nv_{S_i}\cos\theta}{\lambda_0} = f_0 \cdot \frac{2nv_{S_i}\cos\theta}{c} \tag{1.14}$$

where v_{S_n} is the speed of the particle and θ is the Doppler angle, the angle of the velocity vector from the optical axis. n denotes the refractive index of the sample, c denotes the speed of light in vacuum. $\lambda_0 = 2\pi/k_0$ and $f_0 = k_0 c/2\pi$ are the center wavelength and the center frequency of the light source, respectively. The detection range of axial velocity was limited by the detection bandwidth of the lock-in amplifier.

This technique robustly measured axial flow velocities in the retinal blood vessels in real time, revealing the cross-sectional blood flow velocity profile inside the blood vessels [35] and

pulsatile fluctuation of blood flow velocity [38]. However, true blood flow speed could not be measured because the Doppler angle was unknown. Hence, blood flow even in a single vessel could not be measured. First reported Doppler OCT measurement of TRBF was using FD-OCT.

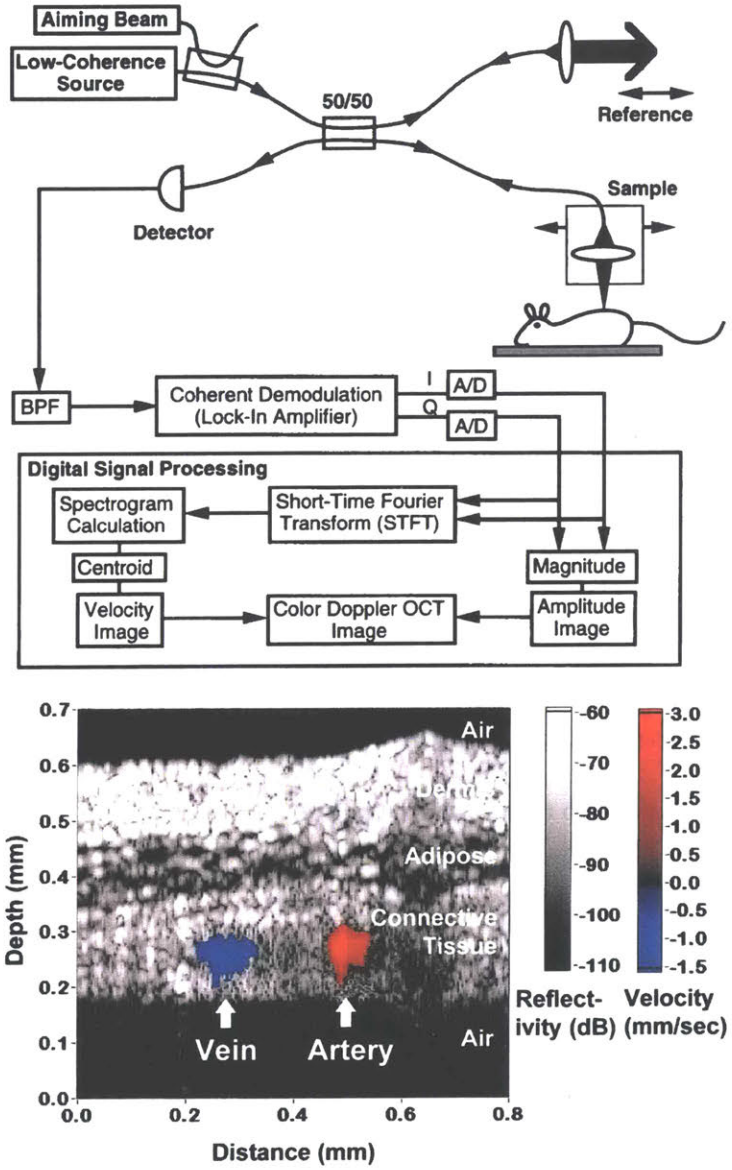

Fig 1.3. Schematic of experimental setup for time-domain Doppler OCT and blood flow detecetion in the rat retina; source: [31].

1.2.2 Fourier-Domain Doppler OCT

FD-Doppler OCT and TD-Doppler OCT are two distinct techniques with different working principles, although they both aim to measure the axial velocity of the scattering particles. TD-Doppler OCT measures the post-demodulation residual phase during the A-scans. TD-OCT requires a lock-in amplifier to output in-phase and out-of-phase components of the demodulated signal. In contrast, FD-Doppler OCT measures the phase shift in between two A-scans taken in quick succession [39, 40]. This phase shift is called Doppler phase and is proportional to the axial velocity of the scattering particles. FD-Doppler OCT does not require any extra hardware because FD-OCT inherently carries phase information, as shown in the expression (1.12) for the FD OCT signal:

$$S_{FD}(z) = r_R e^{jk_0 z} \sum_i r_{S_i} \gamma[z - 2(z_{S_i} - z_R)] e^{-j2k_0(z_{S_i} - z_R)}. \tag{1.15}$$

The phase delay term $e^{-j2k_0(z_{S_i} - z_R)}$ indicates the axial position of each scattering particles in the sample. Therefore, axial velocity of the particles can be measured by comparing two A-scans of the same sample acquired at two different time points:

$$\begin{aligned} S_{FD}(z,t) &= r_R e^{jk_0 z} \sum_i r_{S_i} \gamma[z - 2(z_{S_i} - z_R)] e^{-j2k_0(z_{S_i} - z_R)} \\ S_{FD}(z,t+\Delta t) &= r_R e^{jk_0 z} \sum_i r_{S_i} \gamma[z - 2(z_{S_i} + \Delta z_{S_i} - z_R)] e^{-j2k_0(z_{S_i} + \Delta z_{S_i} - z_R)}. \end{aligned} \tag{1.16}$$

Assuming the displacement Δz_{S_i} is much smaller than the axial resolution, the difference between $\gamma[z - 2(z_{S_i} - z_R)]$ and $\gamma[z - 2(z_{S_i} + \Delta z_{S_i} - z_R)]$ can be neglected. Then, the only remaining difference is the phase shift $\Delta\phi = 2k_0 \Delta z_{S_i}$. The axial blood flow velocity can be calculated by dividing this phase shift by the time interval:

$$v_{S_i} \cos\theta = \frac{1}{n} \frac{\Delta z_{S_i}}{\Delta t} = \frac{1}{2nk_0} \frac{\Delta\phi}{\Delta t} = \frac{\lambda_0}{4\pi n} \frac{\Delta\phi}{\Delta t}. \tag{1.17}$$

The first demonstration of TRBF measurement with FD-Doppler OCT used multiple circumpapillary scans intercepting all of the retinal vessels around the optic disc in order to measure the flow velocity component along the OCT probe beam direction and the Doppler angle between the velocity vector and the OCT beam [41-44]. However, the flow measurement was highly sensitive to errors in the Doppler angle, especially when the vessel is oriented near 90° to the OCT beam as in the optic disc margin. Eye motion artifacts as well as varying vessel geometries in different subjects can make angle measurements challenging and require reader assistance to analyze data. Another method, bidirectional Doppler OCT, is analogous to BLDV. This approach measures Doppler velocity in two probe beam directions and uses trigonometric relations to calculate the absolute flow velocity [45] and blood flow [46]. This method addresses some of the limitations in the circumpapillary method, but cannot be performed with commercial OCT instruments because a major hardware modification is required for dual-beam scanning.

1.2.3 En Face Doppler OCT

Recent improvements in FD-OCT imaging speed enabled a new Doppler OCT approach, which avoids the need to measure the Doppler angle by analyzing blood flow in the en face plane. This method, en face Doppler OCT, was first demonstrated in brain sciences for cerebral blood flow measurement in small animals [47]. In ophthalmology, TRBF can be measured by integrating the Doppler velocity over an en face plane in volumetric data of the optic disc.

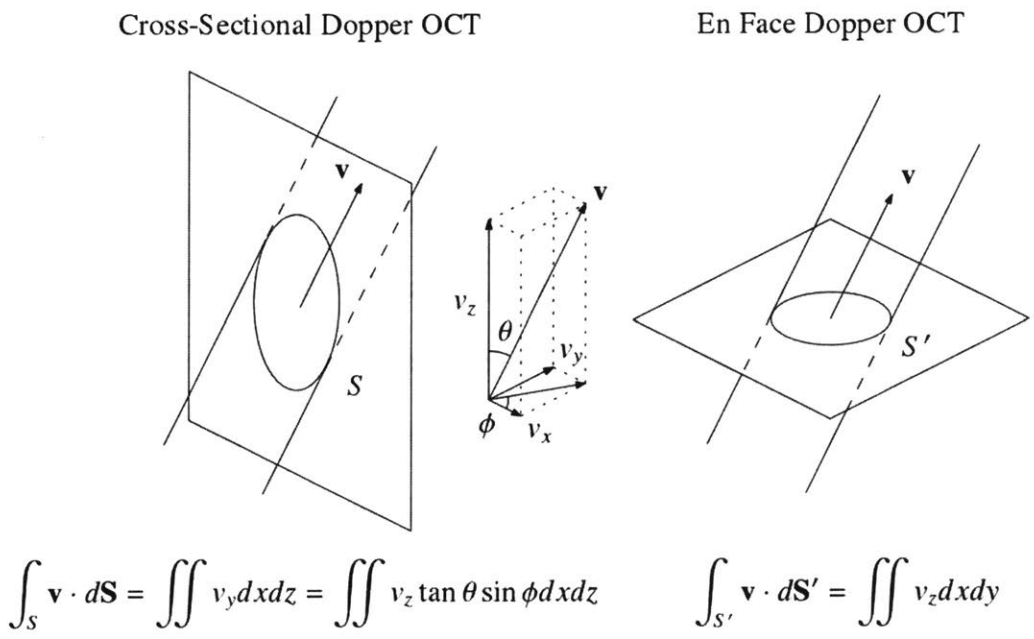

Fig 1.4 Comparison of the blood flow calculation geometries for cross-sectional Doppler OCT and en face Doppler OCT.

Fig 1.4 illustrates the geometrical properties of blood flow measurement in a single vessel using cross-sectional Doppler OCT and en face Doppler OCT, respectively. In cross-sectional Doppler OCT, the detected axial velocity component v_z lies within the image. However, the velocity component v_y perpendicular to the cross-section must be known in order to perform the blood flow surface integral,

$$F = \int_S \mathbf{v} \cdot d\mathbf{S} = \iint v_y dxdz . \tag{1.18}$$

Therefore, the angles θ and ϕ representing the orientation of the blood vessel relative to the cross-section is measured to back-calculate $v_y = v_z \tan\theta \sin\phi$, the velocity component perpendicular to the cross-sectional plane. Then, the blood flow can be calculated as

$$F = \int_S \mathbf{v} \cdot d\mathbf{S} = \iint v_y dxdz = \iint v_z \tan\theta \sin\phi dxdz . \tag{1.19}$$

The angles θ and ϕ can be measured by detecting the blood vessels in two nearby cross-sections or using multi-beam illumination.

In contrast, en face Doppler OCT does not require Doppler angle measurement because the detected axial flow velocity component is always perpendicular to the en face plane. The blood flow can be calculated by the following surface integral without angle dependence:

$$F = \int_{S'} \mathbf{v} \cdot d\mathbf{S}' = \iint v_z dx dy . \tag{1.20}$$

This geometrical simplicity enables fully automatic analysis of TRBF. High imaging speed is crucial for en face Doppler OCT because a densely sampled volumetric image is required to measure TRBF and multiple volumetric images per cardiac cycle are necessary to accurately assess pulsatile blood flow. Utilizing high-speed imaging capabilities, our group has demonstrated en face Doppler measurements of human TRBF using swept source / Fourier domain OCT (SS-OCT) at 200 kHz axial scan (A-scan) rate [48], spectral / Fourier domain OCT (SD-OCT) at 244 kHz A-scan rate [49], and SS-OCT at 400 kHz A-scan rate [50]. In order to develop software for automatic calculation TRBF without reader input, considerable amount of time and effort was invested in developing image processing algorithm for en face Doppler OCT. Chapter 2 will describe the current implementation of image processing software for en face TRBF calculation in detail.

1.3 History and Principles of Ultrahigh-Resolution OCT

1.3.1 Overview

The term ultrahigh-resolution OCT (UHR OCT) was originally used when the TD-OCT instrument which achieved 1.5 μm axial resolution using Ti:Al_2O_3 laser with 260nm bandwidth was reported [51, 52]. Since the axial resolution of the commercial instruments at the time was

10-15 μm, this instrument was thought to have ultrahigh resolution. Since then, the term UHR OCT was widely used to describe the OCT instruments with 1-3 μm axial resolution, even though the axial resolution was no longer truly "ultrahigh," as commercial FD-OCT instruments for retinal imaging were designed for 5-7 μm axial resolution.

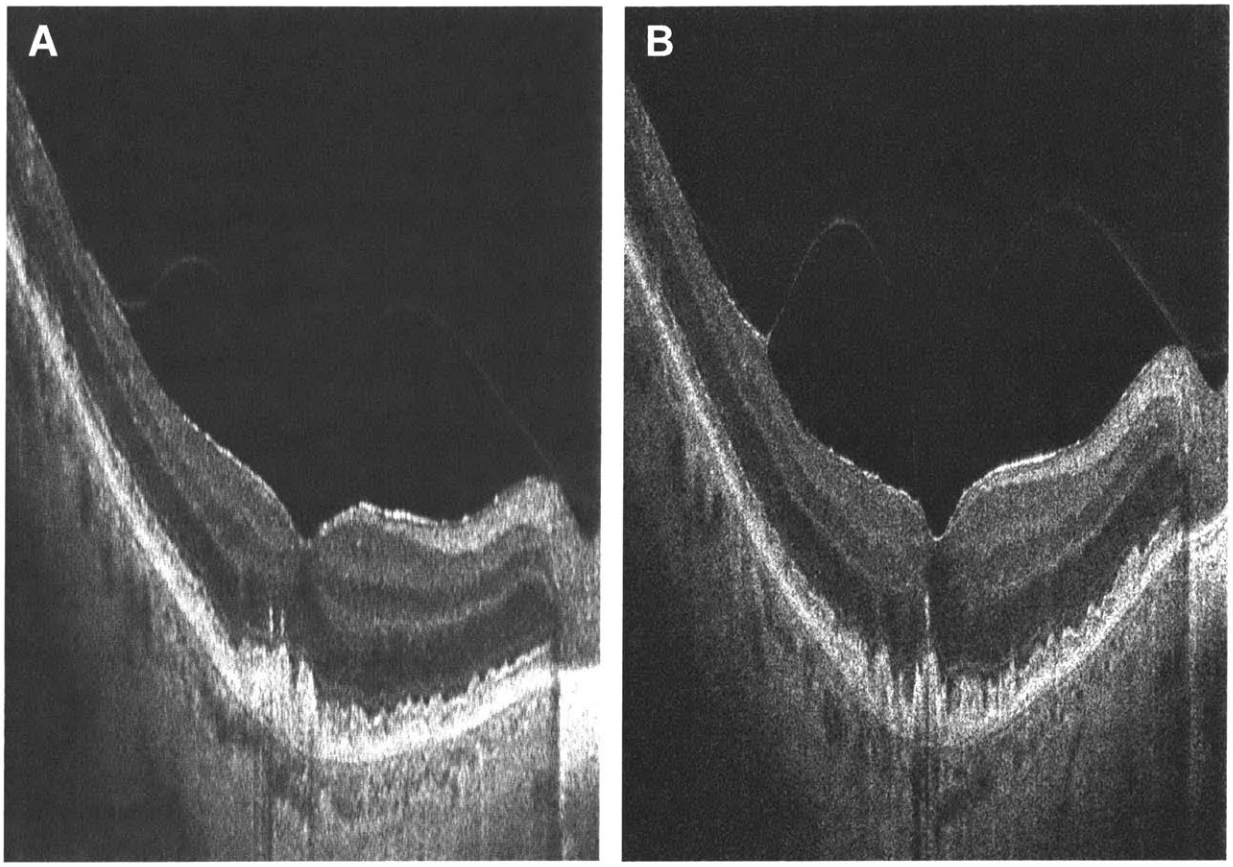

Fig 1.5. Comparison of two SD-OCT images of an eye with non-exudative age-related macular degeneration; (A) 5-μm-resolution commercial instrument and (B) 3-μm-resolution prototype instrument.

UHR OCT can visualize fine axial structures which cannot be resolved with standard resolution OCT. Fig. 1.5 shows a comparison between retinal OCT images of the same eye acquired with a standard-resolution commercial instrument and a UHR OCT prototype. Since UHR OCT reveals some of the details of the biological tissue at cellular level, it can be beneficial for advancing pathophysiological knowledge or finding novel early diagnostic markers. Clinical testing of UHR OCT was most active in retinal imaging: over 1,000 eyes with

retinal pathology was imaged with UHR OCT prototype instruments and showed unprecedented visualization of the bright, tightly packed bands in the photoreceptor layer [53-63]. These investigations have observed photoreceptor layer impairments in macular pathologies such as macular holes, central serous chorioretinopathy, age-related macular degeneration (AMD), foveomacular dystrophies, Stargardt's dystrophy, and retinitis pigmentosa.

More recently, research interest in photoreceptor changes during dark adaptation has motivated further investigations with UHR OCT. After entering darkness, the cone and rod photoreceptors in the retina have a delayed light sensitivity recovery known as dark adaptation that depends on the previous light exposure [64]. The cone photoreceptors sensitivity recovers quickly in a matter of minutes but full sensitivity recovery only occurs when the rod photoreceptors recover in 10 to 40 minutes depending on the original level of photobeaching of rhodopsin. This slow recovery rate has been attributed to the rate-limited regeneration of rhodopsin from the opsin formed by photoisomerization [65].

Patients with AMD suffer from an impairment of dark adaptation that correlates with disease severity attributed to disease impaired transportation between the retinal pigment epithelium (RPE) and photoreceptors [65-68]. This dark adaptation impairment occurs prior to significant visual acuity loss [68, 69]. There currently exists a commercial dark adaptometer that requires patient input to measure light sensitivity over time [70]. Our group has investigated UHR OCT to measure the changes in the photoreceptors during dark adaptation [71]. If these changes are observable, UHR OCT would simplify the dark adaption measurement without the need for patient input. The detection of dark adaptation can be used as a possible endpoint for clinical trials of AMD pharmaceutical treatments as well as treatments for other retinal disorders that impair dark adaptation.

There are technical challenges exclusive to UHR OCT. As UHR OCT requires usage of broadband light sources, factors such as group delay dispersion, chromatic aberration, polarization mismatch can disturb the image. In particular, UHR SD-OCT requires advanced spectrometer design to maintain diffraction-limited performance over a broad optical bandwidth. Moreover, UHR SD-OCT trades off the spectral resolution to increase the optical bandwidth, which means the depth range is traded off for achieving high axial resolution. This section discusses theoretical foundations of axial and lateral resolution in OCT, technical challenges of UHR OCT, and previous demonstrations of photoreceptor layer imaging.

1.3.2 Axial Resolution in OCT

Axial resolution in OCT is determined by the optical bandwidth of the low-coherence interferometer. This axial resolution is often referred as coherence-gated resolution; coherence gating allows OCT to achieve axial resolution much higher than the confocal-gated axial resolution limited by the numerical aperture of the illumination beam. Therefore, optical designs for sample illumination in OCT often choose to have lower numerical aperture to attain longer depth of focus. Meanwhile, lateral resolution of OCT is determined by the illumination optics and often much lower than the axial resolution. As a result, OCT instruments typically have a considerable amount of asymmetry between their axial and lateral resolutions.

This subsection will present a brief derivation of the analytical expression for the coherence-gated axial resolution of OCT. In section 1.1, we have discussed about the optical field autocorrelation function,

$$A(z) \equiv \int_{-\infty}^{\infty} E(z')E^*(z'-z)dz' = \int_{-\infty}^{\infty} \left|E(k)\right|^2 e^{jkz} dk \tag{1.21}$$

and its magnitude-phase decomposition,

$$A(z) = \gamma(z)e^{jk_0 z}, \tag{1.22}$$

where E denotes the electromagnetic field of the light source and k_0 denotes the center wavenumber. The magnitude $\gamma(z)$, often called coherence function, represents the axial profile of an isolated reflective surface or scattering particle in the OCT image. $\gamma(z)$ can be analytically or computationally calculated by the following intergral:

$$\gamma(z) = \int_{-\infty}^{\infty} |E(k)|^2 e^{j(k-k_0)z} dk \tag{1.23}$$

For rough calculation of the width of the coherence function, let us assume Gaussian-shaped spectrum for simplicity:

$$|E(k)|^2 = \frac{I_0}{\Delta k\sqrt{\pi}} e^{\frac{(k-k_0)^2}{\Delta k^2}} \tag{1.24}$$

Then, the coherence function is

$$\gamma(z) = I_0 e^{-\frac{\Delta k^2 z^2}{4}} \tag{1.25}$$

In the OCT community, axial resolution is usually represented by the full-width at half-maximum (FWHM) of the axial point-spread function. Looking at (1.7) and (1.12), the axial point-spread function is a spatially compressed version of the coherence function by a factor of two, since the optical path of the sample and reference arm is passed twice. Therefore,

$$\Delta z_{FWHM} = \frac{2\sqrt{\ln 2}}{\Delta k} \approx \frac{2\ln 2}{\pi} \frac{\lambda_0^2}{\Delta\lambda_{FWHM}} \tag{1.26}$$

where λ_0 is the center wavelength and $\Delta\lambda_{FWHM}$ is the wavelength bandwidth in terms of the full width at half-maximum power spectral density.

1.3.3 Group Delay Dispersion Mismatch

Mismatch of group delay dispersion, or simply dispersion, between the reference arm and sample arm optical paths result in axial blurring and broadening of the image. This subsection explains how an error in group delay dispersion matching can limit the axial resolution of OCT.

In the previous analysis, we have assumed that the optical path lengths of the sample arm and reference arm are constant for different wavenumber in vacuum. However, typical optical media has wavenumber-dependent refractive index and this results in wavenumber-dependent sample and reference arm optical path lengths $z_R(k)$ and $z_S(k)$, where k is the wavenumber in vacuum. This means the equations (1.4) and (1.10) does not hold anymore; the axial profile of the scattering particles in the image will not be equal to the coherence function because of the second or higher order components in the phase delay $\phi(k) = -2k[z_S(k) - z_R(k)]$.

For simple demonstration, we will only consider up to the second order term of $\phi(k)$:

$$\begin{aligned}\phi(k) &= 2k[z_S(k) - z_R(k)] \\ &\approx \phi(k_0) + \left.\frac{\partial\phi}{\partial k}\right|_{k_0}(k-k_0) + \frac{1}{2}\left.\frac{\partial^2\phi}{\partial k^2}\right|_{k_0}(k-k_0)^2 \\ &= 2k[z_S(k_0) - z_R(k_0)] + \frac{\phi''}{2}(k-k_0)^2\end{aligned} \tag{1.27}$$

where ϕ'' is the dispersion mismatch. In order to see the effect of the wavenumber dependence of optical path lengths, let us recalculate the expression (1.10) for a single particle with the dispersion mismatch in consideration:

$$\begin{aligned}S_{FD}(z) &= \int_{-\infty}^{\infty} I_{BS}(k)e^{jkz}dk \\ &= \int_{-\infty}^{\infty} |E(k)|^2 \cdot 2r_R r_S \cos 2k[z_S(k) - z_R(k)] \cdot e^{jkz}dk \\ &= r_R r_S \int_{-\infty}^{\infty} |E(k)|^2 \{e^{jk[z-2(z_S-z_R)]}e^{-j\frac{\phi''}{2}(k-k_0)^2} + e^{jk[z+2(z_S-z_R)]}e^{j\frac{\phi''}{2}(k-k_0)^2}\}dk\end{aligned} \tag{1.28}$$

where z_S and z_R are simplified notations for $z_S(k_0)$ and $z_R(k_0)$, respectively. Neglecting the negative depth terms,

$$S_{FD}(z) = r_R r_S \int_{-\infty}^{\infty} |E(k)|^2 e^{jk[z-2(z_S-z_R)]} e^{-j\frac{\phi''}{2}(k-k_0)^2} dk \tag{1.29}$$

Let us assume the same Gaussian spectrum (1.24). Then, this becomes

$$S_{FD}(z) = r_R r_S \frac{I_0}{\Delta k\sqrt{\pi}} \int_{-\infty}^{\infty} e^{\left(\frac{1}{\Delta k^2}-j\frac{\phi''}{2}\right)(k-k_0)^2} e^{jk[z-2(z_S-z_R)]} dk \tag{1.30}$$

Therefore, the axial resolution affected by the dispersion is

$$\Delta z_{D,FWHM} = \frac{2\sqrt{\ln 2}}{\Delta k}\sqrt{1+\phi''^2\Delta k^4} = \Delta z_{FWHM}\sqrt{1+\phi''^2\Delta k^4}\,. \tag{1.31}$$

Dispersion can be mismatched by a number of different causes. Most commonly, any significant amount of glass layers in the sample arm scanning optics will introduce GDD mismatch. Dichroic mirrors used for overlaying OCT illumination bean on the fixation target may have highly nonlinear phase response. Eyes with different axial length from the cornea to the retina will result in changes in the dispersion mismatch. Therefore, it is recommended to computationally compensate the dispersion mismatch using optimization methods or extraction methods. This will be discussed briefly in Chapter 4.

1.4 Scope of Thesis

In this thesis, advancement of FD-OCT hardware and software technologies for functional imaging techniques will be reported. The thesis is largely divided into two functional imaging techniques: retinal blood flow imaging and photoreceptor imaging. The aims of this thesis are: 1) to develop next-generation imaging instruments or novel scan protocols for functional measurements; 2) to refine imaging processing algorithms for repeatable, automatic assessment

of quantitative metrics of retinal function; 3) test the new instruments and image processing algorithms in eyes with retinal disease and perform pilot studies.

Chapter 1 presented a general theoretical review of OCT and also introduced the history and principles of Doppler OCT and UHR OCT. It referred to a number of previous technical demonstrations and clinical studies of the two imaging modalities. Recent advances such as en face Doppler OCT and photoreceptor layer thickness response in dark adaptation were important to mention since they are directly connected with the contents of the rest of the thesis.

Chapter 2 is a detailed description of the scan pattern and the image processing algorithm for en face Doppler OCT measurement of TRBF. This chapter primarily serves as a documentation for the complex software which involves special filtering, segmentation, and artifact removal steps. In the latter parts of the chapter, a novel acquisition strategy involving pulse oximetry cardiac gating is introduced. This approach is particularly useful for instruments which operate at 200 kHz A-scan rate or lower.

Chapter 3 shows two example clinical studies of TRBF in ocular disease. The glaucoma study found a strong correlation between TRBF and visual fields (VF) loss and a possible broken-stick like relation between retinal nerve fiber layer (RNFL) thickness and TRBF similar to the previously found relation between RNFL thickness and VF loss [72]. The diabetic retinopathy (DR) study found a significant reduction of TRBF in the eyes with diabetic macular edema. The eyes with moderate non-proliferative DR (NPDR) and without DME showed bimodal distribution, motivating follow-up studies of moderate NPDR patients with reduced TRBF.

Chapter 4 is a technical report on a newly deployed UHR SD-OCT instrument. The instrument attempts to overcome the inherent depth range limitation of UHR SD-OCT by

moving the reference arm length during image acquisition to compensate for the axial displacement of the retinal image due to retinal curvature. Preliminary imaging results show interesting photoreceptor changes in AMD eyes compared to age-matched healthy eyes and also capabilities of outer retinal layer segmentation for en face image analysis. These results support that investigations of photoreceptor layer response in dark adaptation are possible with this instrument.

Chapter 5 makes suggestions on potential future research topics related to the current thesis and wraps up the thesis. It ends with the author's publication list during the research period of this thesis.

References

[1] D. Huang, E. A. Swanson, C. P. Lin, J. S. Schuman, W. G. Stinson, W. Chang, M. R. Hee, T. Flotte, K. Gregory, C. A. Puliafito, and et al., "Optical coherence tomography," *Science,* vol. 254, pp. 1178-81, Nov 22 1991.

[2] M. R. Hee, J. A. Izatt, E. A. Swanson, D. Huang, J. S. Schuman, C. P. Lin, C. A. Puliafito, and J. G. Fujimoto, "Optical coherence tomography of the human retina," *Arch Ophthalmol,* vol. 113, pp. 325-32, Mar 1995.

[3] J. A. Izatt and M. A. Choma, "Theory of Optical Coherence Tomography," *Optical Coherence Tomography: Technology and Applications,* pp. 47-72, 2008.

[4] R. Leitgeb, C. Hitzenberger, and A. Fercher, "Performance of fourier domain vs. time domain optical coherence tomography," *Opt Express,* vol. 11, pp. 889-94, Apr 21 2003.

[5] M. A. Choma, M. V. Sarunic, C. H. Yang, and J. A. Izatt, "Sensitivity advantage of swept source and Fourier domain optical coherence tomography," *Opt Express,* vol. 11, pp. 2183-2189, Sep 8 2003.

[6] J. F. de Boer, B. Cense, B. H. Park, M. C. Pierce, G. J. Tearney, and B. E. Bouma, "Improved signal-to-noise ratio in spectral-domain compared with time-domain optical coherence tomography," *Opt Lett,* vol. 28, pp. 2067-9, Nov 1 2003.

[7] S. S. Hayreh, "Blood supply of the optic nerve head and its role in optic atrophy, glaucoma, and oedema of the optic disc," *Br J Ophthalmol,* vol. 53, pp. 721-48, Nov 1969.

[8] J. Flammer, "The vascular concept of glaucoma," *Surv Ophthalmol,* vol. 38 Suppl, pp. S3-6, May 1994.

[9] J. Flammer, S. Orgul, V. P. Costa, N. Orzalesi, G. K. Krieglstein, L. M. Serra, J. P. Renard, and E. Stefansson, "The impact of ocular blood flow in glaucoma," *Prog Retin Eye Res,* vol. 21, pp. 359-93, Jul 2002.

[10] M. C. Grieshaber and J. Flammer, "Blood flow in glaucoma," *Curr Opin Ophthalmol,* vol. 16, pp. 79-83, Apr 2005.

[11] L. Schmetterer and M. Wolzt, "Ocular blood flow and associated functional deviations in diabetic retinopathy," *Diabetologia,* vol. 42, pp. 387-405, Apr 1999.

[12] R. Klein, B. E. Klein, S. E. Moss, T. Y. Wong, L. Hubbard, K. J. Cruickshanks, and M. Palta, "Retinal vascular abnormalities in persons with type 1 diabetes: the Wisconsin Epidemiologic Study of Diabetic Retinopathy: XVIII," *Ophthalmology,* vol. 110, pp. 2118-25, Nov 2003.

[13] A. Yoshida, G. T. Feke, J. Morales-Stoppello, G. D. Collas, D. G. Goger, and J. W. McMeel, "Retinal blood flow alterations during progression of diabetic retinopathy," *Arch Ophthalmol,* vol. 101, pp. 225-7, Feb 1983.

[14] V. Patel, S. Rassam, R. Newsom, J. Wiek, and E. Kohner, "Retinal blood flow in diabetic retinopathy," *BMJ,* vol. 305, pp. 678-83, Sep 19 1992.

[15] A. S. Hafez, R. L. Bizzarro, and M. R. Lesk, "Evaluation of optic nerve head and peripapillary retinal blood flow in glaucoma patients, ocular hypertensives, and normal subjects," *Am J Ophthalmol,* vol. 136, pp. 1022-31, Dec 2003.

[16] G. Fuchsjager-Mayrl, B. Wally, M. Georgopoulos, G. Rainer, K. Kircher, W. Buehl, T. Amoako-Mensah, H. G. Eichler, C. Vass, and L. Schmetterer, "Ocular blood flow and systemic blood pressure in patients with primary open-angle glaucoma and ocular hypertension," *Invest Ophthalmol Vis Sci,* vol. 45, pp. 834-9, Mar 2004.

[17] A. Harris, R. C. Sergott, G. L. Spaeth, J. L. Katz, J. A. Shoemaker, and B. J. Martin, "Color Doppler analysis of ocular vessel blood velocity in normal-tension glaucoma," *Am J Ophthalmol,* vol. 118, pp. 642-9, Nov 15 1994.

[18] S. J. Rankin, B. E. Walman, A. R. Buckley, and S. M. Drance, "Color Doppler imaging and spectral analysis of the optic nerve vasculature in glaucoma," *Am J Ophthalmol,* vol. 119, pp. 685-93, Jun 1995.

[19] G. T. Feke, S. M. Buzney, H. Ogasawara, N. Fujio, D. G. Goger, N. P. Spack, and K. H. Gabbay, "Retinal circulatory abnormalities in type 1 diabetes," *Invest Ophthalmol Vis Sci,* vol. 35, pp. 2968-75, Jun 1994.

[20] S. Wolf, O. Arend, H. Toonen, B. Bertram, F. Jung, and M. Reim, "Retinal capillary blood flow measurement with a scanning laser ophthalmoscope. Preliminary results," *Ophthalmology,* vol. 98, pp. 996-1000, Jun 1991.

[21] B. Bertram, S. Wolf, S. Fiehofer, K. Schulte, O. Arend, and M. Reim, "Retinal circulation times in diabetes mellitus type 1," *Br J Ophthalmol,* vol. 75, pp. 462-5, Aug 1991.

[22] S. E. Bursell, A. C. Clermont, B. T. Kinsley, D. C. Simonson, L. M. Aiello, and H. A. Wolpert, "Retinal blood flow changes in patients with insulin-dependent diabetes mellitus and no diabetic retinopathy," *Invest Ophthalmol Vis Sci,* vol. 37, pp. 886-97, Apr 1996.

[23] C. E. Riva, J. E. Grunwald, S. H. Sinclair, and B. L. Petrig, "Blood velocity and volumetric flow rate in human retinal vessels," *Invest Ophthalmol Vis Sci,* vol. 26, pp. 1124-32, Aug 1985.

[24] G. T. Feke, H. Tagawa, D. M. Deupree, D. G. Goger, J. Sebag, and J. J. Weiter, "Blood flow in the normal human retina," *Invest Ophthalmol Vis Sci,* vol. 30, pp. 58-65, Jan 1989.

[25] J. P. Garcia, Jr., P. T. Garcia, and R. B. Rosen, "Retinal blood flow in the normal human eye using the canon laser blood flowmeter," *Ophthalmic Research,* vol. 34, pp. 295-9, Sep-Oct 2002.

[26] K. Guan, C. Hudson, and J. G. Flanagan, "Variability and repeatability of retinal blood flow measurements using the Canon Laser Blood Flowmeter," *Microvasc Res,* vol. 65, pp. 145-51, May 2003.

[27] J. E. Grunwald, C. E. Riva, J. Baine, and A. J. Brucker, "Total retinal volumetric blood flow rate in diabetic patients with poor glycemic control," *Invest Ophthalmol Vis Sci,* vol. 33, pp. 356-63, Feb 1992.

[28] G. T. Feke, H. Tagawa, A. Yoshida, D. G. Goger, J. J. Weiter, S. M. Buzney, and J. W. McMeel, "Retinal circulatory changes related to retinopathy progression in insulin-dependent diabetes mellitus," *Ophthalmology,* vol. 92, pp. 1517-22, Nov 1985.

[29] J. E. Grunwald, J. DuPont, and C. E. Riva, "Retinal haemodynamics in patients with early diabetes mellitus," *Br J Ophthalmol,* vol. 80, pp. 327-31, Apr 1996.

[30] B. Pemp, E. Polska, G. Garhofer, M. Bayerle-Eder, A. Kautzky-Willer, and L. Schmetterer, "Retinal blood flow in type 1 diabetic patients with no or mild diabetic retinopathy during euglycemic clamp," *Diabetes Care,* vol. 33, pp. 2038-42, Sep 2010.

[31] G. Garhofer, R. Werkmeister, N. Dragostinoff, and L. Schmetterer, "Retinal blood flow in healthy young subjects," *Invest Ophthalmol Vis Sci,* vol. 53, pp. 698-703, Feb 2012.

[32] J. A. Izatt, M. D. Kulkami, S. Yazdanfar, J. K. Barton, and A. J. Welch, "In vivo bidirectional color Doppler flow imaging of picoliter blood volumes using optical coherence tomograghy," *Opt Lett,* vol. 22, pp. 1439-1441, Sep 15 1997.

[33] S. Yazdanfar, M. D. Kulkarni, and J. A. Izatt, "High resolution imaging of in vivo cardiac dynamics using color Doppler optical coherence tomography," *Opt Express,* vol. 1, pp. 424-431, Dec 22 1997.

[34] T. G. van Leeuwen, M. D. Kulkarni, S. Yazdanfar, A. M. Rollins, and J. A. Izatt, "High-flow-velocity and shear-rate imaging by use of color Doppler optical coherence tomography," *Opt Lett,* vol. 24, pp. 1584-1586, Nov 15 1999.

[35] S. Yazdanfar, A. M. Rollins, and J. A. Izatt, "Imaging and velocimetry of the human retinal circulation with color Doppler optical coherence tomography," *Opt Lett,* vol. 25, pp. 1448-1450, Oct 1 2000.

[36] V. Westphal, S. Yazdanfar, A. M. Rollins, and J. A. Izatt, "Real-time, high velocity-resolution color Doppler optical coherence tomography," *Opt Lett,* vol. 27, pp. 34-36, Jan 1 2002.

[37] A. M. Rollins, S. Yazdanfar, J. K. Barton, and J. A. Izatt, "Real-time in vivo color Doppler optical coherence tomography," *J Biomed Opt,* vol. 7, pp. 123-9, Jan 2002.

[38] S. Yazdanfar, A. M. Rollins, and J. A. Izatt, "In vivo imaging of human retinal flow dynamics by color Doppler optical coherence tomography," *Arch Ophthalmol,* vol. 121, pp. 235-9, Feb 2003.

[39] R. Leitgeb, L. Schmetterer, W. Drexler, A. Fercher, R. Zawadzki, and T. Bajraszewski, "Real-time assessment of retinal blood flow with ultrafast acquisition by color Doppler Fourier domain optical coherence tomography," *Opt Express,* vol. 11, pp. 3116-21, Nov 17 2003.

[40] R. A. Leitgeb, L. Schmetterer, C. K. Hitzenberger, A. F. Fercher, F. Berisha, M. Wojtkowski, and T. Bajraszewski, "Real-time measurement of in vitro flow by Fourier-domain color Doppler optical coherence tomography," *Opt Lett,* vol. 29, pp. 171-173, Jan 15 2004.

[41] Y. Wang, B. A. Bower, J. A. Izatt, O. Tan, and D. Huang, "In vivo total retinal blood flow measurement by Fourier domain Doppler optical coherence tomography," *J Biomed Opt,* vol. 12, p. 041215, Jul-Aug 2007.

[42] Y. Wang, B. A. Bower, J. A. Izatt, O. Tan, and D. Huang, "Retinal blood flow measurement by circumpapillary Fourier domain Doppler optical coherence tomography," *J Biomed Opt,* vol. 13, p. 064003, Nov-Dec 2008.

[43] Y. Wang, A. Lu, J. Gil-Flamer, O. Tan, J. A. Izatt, and D. Huang, "Measurement of total blood flow in the normal human retina using Doppler Fourier-domain optical coherence tomography," *Br J Ophthalmol,* vol. 93, pp. 634-7, May 2009.

[44] Y. Wang, A. A. Fawzi, R. Varma, A. A. Sadun, X. Zhang, O. Tan, J. A. Izatt, and D. Huang, "Pilot study of optical coherence tomography measurement of retinal blood flow in retinal and optic nerve diseases," *Invest Ophthalmol Vis Sci,* vol. 52, pp. 840-5, Feb 2011.

[45] R. M. Werkmeister, N. Dragostinoff, M. Pircher, E. Gotzinger, C. K. Hitzenberger, R. A. Leitgeb, and L. Schmetterer, "Bidirectional Doppler Fourier-domain optical coherence tomography for measurement of absolute flow velocities in human retinal vessels," *Opt Lett,* vol. 33, pp. 2967-9, Dec 15 2008.

[46] C. Blatter, B. Grajciar, L. Schmetterer, and R. A. Leitgeb, "Angle independent flow assessment with bidirectional Doppler optical coherence tomography," *Opt Lett,* vol. 38, pp. 4433-6, Nov 1 2013.

[47] V. J. Srinivasan, S. Sakadzic, I. Gorczynska, S. Ruvinskaya, W. Wu, J. G. Fujimoto, and D. A. Boas, "Quantitative cerebral blood flow with optical coherence tomography," *Opt Express,* vol. 18, pp. 2477-94, Feb 1 2010.

[48] B. Baumann, B. Potsaid, M. F. Kraus, J. J. Liu, D. Huang, J. Hornegger, A. E. Cable, J. S. Duker, and J. G. Fujimoto, "Total retinal blood flow measurement with ultrahigh speed swept source/Fourier domain OCT," *Biomed Opt Express,* vol. 2, pp. 1539-52, Jun 1 2011.

[49] W. Choi, B. Baumann, J. J. Liu, A. C. Clermont, E. P. Feener, J. S. Duker, and J. G. Fujimoto, "Measurement of pulsatile total blood flow in the human and rat retina with ultrahigh speed spectral/Fourier domain OCT," *Biomed Opt Express,* vol. 3, pp. 1047-61, May 1 2012.

[50] W. Choi, B. Potsaid, V. Jayaraman, B. Baumann, I. Grulkowski, J. J. Liu, C. D. Lu, A. E. Cable, D. Huang, J. S. Duker, and J. G. Fujimoto, "Phase-sensitive swept-source optical coherence tomography imaging of the human retina with a vertical cavity surface-emitting laser light source," *Opt Lett,* vol. 38, pp. 338-40, Feb 1 2013.

[51] W. Drexler, U. Morgner, F. X. Kartner, C. Pitris, S. A. Boppart, X. D. Li, E. P. Ippen, and J. G. Fujimoto, "In vivo ultrahigh-resolution optical coherence tomography," *Opt Lett,* vol. 24, pp. 1221-3, Sep 1 1999.

[52] W. Drexler, U. Morgner, R. K. Ghanta, F. X. Kartner, J. S. Schuman, and J. G. Fujimoto, "Ultrahigh-resolution ophthalmic optical coherence tomography," *Nat Med,* vol. 7, pp. 502-7, Apr 2001.

[53] W. Drexler, H. Sattmann, B. Hermann, T. H. Ko, M. Stur, A. Unterhuber, C. Scholda, O. Findl, M. Wirtitsch, J. G. Fujimoto, and A. F. Fercher, "Enhanced visualization of macular pathology with the use of ultrahigh-resolution optical coherence tomography," *Arch Ophthalmol,* vol. 121, pp. 695-706, May 2003.

[54] T. H. Ko, J. G. Fujimoto, J. S. Schuman, L. A. Paunescu, A. M. Kowalevicz, I. Hartl, W. Drexler, G. Wollstein, H. Ishikawa, and J. S. Duker, "Comparison of ultrahigh- and standard-resolution optical coherence tomography for imaging macular pathology," *Ophthalmology,* vol. 112, pp. 1922 e1-15, Nov 2005.

[55] E. Ergun, B. Hermann, M. Wirtitsch, A. Unterhuber, T. H. Ko, H. Sattmann, C. Scholda, J. G. Fujimoto, M. Stur, and W. Drexler, "Assessment of central visual function in Stargardt's disease/fundus flavimaculatus with ultrahigh-resolution optical coherence tomography," *Invest Ophthalmol Vis Sci,* vol. 46, pp. 310-6, Jan 2005.

[56] G. Wollstein, L. A. Paunescu, T. H. Ko, J. G. Fujimoto, A. Kowalevicz, I. Hartl, S. Beaton, H. Ishikawa, C. Mattox, O. Singh, J. Duker, W. Drexler, and J. S. Schuman, "Ultrahigh-resolution optical coherence tomography in glaucoma," *Ophthalmology,* vol. 112, pp. 229-37, Feb 2005.

[57] T. H. Ko, J. G. Fujimoto, J. S. Duker, L. A. Paunescu, W. Drexler, C. R. Baumal, C. A. Puliafito, E. Reichel, A. H. Rogers, and J. S. Schuman, "Comparison of ultrahigh- and standard-resolution optical coherence tomography for imaging macular hole pathology and repair," *Ophthalmology,* vol. 111, pp. 2033-43, Nov 2004.

[58] M. G. Wirtitsch, E. Ergun, B. Hermann, A. Unterhuber, M. Stur, C. Scholda, H. Sattmann, T. H. Ko, J. G. Fujimoto, and W. Drexler, "Ultrahigh resolution optical coherence tomography in macular dystrophy," *Am J Ophthalmol,* vol. 140, pp. 976-983, Dec 2005.

[59] L. A. Paunescu, T. H. Ko, J. S. Duker, A. Chan, W. Drexler, J. S. Schuman, and J. G. Fujimoto, "Idiopathic juxtafoveal retinal telangiectasis: new findings by ultrahigh-resolution optical coherence tomography," *Ophthalmology,* vol. 113, pp. 48-57, Jan 2006.

[60] T. H. Ko, A. J. Witkin, J. G. Fujimoto, A. Chan, A. H. Rogers, C. R. Baumal, J. S. Schuman, W. Drexler, E. Reichel, and J. S. Duker, "Ultrahigh-resolution optical coherence tomography of surgically closed macular holes," *Arch Ophthalmol,* vol. 124, pp. 827-36, Jun 2006.

[61] C. Scholda, M. Wirtitsch, B. Hermann, A. Unterhuber, E. Ergun, H. Sattmann, T. H. Ko, J. G. Fujimoto, A. F. Fercher, M. Stur, U. Schmidt-Erfurth, and W. Drexler, "Ultrahigh resolution optical coherence tomography of macular holes," *Retina,* vol. 26, pp. 1034-41, Nov-Dec 2006.

[62] A. J. Witkin, J. S. Duker, T. H. Ko, J. G. Fujimoto, and J. S. Schuman, "Ultrahigh resolution optical coherence tomography of birdshot retinochoroidopathy," *Br J Ophthalmol,* vol. 89, pp. 1660-1, Dec 2005.

[63] A. J. Witkin, M. Wojtkowski, E. Reichel, V. J. Srinivasan, J. G. Fujimoto, J. S. Schuman, and J. S. Duker, "Photoreceptor disruption secondary to posterior vitreous detachment as visualized using high-speed ultrahigh-resolution optical coherence tomography," *Arch Ophthalmol,* vol. 125, pp. 1579-80, Nov 2007.

[64] S. Hecht, C. Haig, and A. M. Chase, "The Influence of Light Adaptation on Subsequent Dark Adaptation of the Eye," *J Gen Physiol,* vol. 20, pp. 831-50, Jul 20 1937.

[65] T. D. Lamb and E. N. Pugh, Jr., "Phototransduction, dark adaptation, and rhodopsin regeneration the proctor lecture," *Invest Ophthalmol Vis Sci,* vol. 47, pp. 5137-52, Dec 2006.

[66] G. R. Jackson, C. Owsley, and C. A. Curcio, "Photoreceptor degeneration and dysfunction in aging and age-related maculopathy," *Ageing Res Rev,* vol. 1, pp. 381-96, Jun 2002.

[67] C. Owsley, G. McGwin, G. R. Jackson, D. C. Heimburger, C. J. Piyathilake, R. Klein, M. F. White, and K. Kallies, "Effect of short-term, high-dose retinol on dark adaptation in aging and early age-related maculopathy," *Invest Ophthalmol Vis Sci,* vol. 47, pp. 1310-8, Apr 2006.

[68] G. R. Jackson and J. G. Edwards, "A short-duration dark adaptation protocol for assessment of age-related maculopathy," *J Ocul Biol Dis Infor,* vol. 1, pp. 7-11, Mar 2008.

[69] C. Owsley, G. R. Jackson, M. White, R. Feist, and D. Edwards, "Delays in rod-mediated dark adaptation in early age-related maculopathy," *Ophthalmology,* vol. 108, pp. 1196-202, Jul 2001.

[70] G. R. Jackson, I. U. Scott, I. K. Kim, D. A. Quillen, A. Iannaccone, and J. G. Edwards, "Diagnostic sensitivity and specificity of dark adaptometry for detection of age-related macular degeneration," *Invest Ophthalmol Vis Sci,* vol. 55, pp. 1427-31, Mar 2014.

[71] C. D. Lu, B. Lee, J. Schottenhamml, A. Maier, E. N. Pugh, Jr., and J. G. Fujimoto, "Photoreceptor Layer Thickness Changes During Dark Adaptation Observed With Ultrahigh-Resolution Optical Coherence Tomography," *Invest Ophthalmol Vis Sci,* vol. 58, pp. 4632-4643, Sep 1 2017.

[72] G. Wollstein, L. Kagemann, R. A. Bilonick, H. Ishikawa, L. S. Folio, M. L. Gabriele, A. K. Ungar, J. S. Duker, J. G. Fujimoto, and J. S. Schuman, "Retinal nerve fibre layer and

visual function loss in glaucoma: the tipping point," *Br J Ophthalmol,* vol. 96, pp. 47-52, Jan 2012.

Chapter 2
Methods for en Face Doppler OCT Measurement of Total Retinal Blood Flow

2.1 Previous Work

Early work in total retinal blood flow (TRBF) measurement using en face Doppler OCT delivered promising results, demonstrating feasibility of accurate TRBF assessment using high-speed FD-OCT instruments [1]. However, as the volume repetition rate was not considerably higher than the heart rate, the technique's robustness against variables such as eye motion and vascular geometry at the optic nerve head (ONH) remained unclear. En face Doppler OCT TRBF measurement with volume repetition rate high enough to achieve 5 or more volumes per cardiac cycle was first demonstrated in rat retina, using a UHR SD-OCT system operating at 244 kHz A-scan rate [2]. Since the heart rate of a rat can exceed 300 beats per minute even under anesthesia, the scan pattern was optimized for high volume repetition rate. Raster scans covering 200 μm × 200 μm area at the rat optic nerve head with 150 × 25 A-scans were repeated at 55 Hz volume repetition rate (Fig 2.1). The scan area was allowed to be small because the central retinal artery of the rat retina bulges into the vitreous at the point where it branches out radially. The scan would be aimed to the central retinal artery of the stable, anesthetized rat retina to ensure that the entire flow in the artery is covered by the scan.

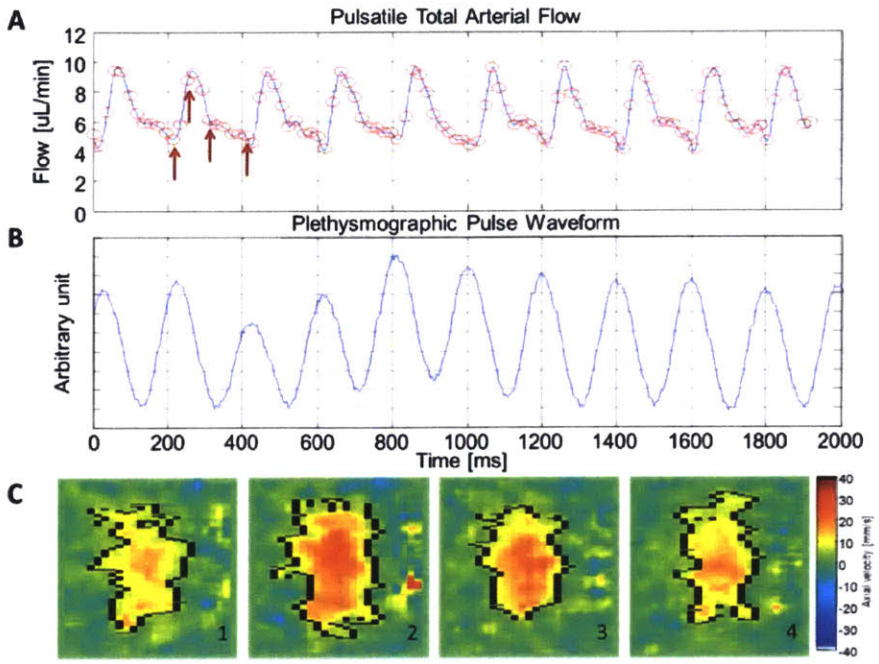

Fig. 2.1. An example of en face Doppler total retinal blood flow (TRBF) measurement in rat retina. A 200 μm × 200 μm scan area barely large enough to fit the central retinal artery was scanned rapidly scanned at 55 Hz volume rep rate to resolve the pulsatile fluctuation of rat TRBF. Extracted from [2].

The software for TRBF measurement in rat eyes was remarkably simple because of the simple vessel geometry of the rat's central retinal vasculature. The software smoothed the Doppler phase with a 2D median filter, binarized the filtered image with a threshold, and calculated the sum of Doppler phase inside the largest connected component in the binary map. Since the scan area was small, the largest area with high Doppler phase corresponded to the central retinal artery in a great majority of the data. In the same article, TRBF measurement in human retina was also reported with the same system using an 800 μm × 800 μm scan area. The scan area was barely large enough for a one-time demonstration in one healthy eye; however, considering that the segmented blood flow areas were nearly moving outside of the scan area, the scan pattern would not be applicable to general group of healthy and diseased eyes for reliable measurement of TRBF. Since the vessel geometry of the human ONH varies widely across

different subjects, faster A-scan rate would be desired to expand the scan area so that a wider range of ONH shapes could be eligible for TRBF measurement.

2.2 Doppler Phase and Doppler Phase Noise

Prior to describing the en face Doppler OCT image processing software, it is necessary to understand the basic principles of Doppler phase and its noise characteristics. The term "Doppler phase" refers to the phase shift between the two A-scans taken at (nearly) the same location but at two different time points. An article by Makita et al. [3] discusses statistical characteristics of Doppler phase in detail; the information in this section was also largely taken from Makita's analysis. Doppler phase can be best understood under the framework of the complex metric called the normalized field autocorrelation (FAC) function,

$$a(z,\tau)=\frac{\left\langle S_{FD}(z,t)S_{FD}^{*}(z,t-\tau)\right\rangle_{t}}{\left\langle \left|S_{FD}(z,t)\right|^{2}\right\rangle_{t}}=\rho(z)e^{\Delta\phi_{0}(z)} \tag{2.1}$$

where $S_{FD}(z,t)$ is FD-OCT A-scan recorded at time t, which is the sum of true noise-free OCT signal and complex Gaussian shot noise. $\langle\cdot\rangle_{t}$ is the time-averaging operator for calculating the expected value; this can be replaced by lateral spatial filtering in the context of en face Doppler OCT. τ is the measurement interval. The expression $\rho(z)e^{\Delta\phi_{0}(z)}$ is the magnitude-phase decomposition of FAC.

Considering the complex Gaussian distribution of shot noise, the expected value and standard deviation of the Doppler phase, $\Delta\phi$, can be derived as below:

$$E[\Delta\phi]=\frac{\rho\sin\Delta\phi_{0}}{\sqrt{1-\rho^{2}\cos^{2}\Delta\phi_{0}}}\cos^{-1}(\rho\cos\Delta\phi_{0}) \tag{2.2}$$

$$\sigma_{\Delta\phi} = \sqrt{\frac{1-\rho^2}{1-\rho^2\cos^2\Delta\phi_0}\left[\frac{\pi}{2} - \sin^{-1}(\rho\cos\Delta\phi_0)\right]^2 + \frac{\pi^2}{12} - \frac{\mathrm{Li}_2(\rho^2)}{2}} \tag{2.3}$$

where Li_2 is Euler's dilogarithm. For the special case of fully uncorrelated measurements, $\rho = 0$, $E[\Delta\phi] = 0$ and $\sigma_{\Delta\phi} = \pi/\sqrt{3}$, which correspond to uniform distribution in $[-\pi, \pi]$. In contrast, for the special case of perfectly correlated measurements, $\rho = 1$, $E[\Delta\phi] = \Delta\phi_0$ and $\sigma_{\Delta\phi} = 0$. In practical imaging situation, magnitude of the FAC can be anything between 0 and 1 depending on the sampling interval between two A-scans in comparison and signal strength in the very pixel we are interested in. If the two A-scans are taken at two locations far away from each other, they cannot be assumed to be coming from the same group of scattering particles and would result in low FAC magnitude. If the signal is weak, the noise would dominate the detected signal, lowering the FAC magnitude. Therefore, in order to have accurate TRBF measurements from en face Doppler OCT, it is necessary both to design a scan pattern which samples the area densely enough and to filter out the low-signal pixels in post-processing.

2.3 Scan Pattern

Reliable and accurate measurement of TRBF largely depends on choosing an appropriate scan pattern. In the process of choosing the scan pattern for en face Doppler OCT, there are three constraints which trade off with one another: the volume repetition rate, the A-scan sampling density, and the scan area.

First, the volume repetition rate must be high enough so that multiple volumes can be acquired in one cardiac cycle. Adequate temporal sampling of the pulsatile fluctuation of the instantaneous TRBF is critical for accurate estimation of the mean TRBF because continuous sampling at a slow volumetric repetition rate may cause bias in the measurement because of

over-representation of certain parts of the cardiac cycle. This is analogous to aliasing effects in discrete-time signal processing theory and can be prevented by having sufficiently high volume repetition rate. After imaging several healthy young subjects, the lower bound on the volume repetition rate was determined to be six volumes per second.

Second, the A-scan sampling density must be high enough to ensure the Doppler phase signal is clean. The Doppler phase noise equation (2.3) suggests that amplitude correlation between the A-scans is important to keep the Doppler phase signal clean. The correlation is lower for moving particles than for a stationary tissue; therefore, the sampling density of the A-scans must be determined based on the Doppler phase signal quality in the fast-flowing major blood vessels. After experimenting with a series of different scan patterns, the A-scan sampling interval was determined to be 2.5 μm. This was approximately 1/8 of the lateral resolution defined by the full-width at half-maximum of the lateral point spread function.

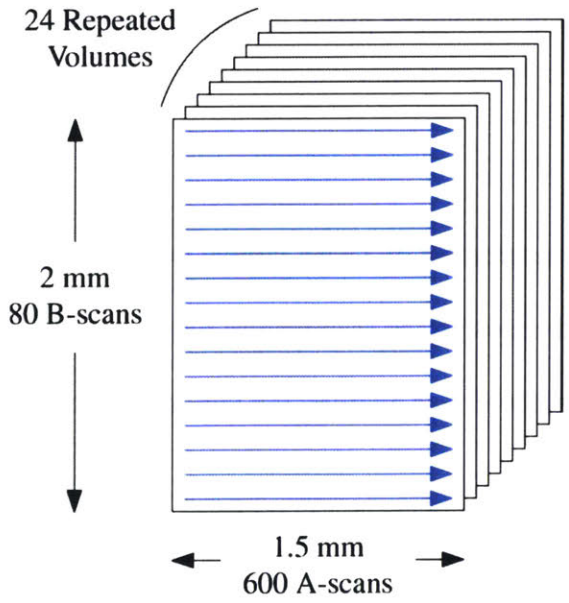

Fig. 2.2. Scan pattern used for en face Doppler total retinal blood flow measurement in human retina.

Lastly, the scan area was determined at 1.5 mm wide in the horizontal direction and 2 mm tall in the vertical direction. The scan height was deliberately chosen to be larger than the width because the major retinal blood vessels generally bifurcate into superior and inferior branches before they branch into smaller arterioles or venules. In order to cover the area of the major retinal blood vessels inside the optic disc, the height of the scan was set at 2 mm.

In summary, a volumetric scan with 600×80 A-scans covering 1.5 mm×2 mm area at the optic disc was rapidly repeated 24 times to measure pulsatile TRBF. Given the axial scan rate of 400 kHz, the total acquisition time was about 3.4 seconds and the volume repetition rate was 7.1 volumes per second.

2.4 Software Methods for Calculation of TRBF

2.4.1 Overview

There are several major challenges that hinder en face Doppler OCT measurement of TRBF: inter-individual variation in central retinal vessel geometry, high signal attenuation inside blood vessels, and Doppler phase wrapping—discontinuous jumps in between $\pm\pi$ phase—in fast-flowing vessels. This section outlines the image processing methods developed to mitigate these limitations.

The overarching strategy in en face Doppler OCT TRBF processing is to avoid overestimation or underestimation of TRBF. We aim to accurately measure volumetric blood flow rate, without missing a major blood vessel or failing to detect low blood flow velocities in diastolic phase, while not mistaking phase artifacts or noise for blood flow. This section will describe the overall structure of the TRBF calculation algorithm and the details of each internal step. The algorithm is carefully designed to overcome the technical challenges of Doppler OCT

inherent to its phase-sensitive nature and each step is intended to prevent erroneous flow calculation in eyes with either high or low retinal blood flow velocities and with various ONH structures.

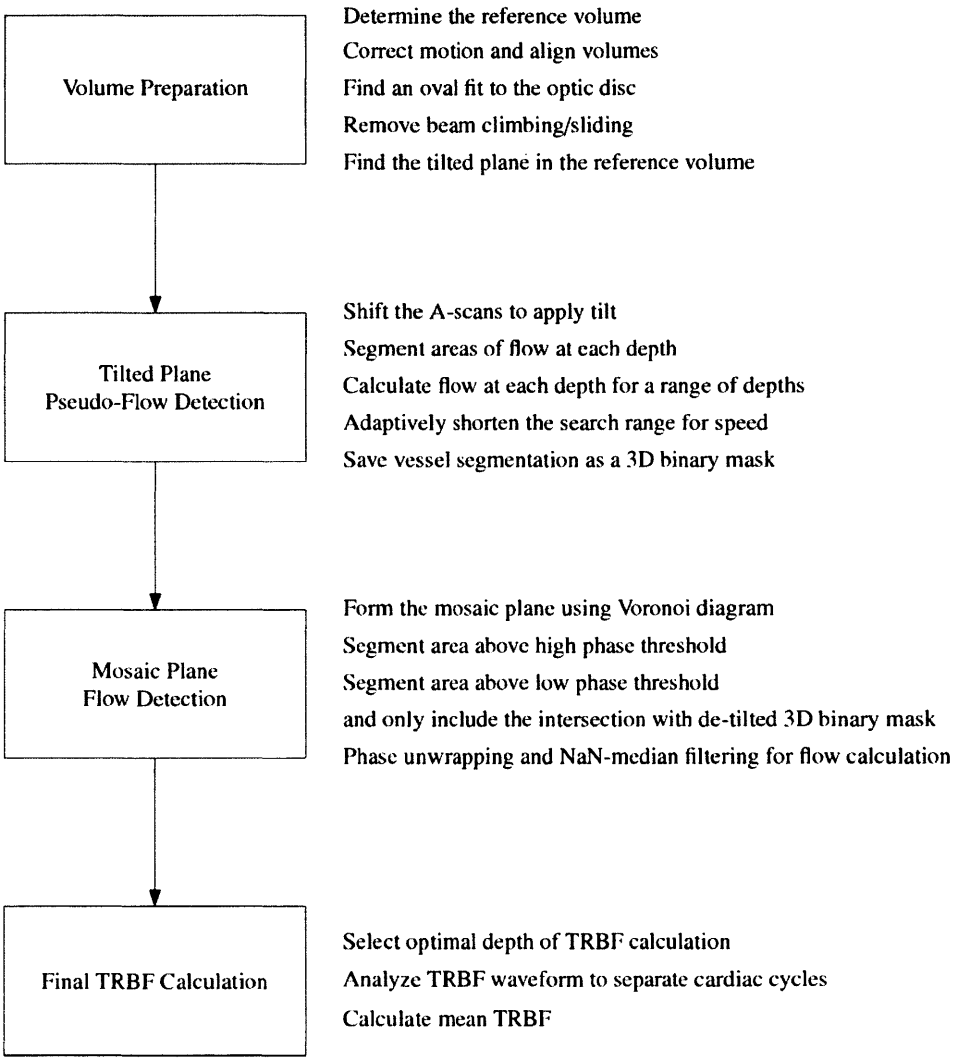

Fig. 2.3. Major image processing procedures for TRBF calculation and detailed steps in each procedure.

The chart in Fig. 2.3 shows the large-scale processes and detailed steps in the TRBF calculation software. The basic approach of blood flow segmentation is to select an en face plane and segment areas with high filtered phase values. Arteries and veins can be distinguished by looking at the sign of the phase in the areas near the boundary of the segmented area. This

process can be repeated over a range of depths to determine the optimal en face plane for complete detection of TRBF. In principle, this process may seem simple but in practice, each step must be deliberately designed to minimize segmentation errors. The following sections will describe the procedural details of each step in the software and its impact on enhancing the accuracy of TRBF calculation.

2.4.2 Volume Preparation

2.4.2.1 Cross-Correlation-Based Lateral Motion Correction

Before beginning any processing on the Doppler phase images, software corrects for lateral eye motion by selecting a reference volume and aligning the others based on cross-correlation of depth projection images. First, the reference volume was selected based on the correlation matrix. Correlation matrix is a square matrix with number of rows and columns equal to the number of volume repeats. The (i, j) entry of the correlation matrix corresponds to the maximum cross-correlation between the depth projections of the i^{th} and j^{th} volumes. Assuming that saccades occur randomly in a relatively small number of volumes, the volume with highest mean correlation with other volumes is selected as the reference volume. Then, the B-scans in the other volumes are shifted laterally to match the B-scans of the reference volume. For each B-scan, the fundus projection of five-B-scan-thick slab centered at the current B-scan was cross-correlated with the fundus projection of the reference volume. Based on the peak position of the cross-correlation, the x- and y-shifts of the B-scan is determined. Fig. 2.4 shows an example of volumes pre- and post- motion correction. After the B-scans in all volumes are aligned to the reference volume laterally, they are also aligned axially using the segmented vitreoretinal

interface. This process allows all 24 volumes to be closely matched to the reference volume and remove uncertainty introduced by eye motion.

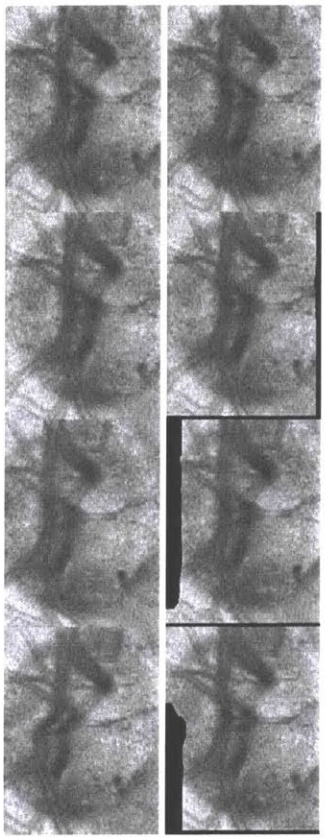

Fig. 2.4. En face log-of-amplitude projections of four volumes (left) before motion correction and (right) after motion correction.

The B-scan shifting for motion correction only applies integer amounts of lateral shifts because Doppler phase data is not preserved if any subpixel shifts are applied. Phase operator is essentially the imaginary part of the logarithm of an analytic function and is not a linear operator. However, subpixel shifts are allowed if the TRBF analysis is not performed on the radial coordinates of amplitude and Doppler phase but performed on the Cartesian coordinates of real and imaginary components of FAC discussed in section 2.2. Advantage of using field autocorrelation will be discussed later in *Field Autocorrelation* section.

2.4.2.2 Segmentation of the Optic Disc Area

Confining the flow measurement within the optic disc area, namely the area circumscribed by the neuroretinal rim, is a solution to a very common error—the double-counting of blood flow. In a considerable number of individuals, the vitreoretinal interface at the neuroretinal rim, or in the entire optic nerve head, can bulge into the retina, causing arching of the major branches of central retinal artery vessels (Fig. 2.5). As a result of this arching, the same vessel can be detected at two different locations—as flow into the en face plane at one location and as flow out of the en face plane at another location. This generally leads to overestimation of blood flow because venous flow outside of optic disc area can be mistaken as arterial flow inside the optic disc area and vice versa. Such double-measurement is one of many ways in which variations in vessel geometry can cause complications in TRBF measurements.

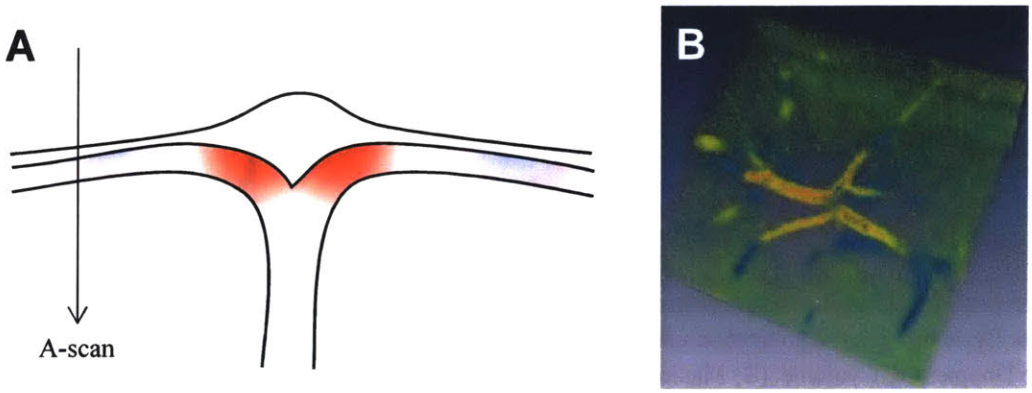

Fig. 2.5. (A) A simplified illustration of a human optic nerve head cross-section with areas of detectable axial flow velocity colored in red. (B) An example of clear vessel arching in 3 mm × 3 mm area, extracted from [1]. Doppler velocity is detectable only if the vessel angle is sufficiently steep and the signal attenuation is not severe. Moreover, the same vessel may be detected at two places, presenting flow in opposite directions.

Since the vessels tend to arch around at the edge of the optic disc, segmenting the optic disc boundary and excluding Doppler phase outside of the boundary can be a simple solution to this problem. In OCT, the optic disc area can be best characterized by areas without RPE; therefore, detecting the presence of RPE is the first step of segmenting optic disc area. This can be done by

finding the maximum value of the axial gradient below the vitreoretinal interface. The two brightest layers in a retinal OCT image are the topmost retinal nerve fiber layer and the photoreceptor complex, from the inner and outer segments junction to the RPE; if a certain depth posterior to the vitreoretinal interface is excluded, then, the only layer that can cause large positive values of axial gradient is the photoreceptor complex. The current implementation of optic disc area segmentation takes a 3D Gaussian-filtered volume and generates an en face map of the maximum positive gradient under the vitreoretinal interface. With simple histogram analysis and oval fitting using RANSAC algorithm, the elliptical trace which follows the rough shape of the optic disc is determined (Fig. 2.6). All Doppler phase outside of this region is set to zero, forcing the measurement of blood flow to be limited within the optic disc area.

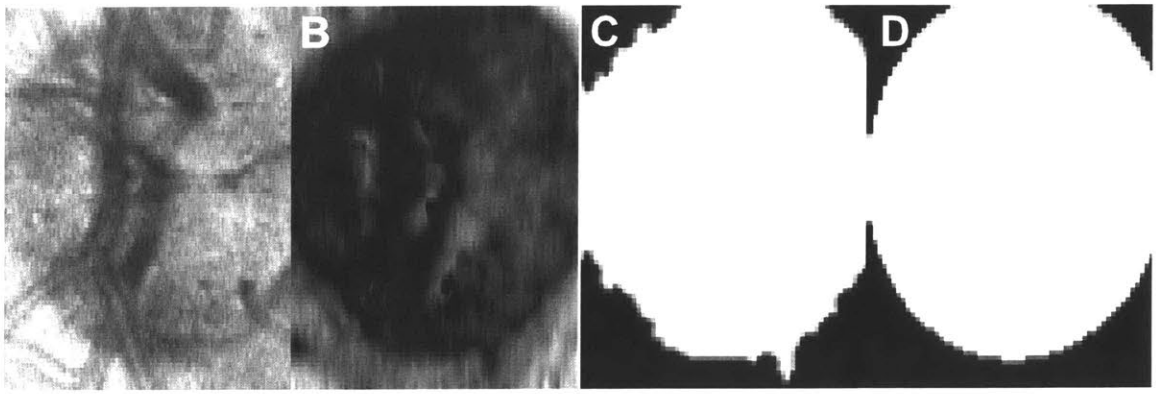

Fig. 2.6. Optic disc area segmentation using RPE detection. (A) Full log-of-amplitude projection of an en face Doppler OCT volume. (B) Maximum dark-to-light gradient under segmented vitreoretinal interface. (C) Detected optic disc boundary using histogram analysis. (D) Least-square oval fit of the optic disc boundary using RANSAC algorithm.

2.4.2.3 Reducing Beam Climbing and Beam Sliding Artifacts

Doppler phase artifacts are inevitable source of error in any form of phase-based Doppler OCT with confocal scanning geometry. When there are dense packets of scattering particles, the packets can be optically seen as a large, continuous reflecting surface like a mirror and any variation in optical path length to the surface will introduce Doppler phase into image. For

example, any topographical variation in the vitreoretinal surface will introduce "beam climbing" or "beam sliding" Doppler phase artifacts.

The phase artifact is most pronounced at highly scattering, laterally continuous surfaces with a slope. Recall that the OCT signal has the phase delay term e^{-j2kz} where z is the axial coordinate. If the optical path length to the surface decreases as the beam scans, positive phase artifact (beam climbing) will appear. Conversely, if the optical path length to the surface decreases as the beam scans, negative phase artifact (beam sliding) will appear. This is because the phase delay varies in between adjacent A-scans based on the slope of the surfaces. As shown in Fig. 2.7, positive Doppler phase appears with upward slope, whereas negative Doppler phase appears with downward slope, suggesting that the term e^{-j2kz} is dominating the phase artifact.

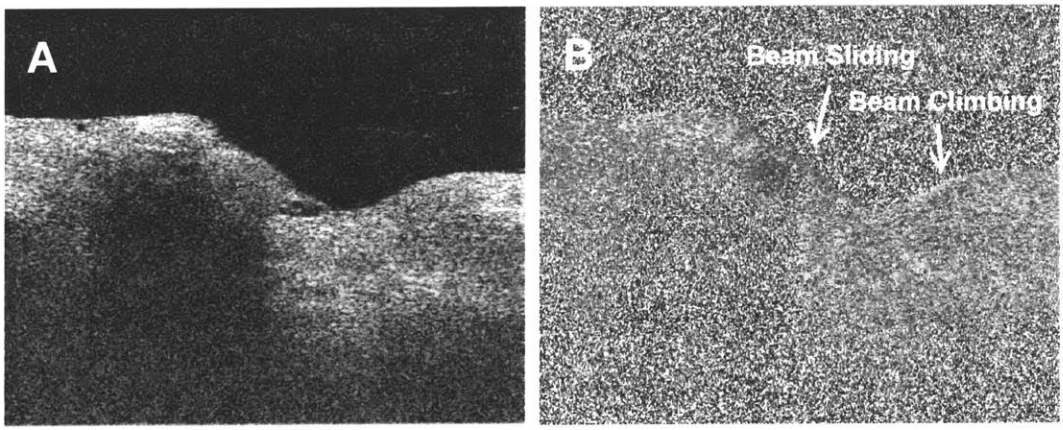

Fig. 2.7. Beam sliding and climbing effects. (A) Log of OCT amplitude of a B-scan taken at the optic nerve head. The vitreoretinal interface appears to have slopes. (B) Negative Doppler phase was measured at areas with negative slope (beam sliding) and positive Doppler phase was measured at areas with positive slope (beam climbing).

The simplest way to remove the beam climbing and beam sliding artifacts is to detect the highly reflecting or scattering surfaces and remove the phase at where the surfaces have a steep slope. Similar to the method used in RPE detection in *Optic Disc Area Segmentation*, detecting high axial gradient in a Gaussian-filtered image would be a simple method to detect possible areas of beam climbing/sliding artifact. In our implementation, the segmented vitreoretinal

interface was morphologically expanded (MATLAB imdilate) horizontally by 10 pixels and all phase in the area was removed.

2.4.2.4 Determination of the Reference Tilted Plane

The next step is to determine the "reference tilted plane" in the reference volume, the volume chosen in *Cross-Correlation-Based Lateral Motion Correction.* Tilted plane pseudo-flow detection is a solution to the individual variation in vessel geometry across different subjects. Because of limited penetration of the OCT signal into the optic nerve, blood vessels are only measurable near the vitreoretinal interface, typically within 100 μm range. Moreover, the attenuation of the OCT signal is high in blood, complicating detection of blood flow in the deeper measuring points into the optic nerve where the central retinal artery or vein lies axially. Therefore, the major branch retinal arteries or veins must be measured at points where they appear oblique to the illumination beam and such measuring points can be at different axial locations depending on the vessel geometry inside the optic nerve head.

Hence, if the axial locations of the vessels are inconsistent because of ONH structure such as cupping, then, it is impossible to detect blood flow in all arteries or all veins in a single en face plane. Therefore, there must be an approach to segment each vessel at its optimal en face plane for flow detection. Such approach is not necessary in the rat retina, since the central retinal artery is usually exposed near the vitreoretinal interface before it branches out radially. However, in the human retina, the vascular structure of the central retinal artery or vein can be quite different depending on the individual. In particular, the point of bifurcation can be exposed near the vitreoretinal interface or buried deeper in the optic nerve. Moreover, additional vascular branching to macular and peripheral direction may take place inside the optic disc. These

uncertainties require the human TRBF calculation software to be more flexible than the simple software for rat retina.

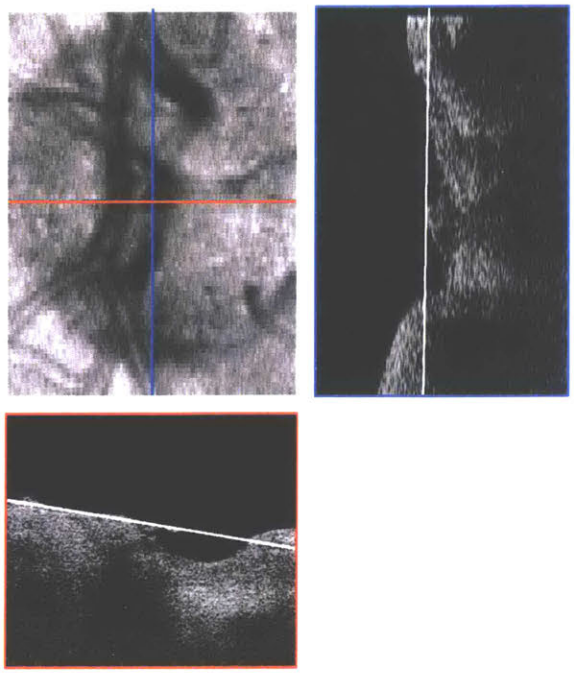

Fig. 2.8. Horizontal central B-scan and vertical central B-scan with their respective intersections with the reference tilted plane, drawn in white.

Tilted plane pseudo-flow detection attempts to detect all arteries or all veins in one plane by finding the reference tilted plane, a least-mean-square planar fit to the segmented vitreoretinal interface in the scan area, and shifting the volumetric data with respect to the reference tilted plane. Since the OCT signal penetrates only up to certain depth into the optic nerve, If the topography of the segmented vitreoretinal interface is represented by the two-dimensional function $f(x, y)$, then, the reference tilted plane $p(x, y) = ax + by + c$ can be determined by the following equations,

$$\begin{aligned}
&\frac{\partial}{\partial a}\sum_n [f(x_n,y_n)-ax_n-by_n-c]^2=0\\
&\frac{\partial}{\partial b}\sum_n [f(x_n,y_n)-ax_n-by_n-c]^2=0\\
&\frac{\partial}{\partial c}\sum_n [f(x_n,y_n)-ax_n-by_n-c]^2=0
\end{aligned} \tag{2.4}$$

which further simplifies into

$$\begin{aligned}
&-\sum_n x_n f(x_n,y_n)+a\sum_n x_n^2+b\sum_n x_n y_n+c\sum_n x_n=0\\
&-\sum_n y_n f(x_n,y_n)+a\sum_n x_n y_n+b\sum_n y_n^2+c\sum_n y_n=0\\
&-\sum_n f(x_n,y_n)+a\sum_n x_n+b\sum_n y_n+cN=0
\end{aligned} \tag{2.5}$$

or in the matrix form,

$$\begin{pmatrix} \sum_n x_n^2 & \sum_n x_n y_n & \sum_n x_n \\ \sum_n x_n y_n & \sum_n y_n^2 & \sum_n y_n \\ \sum_n x_n & \sum_n y_n & N \end{pmatrix} \begin{pmatrix} a \\ b \\ c \end{pmatrix} = \begin{pmatrix} \sum_n x_n f(x_n,y_n) \\ \sum_n y_n f(x_n,y_n) \\ \sum_n f(x_n,y_n) \end{pmatrix} \tag{2.6}$$

once the coefficients a, b, c are determined, the volumetric data of amplitude and Doppler phase are axially translated to introduce the intended tilt and shift in the dataset.

Tilted plane has two characteristics suitable for detecting vessels at different axial positions simultaneously. First, since it generally follows the topography of the vitreoretinal interface, compensating for possible large jump between the axial positions of the vessels. Second, its slope is constant and relatively small, minimizing the risk of small errors in vitreoretinal interface segmentation disturbing the blood flow detection. Fig. 2.8 shows the central B-scans along the fast-scan and slow-scan directions with the white lines representing their intersections with the reference tilted plane.

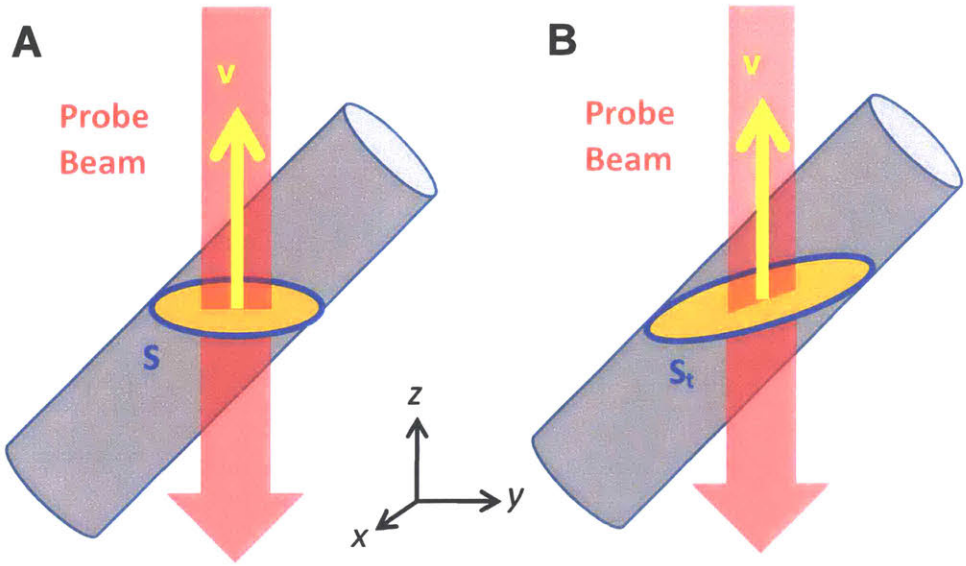

Fig. 2.9. Schematic description of why (B) tilted plane pseudo-flow cannot be equal to actual flow in the (A) en face plane. Tilted plane is not perpendicular axial flow velocity, so summation of axial flow velocity on the tilted plane is not equal to the flux

Although tilted plane is useful for detecting blood vessels at different axial positions, it is not appropriate for actual calculation of blood flow because it is not perpendicular to the axial velocity component measured by Doppler phase (Fig. 2.9). This can be clearly shown by writing out the surface flow integral:

$$\begin{aligned} &\Phi = \int_S \mathbf{v}\cdot d\mathbf{S} = \int_{S_t} \mathbf{v}\cdot d\mathbf{S}_t \\ &\int_S \mathbf{v}\cdot d\mathbf{S} = \iint_S v_z dxdy \\ &\int_{S_t} \mathbf{v}\cdot d\mathbf{S}_t = \iint_{S_t} v_z dxdy + \iint_{S_t} v_x dydz + \iint_{S_t} v_y dxdz \\ &\therefore \Phi = \iint_S v_z dxdy \neq \iint_{S_t} v_z dxdy \end{aligned} \tag{2.7}$$

Therefore, the blood flow calculated on the tilted plane was named "pseudo-flow" and the corresponding segmentation was only used as *a priori* guide information for actual segmentation made on another special plane called "mosaic plane." Mosaic plane is an assortment of plane fragments piecewise perpendicular to the illumination, which would be described in greater detail in *Mosaic Plane Flow Detection.*

2.4.3 Tilted Plane Pseudo-Flow Detection

As discussed in the previous section, preliminary segmentation of blood flow area and rough calculation of total retinal blood flow is performed on the tilted planes with a range of axial offsets from the reference tilted plane. Tilted plane pseudo-flow detection increases the possibility of measuring all blood vessels in one depth slice and the segmented blood flow area can serve as a guide for the actual segmentation in mosaic plane flow detection. This section describes key filtering steps and geometric operations performed on the flow binary masks for accurate segmentation of arterial or venous flow area.

2.4.3.1 Doppler Phase Noise Filtering

Doppler phase noise is one of the major stumbling blocks for accurate blood flow segmentation. This section will cover the theoretical characterization of the Doppler phase noise and practical approaches to suppress or to avoid them. As described in Section 2.2, the Doppler phase noise intensifies when the amplitude is low or the correlation between the two scans in comparison is low. Doppler phase noise corresponding to a pure Gaussian white noise complex OCT signal would be a uniform noise distributed from $-\pi$ to $+\pi$. Consequently, Doppler phase noise has a salt-and-pepper like nature. OCT image is a superposition of complex backscattered optical field from individual scattering particles, often referred as speckles. If there is a dark spot inside a densely packed group of speckles, a uniform, random Doppler phase value will appear sporadically in either stationary tissue or blood vessels. Linear filtering is not applicable for salt-and-pepper noise because a single pixel outlier will affect the filtered data in the nearby pixels. Instead, nonlinear filters such as median filter or amplitude-assisted filtering is more appropriate.

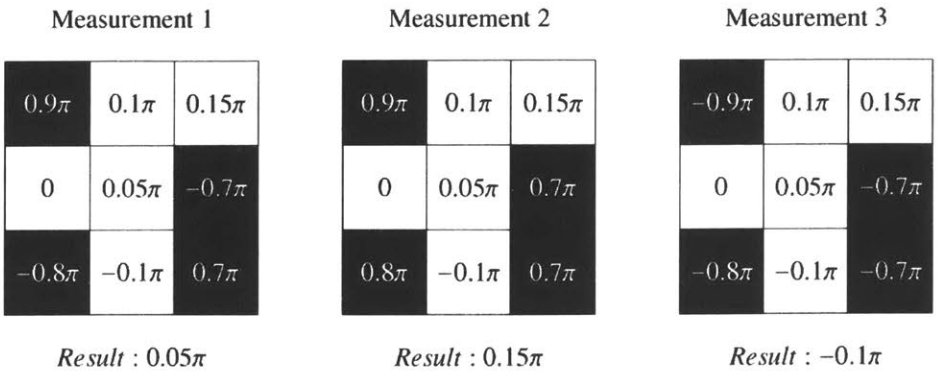

Fig. 2.10. A possible scenario of a simple 2D median filtering resulting in three different filtered Doppler phase values for three different measurements of the same sample. Randomness of Doppler phase of pure Gaussian noise can influence the filtered result significantly.

3D median filtering is the simplest approach to remove the salt-and-pepper Doppler phase noise. Median filter effectively removes a small number of outliers because the median value does not change regardless of small variations on the actual value of the outliers. However, if the number of outliers, namely the pixels associated with low OCT signal amplitude, is comparable to the number of high-OCT-amplitude pixels that represent the axial velocity, then the output becomes increasingly unstable. For instance, assume that the median filter is finding the median of Doppler phase in a filter kernel with nine pixels as shown in Fig. 2.10. If four of the selected pixels are associated with low OCT signal amplitude, it is uncertain that the low-amplitude pixels will have large magnitudes of positive or negative phase, as all of them may have values close to π or - π. It is also possible for these low-amplitude pixels to have phase values close to zero. Therefore, simple 3D median filter generates uncertainty in the filtered data, more so to data with higher ratio of low-amplitude pixels.

Therefore, a filtering process which excludes or suppresses the influence of the low-amplitude pixels would be more desirable than simple 3D median filter. Such filtering process may involve some amplitude thresholding before applying the filter. A median filter which excludes the Doppler phase from the low-amplitude pixels is a good example. This filter, called

3D NaN-median filter, was used *Mosaic Plane Flow Detection* step for calculating final values of instantaneous TRBF. NaN is a MATLAB identifier which stands for "not a number," and represents the values that can be excluded in numerical operations. The NaN identifier can be assigned to Doppler phase of the pixels with low amplitude and then the Doppler phase image can be filtered using 2D NaN-median. For tilted plane pseudo-flow detection, the usage of 3D NaN-median filter was avoided due to its high computational need. Instead, the software first computed the 1D NaN-median of Doppler phase values in each lateral position over three consecutive tilted planes along the axial direction; if the Doppler phase values in all three pixels are NaN, then the lateral pixel was filled with zero Doppler phase. Then, 2D median filter was applied to the 1D NaN-median filtered Doppler phase to generate en face Doppler phase map for tilted plane pseudo-flow detection. Although setting the Doppler phase to zero can introduce bias toward zero, the method described above was sufficient for preliminary segmentation of blood flow area on the tilted plane.

Another problem with median filtering is its computational load due to its nonlinear nature. Fortunately, MATLAB provides a function for GPU-accelerated 2D median filter in its function package. One limitation of this function was the kernel size, which has to be a square with odd number of pixels. In order to utilize this function to achieve further improvements in processing speed, 1-dimensional median filters were applied five axial depths and nine horizontal pixels, respectively, Then, a GPU-accelerated 2D median filter with 5×5 kernel was applied to generate the filtered tilted plane Doppler phase. Note that this is not identical with finding the exact median inside the 3D kernel because of the nonlinear nature of median operator.

2.4.3.2 Artery and Vein Distinction

When a blood flow area is detected, whether the flow is arterial or venous must be determined immediately. While measuring total retinal arterial flow versus measuring total retinal venous flow can be a choice of the software user, the flow direction in a single vessel must be detected to decide if the blood flow in the vessel should be included in the measurement. Determination of flow direction may seem trivial, as for slow flow velocities, the arithmetic mean of the Doppler phase in the flow area will represent the flow direction. However, for faster flow velocities, Doppler phase can wrap around from $+\pi$ to $-\pi$ because the angle function is a multivalued analytic function with a branch cut at the negative real axis. While it is possible to unwrap phase inside a vessel, it is computationally rather expensive. Instead, the arithmetic mean of the Doppler phase near the boundary of the flow area. Assuming that the flow velocity is zero at the blood vessel wall (endothelium), the flow at the boundary of the segmented area is usually slow, and phase wrapping is unlikely to occur there. Hence, the sign of the mean Doppler phase is most likely equal to the sign of the actual axial flow velocity.

2.4.3.3 Information Forwarded to Mosaic Plane Flow Detection

There are two sets of volumetric data from tilted plane pseudo-flow detection forwarded to the next step, mosaic plane flow detection, as *a priori* guide information. First, the 3D binary map of segmented flow area at systole (maximum tilted plane pseudo-flow) is de-tilted and forwarded. Second, the extracted and filtered Doppler phase map in the tilted plane is forwarded. The 3D binary map is used for increased sensitivity in detecting blood flow in diastolic cardiac phases. The filtered Doppler phase map in the tilted plane is used for determination of center of flow

area, which is critical for formation of the mosaic plane. This will be further discussed in the following section.

2.4.4 Mosaic Plane Flow Detection

2.4.4.1 The Mosaic Plane

The term "mosaic plane" is used to denote a fragmented, piecewise-lateral en face plane, where each fragment contains one large artery or vein, depending on the user's choice of calculating arterial or venous flow calculation. The core idea behind the usage of mosaic plane is that if all major arteries or all major veins are detected in one tilted plane, then it is possible to measure accurate flow, not tilted plane pseudo-flow, by extracting the Doppler phase data in the en face planes at the specific axial positions where the blood vessel was found in tilted plane pseudo-flow detection. Using this information, it is possible to calculate blood flow accurately by measuring blood vessels at various axial and lateral positions.

2.4.4.2 Voronoi Diagrams

Mathematical foundation of the mosaic plane is the Voronoi diagram, a partition of a plane based on the distance from a given set of points. The set of n points, called seeds, is specified beforehand; then, the plane is divided into n sections comprising all points that are closer to a particular seed than all other seeds. Fig. 2.11 shows an example of Voronoi partition of a square area by 20 seeds.

Mosaic plane formation using Voronoi diagram is powerful for accelerated total retinal blood flow calculation because it allows C-scan cross-sections of all arteries or veins at different axial positions to be accurately represented in a single image without clipping parts of the blood flow

area. Otherwise, nonlinear filters and geometrical operations must be applied in multiple en face planes separately for each major vessel, making the process computationally more expensive by the factor of number of vessels.

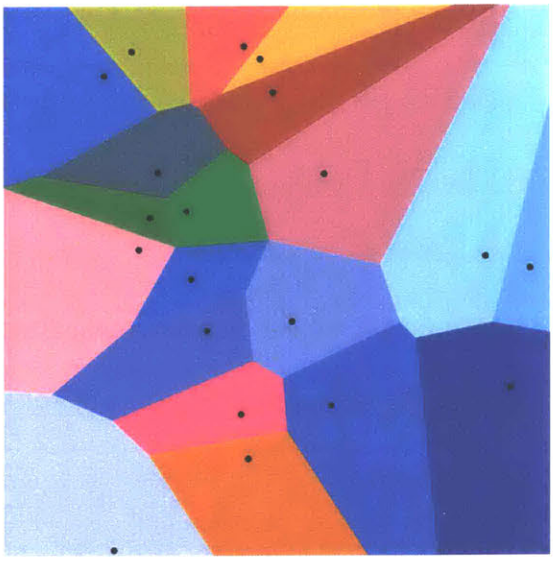

Fig. 2.11. A Voronoi diagram generated with 20 seeds and Euclidean distance system. Source: WikiMedia Commons (https://upload.wikimedia.org/wikipedia/commons/5/54/Euclidean_Voronoi_diagram.svg)

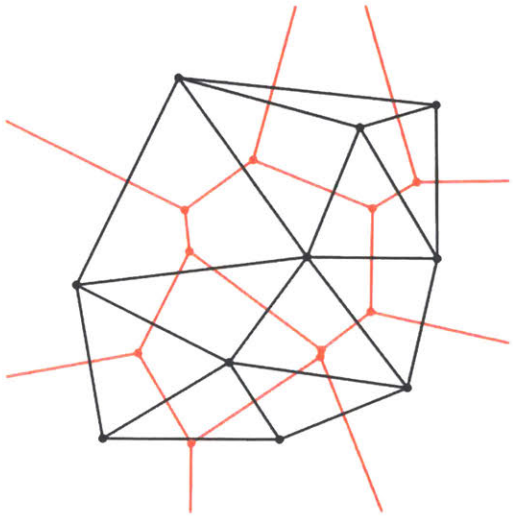

Fig. 2.12. A graph showing that Voronoi diagram (red) and Delaunay triangulation (black) form a dual pair. Voronoi diagram can be completed by connecting the perpendicular bisectors of each edge in the Delaunay triangulation. Source: WikiMedia Commons (https://upload.wikimedia.org/wikipedia/commons/5/56/Delaunay_Voronoi.svg)

An efficient tool to express, store, or determine a Voronoi diagram is its corresponding dual, the Delaunay triangulation. Delaunay triangulation is a complete triangular subdivision of a plane by seeds with no triangle lying within the circumcircle of another triangle. Each segment of Delaunay triangulation has one-to-one correspondence to an edge of a Voronoi cell, such that the perpendicular bisector of a Delaunay triangulation segment is equal to an edge of a Voronoi cell (Fig. 2.12). MATLAB has a built-in function `delaunayTriangulation` which finds the Delaunay triangulation of a given set of seeds; once the `delaunayTriangulation` object is generated, its corresponding Voronoi diagram can be found by calling the intra-class method `voronoiDiagram`. Fig. 2.13 shows an example of Doppler phase maps of a mosaic plane with segmented flow area indicated with black lines. The Voronoi partitions indicated by the colored diagram were generated with the geometrical centers of each segmented area as seeds.

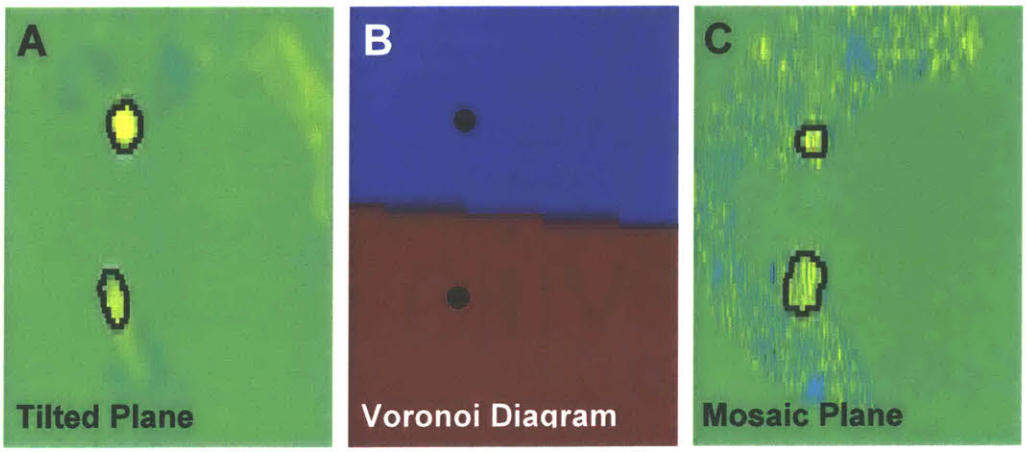

Fig. 2.13. (A) Segmented arterial blood flow area in a tilted plane. (B) Voronoi diagram using the geometrical centers of the segmented blood flow area as seeds. (C) En face plane slices (C-scans) at the depth where the flow was detected are extracted and combined to form the mosaic plane. Note that the vessel shape in (A) and (C) are different due to the tilt.

When calculating blood flow in the mosaic plane, 3D NaN-median filter was used exclusively inside the segmented flow area. It is not straightforward, at least in the framework of MATLAB, to GPU-accelerate the 3D NaN-median filter. The application of this computationally expensive filter, therefore, was limited to final blood flow calculation inside the segmented blood

flow area. The total retinal blood flow was measured repeatedly, in the mosaic planes generated from the pseudo-flow segmentations in the tilted planes over a certain range of axial offset from the planar fit of the vitreoretinal interface. The total retinal blood flow was mapped as a function of axial offset for each of the 24 repeated volumes.

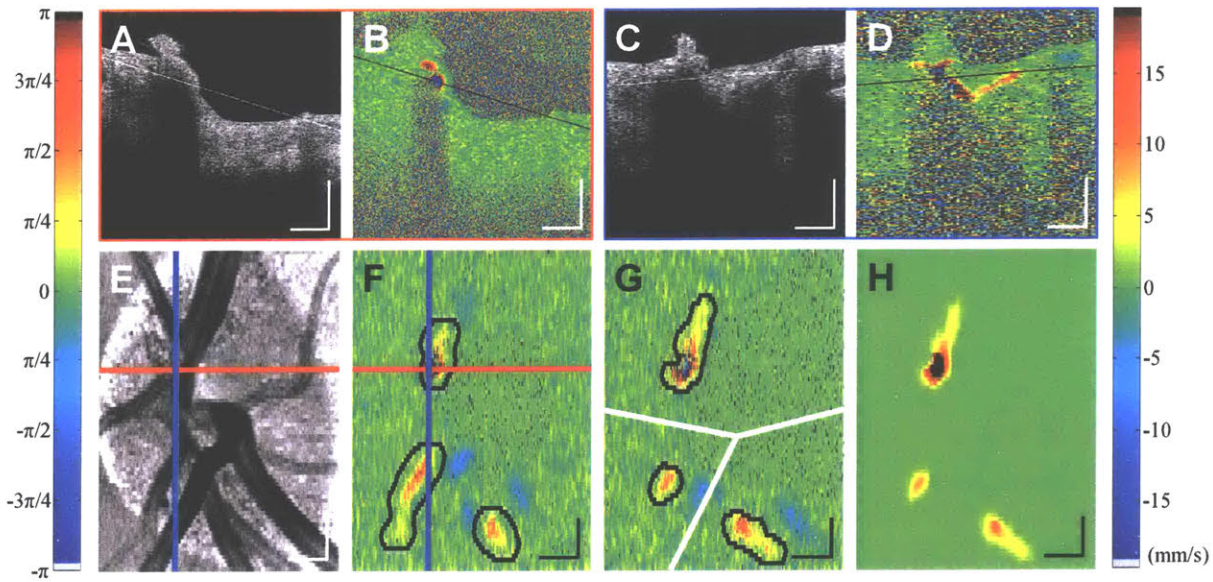

Fig. 2.14. Summary of tilted-plane-mosaic-plane analysis at 100 kHz A-scan rate. (A-D) Tilted plane marked in intensity and Doppler phase images of cross sections along the fast scan direction (A, B) and the slow scan direction (C, D). (E) Fundus projection image of the optic disc. (F) Initial vessel segmentation on the tilted plane. (G) Final vessel segmentation redone in each fragment of the mosaic plane. (H) Phase-unwrapped and noise-filtered *en face* Doppler phase map of the arterial blood flow. Scale bars: 500μm.

2.4.4.3 Phase Unwrapping

Phase wrapping refers to the discontinuous jumps in between $\pm\pi$ phase. Phase wrapping occurs because the angle function is multi-valued because $e^{j2n\pi} = 1$ for all integer n. Therefore, according to a common convention, a single-valued angle function taking values only in $[-\pi, \pi)$ is chosen. This forces a discontinuity at the negative real axis which is called a "branch cut" in complex analysis. Phase wrapping is a common artifact in Doppler OCT especially at shorter

center wavelengths, such as 840 nm, or slower imaging speeds lower than 200 kHz A-scan rate, because phase wrapping velocities are lower. Phase wrapping was less commonly observed in data acquired at 400 kHz A-scan rate with 1050 nm wavelength light source, it was still observed in a group of eyes, whose central retinal arteries were protruded and the flow inside was close to axial direction.

In order to resolve phase wrapping, we used an approach called "branch cut shifting" illustrated in Fig. 2.15. When an arterial flow area is segmented, it is safe to assume that the unwrapped "true" Doppler phase in the area would be almost entirely positive. Therefore, it is possible to extend the detectable maximum phase range from π to 2π by setting the angle function to take values in $[0, 2\pi)$ instead of $[-\pi, \pi)$. As a result, a blood vessel originally presenting with phase wrapping will have a clear phase-unwrapped en face blood flow profile as shown in Fig. 2.15 (C-D). This process does not have to be done in one step. Doppler phase inside a blood flow area can be unwrapped by iterating the following three steps: first, segment fast-flowing area with a certain Doppler phase threshold; second, fill the phase wrapping holes in the middle with morphologic operation; lastly, shift the branch cut in the Doppler phase inside the fast-flowing area by an amount slightly lower than the threshold. These steps can be iterated with increasing Doppler phase threshold until there is no phase wrapping and lead to successful phase unwrapping even in blood vessels with multiple phase wrapping.

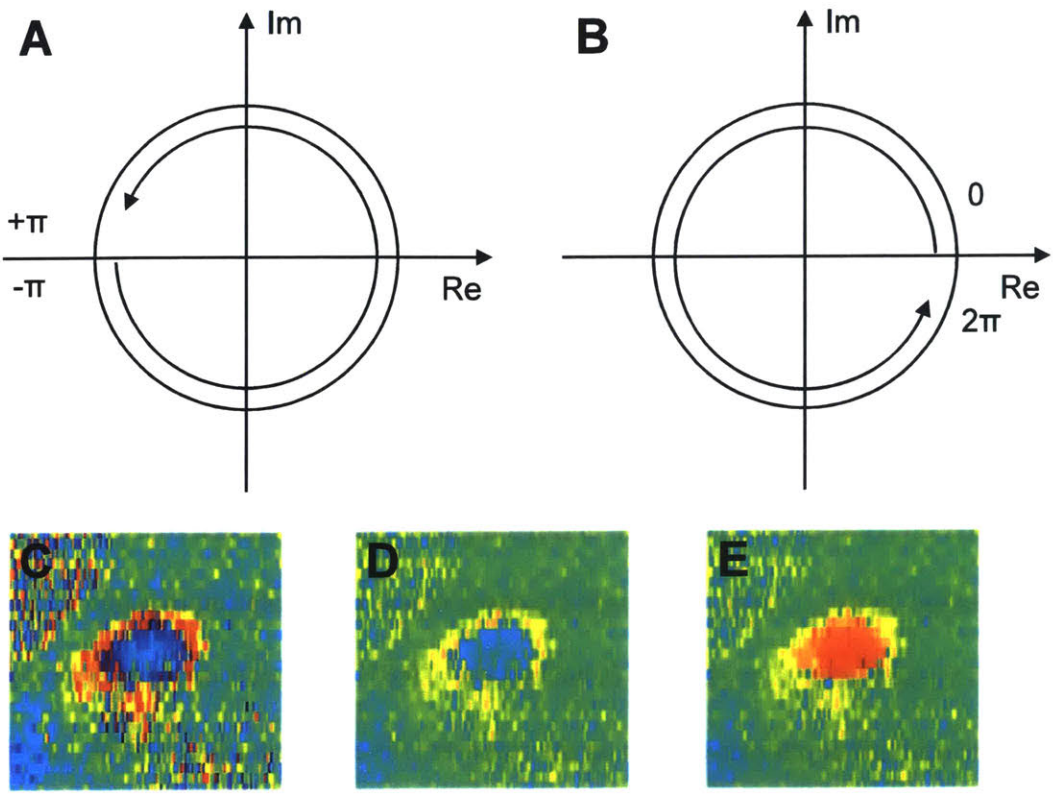

Fig. 2.15. Phase unwrapping by branch cut shifting. (A) Detectable Doppler phase range from $-\pi$ to π with typical branch cut at negative real axis. (B) Detectable Doppler phase range from 0 to 2π with shifted branch cut at positive real axis. (C) Doppler phase in a en face section (C-scan) of fast-flowing vessel drawn in $[-\pi, \pi]$ scale showing severe phase wrapping. (D) The same vessel drawn in $[-2\pi, 2\pi]$ scale. (E) The same vessel after phase wrapping drawn in $[-2\pi, 2\pi]$ scale.

2.4.5 Final Flow Calculation

The final step of calculating TRBF is rather simple. Since all of 24 repeated volumes are co-registered to the same tissue coordinates, the blood flow can be detected at relatively consistent axial positions with respect to the reference tilted plane. It is better to force the axial measurement position of TRBF to be consistent in all 24 volumes than taking the alternative option of finding the maximum detected TRBF in each volume because, if the software searches for the axial position of maximum TRBF measurement in each volume separately, the measurement depth would be shallower at systoles and deeper at diastoles. Since the axial scan

rate is high, the axial flow velocities can correspond to small Doppler phase, less than 0.1 radians, at diastolic cardiac phases even in major retinal arteries or veins. Then, the maximum measurement of TRBF would be at relatively deep axial positions into the optic nerve, where the vessels lie closer to the axial direction. In contrast, the maximum TRBF would be measured at shallow depths at systolic cardiac phases because of higher vessel visibility. Since this positional variation of TRBF measurement is not desirable, we force the measurement position to be relatively consistent. First, TRBF as a function of offset from the reference tilted plane was averaged across all 24 volumes. Then, the optimal depth offset was chosen by finding the maximum average TRBF. Lastly, to prevent the cases where segmentation in a few number of volumes have missed vessels, maximum instantaneous TRBF in a small depth offset range centered at the optimal depth was chosen as the representative instantaneous TRBF, per each volume. The resulting pulsatile total retinal arterial/venous blood flow was plotted as a waveform and saved for future data review. The waveform goes through simple Fourier analysis to determine the heart rate and sectioned into about one to four cardiac cycles. Mean TRBF is calculated as the mean of instantaneous flow over integer number of cardiac cycles.

2.4.6 Discussion

2.4.6.1 Measurement Repeatability

Since en face Doppler OCT is a newly introduced technique for TRBF measurement, it must be validated against the gold standard. Bidirectional laser Doppler velocimetry (BLDV), mentioned in Chapter 1, would be the most appropriate reference measurement because other conventional techniques cannot measure volumetric flow rate. However, BLDV does not yield highly repeatable measurements in itself, possibly because the error in Doppler frequency shift can be

magnified by the trigonometric back-calculation into blood flow velocity. The two illumination beams make a small angle at the retina; hence, a small error in Doppler shift can make a large error in final calculation of TRBF. Luksch et al. evaluated the repeatability of TRBF assessment using a commercial BLDV (Oculix 4000) in 16 eyes of 16 healthy subjects over a 12-hour period and found that the coefficient of variation (COV) of five measurements for each of the 16 healthy subjects was 18.5 ± 6.3% [4]. Since the five measurements were repeated over a 12-hour time period with 3-hour intervals, the fixed effect of diurnal fluctuation of TRBF and the random effect of measurement error could have been mixed in this evaluation; however, considering that the average of mean TRBF in the 16 subjects did not show statistically significant change between any two time points, the COV was likely to be largely contributed by the measurement error. In addition, Luksch et al. also evaluated the COV of venous flow velocity and venous diameter measurements, which are the source measurements used for TRBF calculation. The COV was 16.9 ± 6.9% for the venous flow velocity and 1.6 ± 0.8% for venous diameter, suggesting that the measurement error is mostly credited by the error in velocity measurement.

In en face Doppler OCT, there is no angle involved in the axial flow velocity measurement; the only source of error in the axial flow velocity measurement is Doppler phase noise. If the Doppler phase values from the low-amplitude pixels are effectively rejected, then, the most major source of TRBF measurement error would likely be the blood flow area segmentation. Therefore, it is reasonable to expect considerably higher measurement repeatability, or lower COV, in TRBF measurement using en face Doppler OCT compared to BLDV. Considering these situations, we decided that understanding the measurement repeatability of en face Doppler OCT in various healthy and diseased cohorts and comparing the intra-subject error with the inter-

cohort differences in TRBF is more important than correlating TRBF measurements using en face Doppler OCT and BLDV in each individual for validating en face Doppler OCT.

The COV evaluated in the investigations by our group using the current four-step algorithm was as follows: 1.9% to 8.4% (median 2.9%) in 11 eyes of 8 healthy subjects, 1.8% to 9.6% (median 3.9%) in 8 eyes of 7 diabetic patients without retinopathy, 1.8% to 11.0% (median 7.0%) in 23 eyes with diabetic retinopathy (DR) of 15 patients, and 3.1% to 10.9% (median 6.3%) in 13 eyes with primary open-angle glaucoma (POAG) of 13 patients. The reason for increased median COV in the eyes with DR or POAG can be explained by the nature of segmentation error in en face OCT. Rejecting Doppler phase artifacts such as beam climbing/sliding while detecting slow flow velocities near the endothelium or at diastoles is the utmost objective of TRBF calculation software for en face Doppler OCT. When a segmentation error occurs, it typically results in a certain absolute, not relative, amount of overestimation or underestimation of TRBF because the slow axial velocity regime corresponding to the phase artifacts does not scale with the mean TRBF value. Since the standard error is relatively constant regardless of the mean TRBF, the COV of en face Doppler OCT TRBF measurement tends to heavily depend on the mean TRBF itself. Therefore, the increased median COV in the eyes with DR could have been contributed by the decreased mean TRBF in the eyes with diabetic macular edema (DME) and similarly for the eyes with POAG as well. These results are discussed in further detail in Chapter 3.

2.4.6.2 Choice between Arterial Flow and Venous Flow

The TRBF detection software is designed to detect arterial or venous flow according to the user-specified initial option. The exact same filters and operations are applied except The reason we

select arterial flow rather than venous flow is in two folds: first, the arteries tend to lie above the veins at the optic nerve head; second, the arteries have higher peak blood flow, making it easier to detect them in at least one volume in rapidly repeated volume scans. The Bland-Altman mean-difference plot (Fig. 2.16) of arterial and venous TRBF in eyes with diabetic retinopathy shows that in some eyes, the measurements were similar; in other eyes, arterial flow was considerably higher than venous flow. In 14 eyes, venous flow could not be measured. Shadowing of vessels can prevent imaging the full en face vessel cross-section because veins tend to be posterior to arteries and blood cells are highly scattering and attenuating.

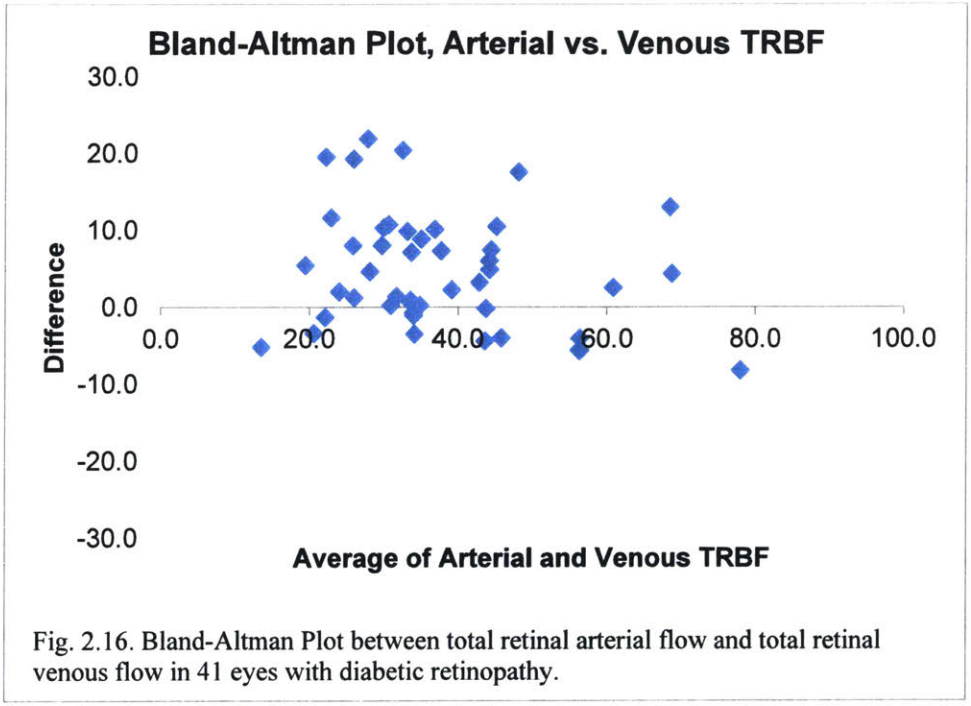

Fig. 2.16. Bland-Altman Plot between total retinal arterial flow and total retinal venous flow in 41 eyes with diabetic retinopathy.

2.4.6.3 Usage of Field Autocorrelation Function

One major disadvantage of median or NaN-median filters is that their computational complexity is roughly proportional to the square root of the kernel area or volume. Although GPU hardware acceleration can increase the filtering speed, it is still significantly slower than the linear space-invariant filters. In particular, Gaussian filters are far more efficient than median filter not only

because it is linear space-invariant but also because 3D Gaussian filtering can be achieved by three separate 1D Gaussian filters applied on each of the three dimensions due to the separable nature of Gaussian in Cartesian coordinates. Moreover, Gaussian filtering is appropriate for any optical imaging using Gaussian beam illumination because the convolution of Gaussian and another Gaussian is also Gaussian. Therefore, from computational and physical perspectives, finding a way to use Gaussian filter would be beneficial to en face Doppler OCT.

Field autocorrelation (FAC) is correlation integral of the optical field (electric field or magnetic vector potential) with itself. FAC is the Fourier-transform dual of the power spectral density, as proven by Wiener-Khinchin-Einstein theorem. Fourier-transform infrared spectroscopy (FTIR) uses FAC to measure the spectrum of lasers at infrared wavelengths. Recall that the mathematical expression for raw and normalized FAC $A(\tau)$ and $a(\tau)$ is

$$\begin{aligned} A(\tau) &= \left\langle S(t)S^*(t-\tau)\right\rangle_t, \\ a(\tau) &= \frac{\left\langle S(t)S^*(t-\tau)\right\rangle_t}{\left\langle \left|S(t)\right|^2\right\rangle_t} \end{aligned} \tag{2.8}$$

where $S(t)$ denotes the backscattered optical field from an ensemble of scattering particles in the sample, and τ denotes the time interval between two different measurements. FAC is used in more advanced phase-sensitive techniques for velocity measurements such as dynamic light scattering OCT [5]. In Doppler OCT context, FAC can be used as a mathematical tool for spatial filtering of Doppler phase. The time offset τ would be fixed at the time interval between two adjacent A-scans. In order to show how FAC is an ideal tool for filtering Doppler phase, we can look at two FD-OCT A-scans of the same scattering particle taken at two different times:

$$\begin{aligned} S(k,t) &= r(k)e^{-j2kz(t)} \\ S^*(k,t-\tau) &= r^*(k)e^{j2kz(t-\tau)} \end{aligned} \tag{2.9}$$

if we assume the spectral reflectivity is the same between the two A-scans, the corresponding FAC would be

$$A(k,\tau) = \left\langle |r(k)|^2 \, e^{-j2k[z(t)-z(t-\tau)]} \right\rangle_t \tag{2.10}$$

For OCT, the time-averaging operator $\langle \cdot \rangle_t$ can be assumed to be equivalent to spatial filtering in subsequent A-scans. In this case, the phase angle of FAC, $\angle A(\tau)$, would be equal to the Doppler phase, and the magnitude of the FAC, $|A(\tau)|$, would be close to the backscattered intensity. Therefore, if FAC is filtered with any linear space-invariant filter, the phase angle of the filtered result is an "intensity-weighted average" of the Doppler phase. This means that using complex FAC data, instead of using two separate real arrays of amplitude and Doppler phase, can simplify the 3D NaN-median filtering of the Doppler phase into 3D Gaussian filtering of an array of FAC. Since 3D Gaussian filter is efficient, the filter can be applied to the whole volume to eliminate the need for applying 1D NaN-median filters and 2D median filters for each depth offset in tilted plane pseudo-flow detection. These are enough reasons to revise the current en face Doppler TRBF processing scheme using FAC and 3D Gaussian filters.

2.5 Pulse Oximetry Cardiac Gating for Lower A-Scan Rates

2.5.1 Motivation

As of 2018, current FDA-approved commercial OCT instruments operate at A-scan rates of 100 kHz or less, which yield low volume rates, limiting the ability to sample the cardiac cycle. Therefore, in order to perform accurate pulsatile TRBF measurements with en face Doppler OCT, data acquisition should be cardiac-gated so that the measurements at different cardiac phases can be distributed across multiple cardiac cycles. Cardiac gating is commonly used in

other imaging modalities such as computed tomography [6] and magnetic resonance imaging [7]. In OCT, pulsatile blood flow measurements using cross-sectional Doppler with pulse oximetry cardiac gating was previously performed in a single choroidal vessel [8]. An en face Doppler OCT approach was also demonstrated which partitioned multiple volumes based on the cardiac phase to reconstruct cardiac-phase-coherent volumes and measure pulsatile blood flow in individual retinal vessels and TRBF [9]. However, this implementation used long imaging sessions with 10 to 20 OCT acquisitions.

This section describes a method for measuring TRBF using pulse-oximetry-gated en face Doppler with SS-OCT at 100 kHz A-scan rate. Pulsatile TRBF was measured using three OCT acquisitions and fully automatic post-processing methods. Cardiac pulse information obtained from the pulse oximetry plethysmogram was used to trigger the OCT acquisition during imaging as well as to accurately integrate the pulsatile TRBF in post-processing. Since commercial SS-OCT instruments operating at 100 kHz A-scan rates are available for investigational use in the US, this technique can be applied in the clinic with a pulse oximeter and relatively simple instrument modifications. If sufficient reproducibility can be achieved, the short measurement time and the ability to automatically process data and obtain quantitative measurements should facilitate larger-scale studies of TRBF.

2.5.2 Prospective Cardiac Gating

In order to measure pulsatile total retinal blood flow, three multiple-volume OCT acquisitions were separately triggered at specific phases in the cardiac cycle. We marked the systolic peaks in the plethysmographic waveform and defined one cardiac cycle as the time period between two

subsequent systoles. The term "cardiac phase" refers to a time-variable between zero and one indicating the relative time position in the current cardiac cycle:

$$\text{(cardiac phase)}=\frac{\text{(time elapsed in the cureent cardiac cycle)}}{\text{(total duration of the current cardiac cycle)}}=\frac{t-t_1}{t_2-t_1} \tag{2.11}$$

where t is the current time, and t_1 and t_2 are two subsequent systolic time points, and $t_1 < t < t_2$. Our prospective cardiac gating algorithm computed a real-time estimate of the subject's cardiac phase because the true value of the cardiac phase is unknown before the next systole. Each OCT acquisition comprised four repeated volumes, each with 600×80 A-scans covering a 1.5 mm×2 mm area of the optic disc, requiring a total of 2.2 seconds acquisition time. Rather than adjusting the volume rate according to the subject's heart rate, the four OCT volumes were acquired at the maximum 1.8 volumes/sec fixed rate in order to minimize the total scan time. Shorter scan times are easier to tolerate for patients and minimize artifacts from blinking or eye motion. However, scanning at fixed volume rate is disadvantageous in that the cardiac cycle may be inadequately sampled depending on the relationship between the OCT scan rate and the heart rate—if the OCT volumes repeatedly sample the same cardiac phase, measurements will be redundant. For example, at a 1.8 volumes/sec scan rate (110 volumes/min), continuous scanning of a subject with a heart rate of 55 beats/min can sample only two cardiac phases separated by one half the cardiac cycle. In order to improve sampling of the entire cardiac cycle for a range of heart rates, we used a cardiac gating algorithm which triggers three repeated multiple-volume OCT acquisitions at three distinct cardiac phases optimized for adequate sampling of the cardiac cycle. If the heart rate was less than 85 beats per minute (bpm), the three acquisitions were triggered at three different cardiac phases separated by 1/6 of the cardiac cycle. However, if the heart rate was greater than 85 bpm, the three acquisitions were triggered at three different cardiac phases

separated by 1/3 of the cardiac cycle. Fig. 2.17 illustrates how the cardiac cycle is sampled for different heart rates.

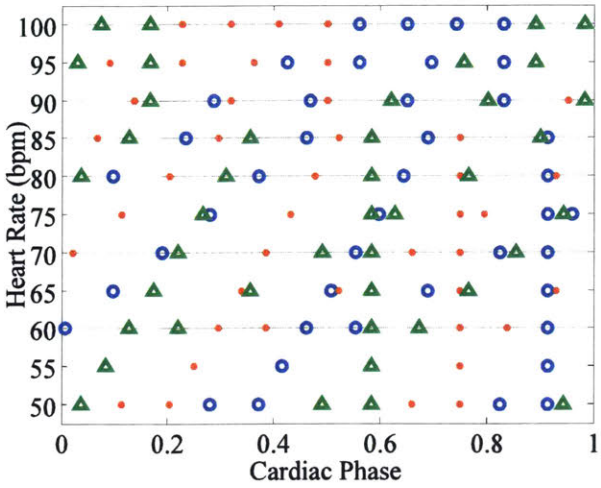

Fig. 2.17. Timing diagram showing how the cardiac cycle is sampled for different constant heart rates. Three repeated OCT acquisitions (shown by different symbols), of four OCT volumes each, are acquired and sample the cardiac cycle as shown by the distribution of symbols on the horizontal lines. Different heart rates are shown by offset horizontal lines. The phase of the OCT acquisitions is chosen to improve sampling. For heart rates <85 bpm, the three acquisitions were triggered at 1/6 multiples of the cardiac cycle, while for heart rates >85 bpm, the three acquisitions were triggered at 1/3 multiples of the cardiac cycle.

Volumetric images of intensity and Doppler phase were generated from the raw OCT data. Each A-scan consisted of 1408 samples, resulting in 704 pixels after Fourier transformation. The pixel spacing was ~4 μm in tissue. The 12 OCT volumes obtained from the three acquisitions were individually processed using the algorithm described in Section 2.4 to measure TRBF.

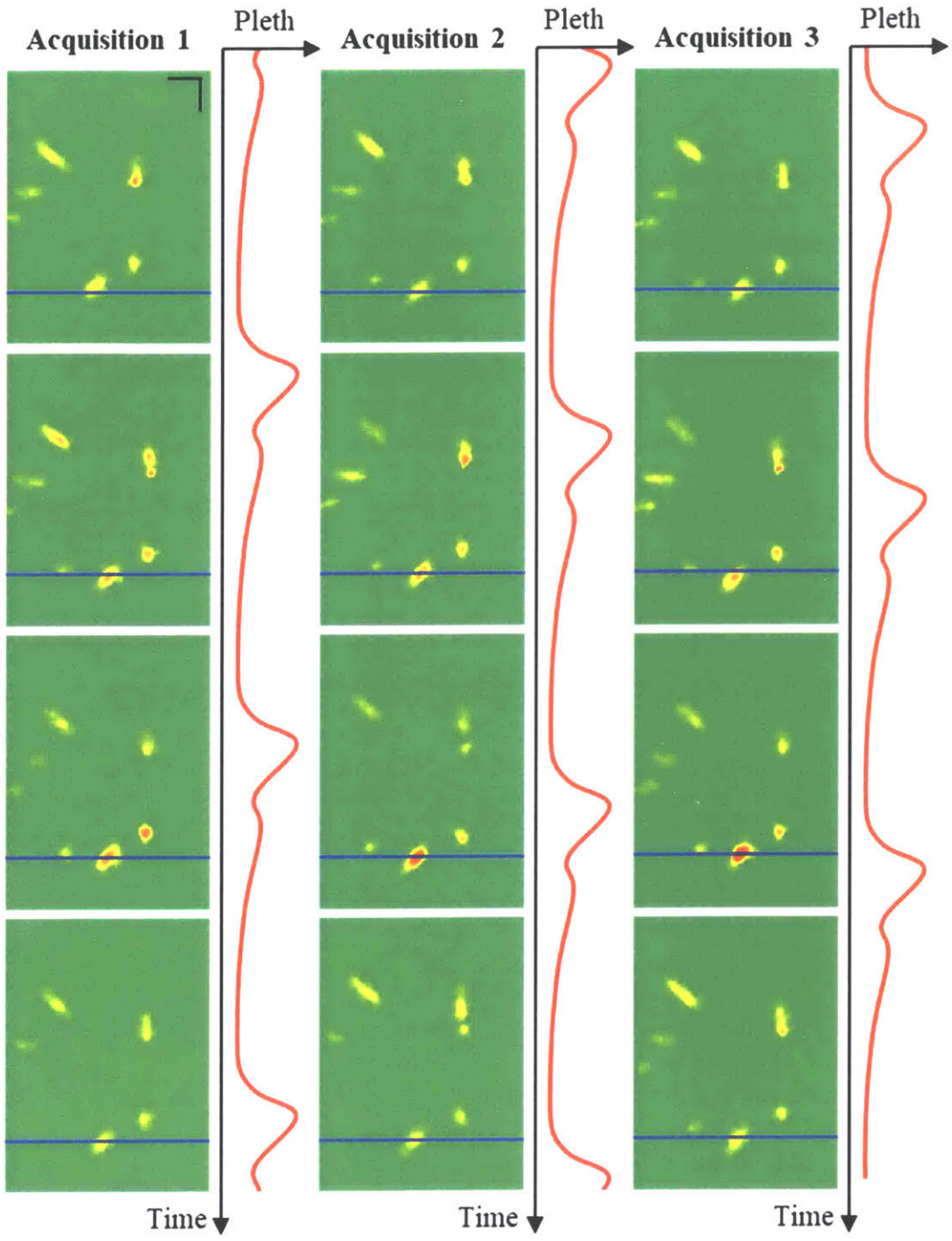

Fig. 2.18. Schematic of the retrospective cardiac gating using weighted averaging of blood flow in each B-line position. Cardiac phase which corresponds to each B-line position in the *en face* Doppler velocity maps is extracted from the plethysmogram simultaneously recorded with OCT. Since the time spacing among the twelve volumes is irregular, the amount of average blood flow in the B-line is calculated by weighted averaging. 1.5 mm by 2 mm.

2.5.3 Retrospective Cardiac Gating

The last key step in our automatic TRBF calculation algorithm is retrospective cardiac gating, where the mean TRBF was calculated by integrating blood flow with respect to the cardiac phase calculated from the recorded plethysmogram. As shown in Fig. 2.17, the cardiac phase intervals between the volumes are non-uniform. Therefore, a simple average of TRBF in the 12 volumes may not accurately measure the mean TRBF because densely sampled portions of the cardiac cycle are overrepresented while sparsely sampled portions are underrepresented. Instead of simple averaging, the plethysmogram recorded with OCT can be used to time-stamp the OCT data, enabling a more accurate integration of flow over the cardiac cycle. Since the raster scan time per volume (0.55 seconds) was itself comparable to a cardiac cycle, individual B-scan lines at all raster positions on the en face Doppler velocity map were labeled with instantaneous cardiac phase. This method guarantees that all blood vessels are labeled with the correct cardiac phases. If each volume is only labeled with a single cardiac phase, perturbations such as saccadic eye motion and small fluctuation in heart rate may introduce cardiac gating errors which affect TRBF measurement.

Fig. 2.18 schematically shows the process of integrating the blood flow in one B-scan position in order to obtain the mean flow. First, the individual B-scan lines in the 12 en face Doppler velocity maps were grouped based on their raster positions in the scan area. At each raster position, the amounts of blood flow intercepted by the 12 B-scan lines were used to generate an approximation of the flow over a cardiac cycle as shown in Fig. 2.18 (B). Then, the mean flow over the cardiac cycle was measured by integrating the flow with respect to cardiac phase using the trapezoidal rule. This technique essentially integrates the linearly interpolated

flow and is well known for its high accuracy when integrating periodic functions [10]. For the B-scan lines at the m^{th} row in the raster scan, the mean blood flow F_m was calculated as

$$F_m = \sum_{n=1}^{12} f_{m,n} \frac{\phi_{m,n+1} - \phi_{m,n-1}}{2} \tag{2.12}$$

where $\phi_{m,0} = \phi_{m,12} - 1$, $\phi_{m,13} = \phi_{m,1} + 1$. In this equation, $f_{m,n}$ represents amounts of blood flow intercepted by the B-scan lines and $\phi_{m,n}$ represents their associated cardiac phases, where n is indexed from the smallest to the largest value of cardiac phase. It is important to mention that the integration of flow requires only the relative cardiac phase and the absolute cardiac phase is not necessary. Lastly, the mean TRBF was calculated by aggregating the mean blood flow in all 80 B-scan positions:

$$\text{(Mean TRBF)} = \sum_{m=1}^{80} F_m = \sum_{m=1}^{80} \sum_{n=1}^{12} f_{m,n} \frac{\phi_{m,n+1} - \phi_{m,n-1}}{2}. \tag{2.13}$$

The resulting mean TRBF gives an accurate measurement because potential causes of measurement errors such as non-uniform sampling of the cardiac cycle, saccadic eye motion, and fluctuation in heart rate are effectively handled by time-stamping individual B-scans.

2.5.4 Repeatability Study

We evaluated pulse-oximetry-gated en face Doppler OCT on 10 healthy young subjects to quantify the impact of cardiac gating on TRBF measurement repeatability. We measured TRBF in all 10 subjects using three different approaches: (1) asynchronous acquisition using 100 kHz SS-OCT, (2) cardiac-gated acquisition using 100 kHz SS-OCT, and (3) asynchronous acquisition using 400 kHz high-speed SS-OCT as a control. When processing asynchronously acquired data, mean TRBF was calculated as the simple average of blood flow in all volumes. Imaging

procedures for asynchronous acquisition and cardiac-gated acquisition with 100 kHz SS-OCT were identical except for the use of pulse oximetry cardiac gating. Asynchronous 400 kHz SS-OCT used the same scan pattern as reference [11], comprising 750×60 A-scans covering 1.5 mm×1.5 mm area. Since the volume scan rate of 7.6 volumes per second improves the sampling of pulsatile blood flow, this method was used as a control to test the accuracy of pulse oximetry cardiac gating. Three measurements were repeated for each method in each subject to calculate mean, standard deviation, and intra-subject coefficient of variation (COV) to assess the measurement repeatability.

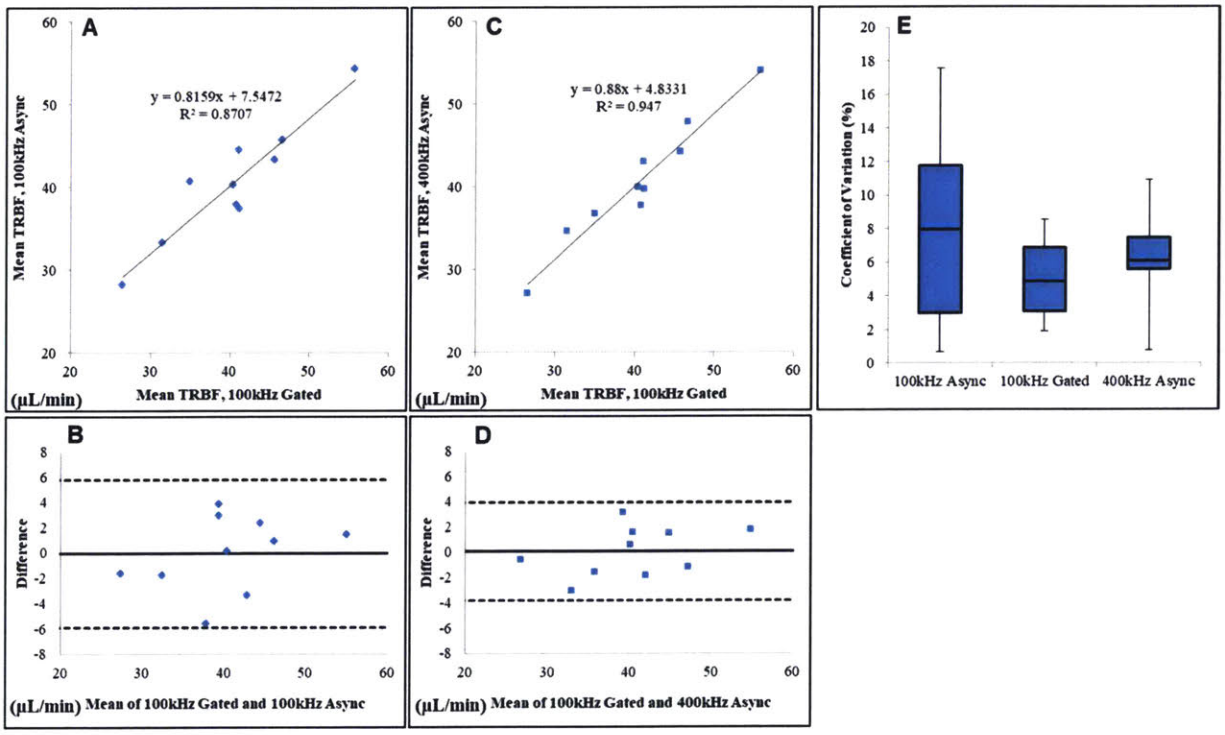

Fig. 2.19. (A-D) Correlation and Bland-Altman plots between the averages of three repeated total retinal blood flow measurements using different methods.
(A) Correlation plot between 100kHz with cardiac gating and 100kHz with asynchronous acquisition.
(B) Bland-Altman plot between 100kHz with cardiac gating and 100kHz with asynchronous acquisition.
(C) Correlation plot between 100kHz with cardiac gating and 400kHz with asynchronous acquisition.
(D) Bland-Altman plot between 100kHz with cardiac gating and 400kHz with asynchronous acquisition.
(E) Box plot comparing the coefficients of variation of the three methods.

Results of this repeatability study show that at 100 kHz A-scan rate, pulse oximetry cardiac gating can reduce measurement variability compared to asynchronous acquisition at similar as well as higher imaging speeds (400 kHz). Fig. 2.19 shows correlation plots and Bland-Altman mean-difference plots between the averages of three repeated measurements from the same subjects using our pulse oximetry cardiac gating approach versus asynchronous acquisition, as well as a box plot comparing COV of the three methods. The correlation plots and Bland-Altman plots confirm that the measurements from the three methods are consistent since there is a high degree of linear correlation without a significant bias. The COV of three measurements in the 10 healthy young subjects was 1.9% to 8.6% (median 4.9%) with cardiac gating and 0.7% to 17.5% (median 8.0%) without cardiac gating. The maximum COV for all three methods was observed in the same subject, who had a high pulsatility index (~0.9) in the central retinal artery. The COV in this subject showed a large improvement, 8.6% with cardiac gating versus 17.5% without cardiac gating, suggesting that pulse oximetry cardiac gating can enable reliable measurements of mean TRBF even in subjects with high flow pulsatility. Encouragingly, the box plot also shows that 100 kHz SS-OCT with cardiac gating can achieve similar or higher repeatability compared to high speed, 400 kHz SS-OCT with asynchronous acquisition. However, please note that this study was performed at earlier time than the development of the four-step algorithm described in Section 2.4, and the 6.1% median COV reported in Fig. 2.19 does not represent the current four-step algorithm.

2.5.5 Discussion

Comparing the measured COV of the cardiac gating method (1.9% to 8.6%, median 4.9%) with previous repeatability studies using conventional techniques suggests that TRBF measurement

using gated en face Doppler OCT is potentially more precise. An early study reported the COV of five TRBF measurements using the Canon Laser Blood Flowmeter in 20 healthy subjects ranging from 4.8% to 37.3% (median 19.3%) [12]. The high COV may have resulted from a combination of daily variation and measurement error, since the five measurements were distributed on five different visits within a month period, because of the long measurement time. In another BLDV study where TRBF in 16 healthy participants was monitored every three hours over a 12-hour time span from 8AM to 8PM, the average COV of TRBF was 18.5% [4]. Although this variation may be a mixture of diurnal fluctuation and measurement error, the lack of clear time dependence in the average TRBF suggested that the primary source of variation was measurement error. A later study using cross-sectional Doppler OCT with double circumpapillary scans demonstrated improvements in repeatability compared with BLDV. Wang et al. reported that the average COV of five TRBF measurements was 10.9% in 20 normal eyes and 14.3% in 28 eyes with diseases such as glaucoma, nonarteritic ischemic optic neuropathy, and proliferative diabetic retinopathy [13]. However, recent work by Rose et al. showed a systematic increase in TRBF measured by the same reader before and after training, suggesting a potential risk of reader-dependent or training-dependent variation of TRBF measured from the same dataset [14]. Our measurements in healthy young subjects demonstrate that cardiac-gated en face Doppler OCT with fully automatic post-processing enables higher measurement repeatability than existing methods.

The B-scan based retrospective cardiac gating method substantially reduces the impact of eye motion on TRBF measurement. Eye motion in the horizontal direction does not affect the flow measurement because it only causes a displacement of the vessel along the B-scan direction. Eye motion in the vertical direction which occurs between successive volumes or within a volume

also does not affect the measurement, provided that the motion does not cause part of a vessel to be missed by B-scans or to be scanned twice. It is important to mention that there are many B-scan positions which do not intercept a vessel and would have zero flow. Vertical eye motion can change the relative position of a vessel in the OCT raster volume and may move the blood flow out of one B-scan position. Then, the flow waveform for a single B-scan position will not reflect the true flow pulsatility but the blood flow will be measured at another B-scan position and will be labeled with the correct cardiac phase. Therefore, the mean TRBF will not change substantially because it is the sum of the integrals of the flow over a cardiac cycle at 80 B-scan positions. Vertical saccades which cause a major vessel to be missed or scanned twice will cause oversampling or undersampling of blood vessels, resulting in an error in TRBF measurement. Therefore, the operator must exclude OCT data with excessive vertical eye motion from the measurement and repeat the acquisition. These data quality criteria a similar to those used for any OCT acquisition.

It is important to note that current commercial SS-OCT instruments are not equipped with A-scan timing jitter compensation and thus the optical phase may not be stable from one A-scan to another. Phase-sensitive OCT imaging methods such as Doppler or phase variance angiography require phase stabilization, which can be achieved by using a fiber Bragg grating in one arm of the balanced photodetector or triggering the A-scan acquisition using a fiber Bragg grating signal. The fiber Bragg grating generates a sharp fiducial edge at a fixed wavenumber in the interference fringes, enabling timing jitter to be compensated and stabilizing the phase across all A-scans. Although this is a simple modification, it requires additional hardware not present in the installed base of existing SS-OCT instruments.

Commercial SD-OCT instruments have stable A-scan phase because they use spectrometers to measure the interference fringes rather than high speed digitizers. However, SD-OCT has several limitations. Commercial SD-OCT instruments operate at ~840 nm center wavelength, shorter than the 1050 nm used in SS-OCT and the highest commercially available SD-OCT imaging speed is currently 70 kHz, slower than the 100 kHz of SS-OCT. These differences result in a smaller phase-wrapping-free Doppler velocity range, which spans only between ±10.9 mm/s. SD-OCT also suffers from signal loss due to fringe washout at high flow velocities because each fringe is integrated over the entire A-scan time [15]. Therefore, en face Doppler imaging of arterial blood flow is difficult with SD-OCT. Although venous flow velocity can be detected more reliably, it is still challenging to calculate TRBF because large veins inside the optic disc margin are frequently located below the arteries. Therefore, en face Doppler OCT measurements of TRBF with currently commercial SD-OCT instruments may be challenging.

Cardiac gating may be valuable for en face Doppler OCT measurements of TRBF using high-speed instruments as well. Automatic blood vessel segmentation in en face Doppler OCT is susceptible to errors caused by timing jitter in the optical clock which determines the digitization of the OCT interference fringe data as well as Doppler phase artifacts from highly reflective layers such as the retinal nerve fiber layer and retinal pigment epithelium. These noise sources and artifacts are often only partially suppressed by post-processing methods and can cause errors in vessel segmentation—misinterpreting a reflection phase artifact as a blood vessel may lead to overestimation of blood flow, while failing to detect a blood vessel with low flow velocity may result in underestimation. The effect of these errors becomes more severe at higher imaging speeds because the same error in Doppler phase corresponds to a larger error in Doppler velocity given the shorter sampling time intervals. Conversely, the risk of errors can be reduced by

increasing sampling time intervals or equivalently, by calculating Doppler phase between non-neighboring A-scans. However, this will decrease the volumetric scan rate because the spatial sampling density must be increased to ensure that the two A-scans being compared still have a large spatial overlap and contain correlated speckle information. This implies there is a tradeoff between volumetric scanning rate and sensitivity to low flow speeds. Therefore, we expect cardiac gating may be helpful for accurate blood flow measurement even at high imaging speeds.

Among the 10 healthy young subjects in this study, the mean and the standard deviation of the TRBFs were 40.5±8.2 μL/min and a wide range of TRBFs, from 26.6 μL/min to 55.8 μL/min, was observed. The large inter-subject variability within healthy subjects is consistent with the results from previous studies using other methods [13, 16]. However, this wide variation among healthy young subjects suggests that it will be difficult to use TRBF alone as an early diagnostic marker since there may be a large overlap between normal and diseased cohorts. However, measurement of changes in TRBF may potentially provide valuable information. Longitudinal measurements of TRBF can be investigated to assess disease progression or treatment response. Measuring changes in TRBF response to visual stimuli [17-20] may enable early assessment of disease in spite of the basal TRBF variation and could potentially enable new diagnostic applications. Reduction of measurement variance is important for all of these studies.

References

[1] B. Baumann, B. Potsaid, M. F. Kraus, J. J. Liu, D. Huang, J. Hornegger, A. E. Cable, J. S. Duker, and J. G. Fujimoto, "Total retinal blood flow measurement with ultrahigh speed swept source/Fourier domain OCT," *Biomed Opt Express,* vol. 2, pp. 1539-52, Jun 1 2011.

[2] W. Choi, B. Baumann, J. J. Liu, A. C. Clermont, E. P. Feener, J. S. Duker, and J. G. Fujimoto, "Measurement of pulsatile total blood flow in the human and rat retina with ultrahigh speed spectral/Fourier domain OCT," *Biomed Opt Express,* vol. 3, pp. 1047-61, May 1 2012.

[3] S. Makita, F. Jaillon, I. Jahan, and Y. Yasuno, "Noise statistics of phase-resolved optical coherence tomography imaging: single-and dual-beam-scan Doppler optical coherence tomography," *Opt Express,* vol. 22, pp. 4830-48, Feb 24 2014.

[4] A. Luksch, M. Lasta, K. Polak, G. Fuchsjager-Mayrl, E. Polska, G. Garhofer, and L. Schmetterer, "Twelve-hour reproducibility of retinal and optic nerve blood flow parameters in healthy individuals," *Acta Ophthalmol,* vol. 87, pp. 875-80, Nov 2009.

[5] J. Lee, W. Wu, J. Y. Jiang, B. Zhu, and D. A. Boas, "Dynamic light scattering optical coherence tomography," *Opt Express,* vol. 20, pp. 22262-77, Sep 24 2012.

[6] B. Desjardins and E. A. Kazerooni, "ECG-gated cardiac CT," *AJR Am J Roentgenol,* vol. 182, pp. 993-1010, Apr 2004.

[7] P. Lanzer, E. H. Botvinick, N. B. Schiller, L. E. Crooks, M. Arakawa, L. Kaufman, P. L. Davis, R. Herfkens, M. J. Lipton, and C. B. Higgins, "Cardiac imaging using gated magnetic resonance," *Radiology,* vol. 150, pp. 121-7, Jan 1984.

[8] M. Miura, S. Makita, T. Iwasaki, and Y. Yasuno, "An approach to measure blood flow in single choroidal vessel using Doppler optical coherence tomography," *Invest Ophthalmol Vis Sci,* vol. 53, pp. 7137-41, Oct 2012.

[9] T. Schmoll and R. A. Leitgeb, "Heart-beat-phase-coherent Doppler optical coherence tomography for measuring pulsatile ocular blood flow," *J Biophotonics,* vol. 6, pp. 275-82, Mar 2013.

[10] Q. I. Rahman and G. Schmeisser, "Characterization of the Speed of Convergence of the Trapezoidal Rule," *Numerische Mathematik,* vol. 57, pp. 123-138, 1990.

[11] W. Choi, B. Potsaid, V. Jayaraman, B. Baumann, I. Grulkowski, J. J. Liu, C. D. Lu, A. E. Cable, D. Huang, J. S. Duker, and J. G. Fujimoto, "Phase-sensitive swept-source optical coherence tomography imaging of the human retina with a vertical cavity surface-emitting laser light source," *Opt Lett,* vol. 38, pp. 338-40, Feb 1 2013.

[12] K. Guan, C. Hudson, and J. G. Flanagan, "Variability and repeatability of retinal blood flow measurements using the Canon Laser Blood Flowmeter," *Microvasc Res,* vol. 65, pp. 145-51, May 2003.

[13] Y. Wang, A. A. Fawzi, R. Varma, A. A. Sadun, X. Zhang, O. Tan, J. A. Izatt, and D. Huang, "Pilot study of optical coherence tomography measurement of retinal blood flow in retinal and optic nerve diseases," *Invest Ophthalmol Vis Sci,* vol. 52, pp. 840-5, Feb 2011.

[14] K. Rose, M. Jong, F. Yusof, F. Tayyari, O. Tan, D. Huang, S. R. Sadda, J. G. Flanagan, and C. Hudson, "Grader learning effect and reproducibility of Doppler Spectral-Domain Optical Coherence Tomography derived retinal blood flow measurements," *Acta Ophthalmol,* Jul 6 2014.

[15] H. C. Hendargo, R. P. McNabb, A. H. Dhalla, N. Shepherd, and J. A. Izatt, "Doppler velocity detection limitations in spectrometer-based versus swept-source optical coherence tomography," *Biomed Opt Express,* vol. 2, pp. 2175-88, Aug 1 2011.

[16] G. Garhofer, R. Werkmeister, N. Dragostinoff, and L. Schmetterer, "Retinal blood flow in healthy young subjects," *Invest Ophthalmol Vis Sci,* vol. 53, pp. 698-703, Feb 2012.

[17] C. E. Riva, B. Falsini, and E. Logean, "Flicker-evoked responses of human optic nerve head blood flow: luminance versus chromatic modulation," *Invest Ophthalmol Vis Sci,* vol. 42, pp. 756-62, Mar 2001.

[18] C. E. Riva, T. Salgarello, E. Logean, A. Colotto, E. M. Galan, and B. Falsini, "Flicker-evoked response measured at the optic disc rim is reduced in ocular hypertension and early glaucoma," *Invest Ophthalmol Vis Sci,* vol. 45, pp. 3662-8, Oct 2004.

[19] G. Garhofer, C. Zawinka, H. Resch, P. Kothy, L. Schmetterer, and G. T. Dorner, "Reduced response of retinal vessel diameters to flicker stimulation in patients with diabetes," *Br J Ophthalmol,* vol. 88, pp. 887-91, Jul 2004.

[20] T. T. Nguyen, R. Kawasaki, A. J. Kreis, J. J. Wang, J. Shaw, W. Vilser, and T. Y. Wong, "Correlation of light-flicker-induced retinal vasodilation and retinal vascular caliber measurements in diabetes," *Invest Ophthalmol Vis Sci,* vol. 50, pp. 5609-13, Dec 2009.

Chapter 3
En Face Doppler OCT Measurement of Total Retinal Blood Flow in Ocular Disease

3.1 Overview

This chapter presents two pilot studies of total retinal blood flow in ocular diseases using en face Doppler OCT. The studies described in the following sections have two main objectives. The first major objective is to validate en face Doppler OCT measurement of total retinal blood flow (TRBF) in eyes with disease and evaluate intra-subject measurement repeatability. Retinal blood flow plays an important pathophysiological role in glaucoma and diabetic retinopathy, both of which are leading causes of blindness. However, the lack of simple and repeatable measurement techniques have complicated systematic investigation of TRBF in these diseases. Therefore, validating en face Doppler OCT as a new standard for TRBF measurement would benefit future investigations of retinal blood flow.

The second major objective is to investigate TRBF in diseased eyes as well as in healthy eyes and correlating TRBF with routine clinical diagnostics such as color fundus photo grading, intraocular pressure, visual fields, and OCT using commercial instruments. Comparative study with conventional measurements will also yield insights in new pathophysiological hypotheses. These two objectives are not completely independent of each other, because the requirements for TRBF measurement repeatability will depend on the differences in TRBF across the diseased and healthy cohorts. The following two sections report example investigations of TRBF in primary open-angle glaucoma and diabetic retinopathy.

3.2 Glaucoma

3.2.1 Motivation

Glaucoma is a leading cause of blindness globally both in the developed world and the developing world [1], potentially affecting 79.6 million people by 2020 [2]. The pathogenesis of glaucoma is not clearly understood, although mechanical and structural risk factors such as elevated intraocular pressure (IOP) and increased optic disc cupping have been identified. In current clinical standard, a decrease in the peripapillary retinal nerve fiber layer (RNFL) thickness measured by optical coherence tomography (OCT) [3] is considered as an early structural marker of glaucomatous progression [4, 5]. There have been an increasing number of publications suggesting blood flow changes are related to the pathogenesis of glaucoma [6-11]. Multiple studies using scanning laser Doppler flowmetry (Heidelberg Retina Flowmeter, Heidelberg Engineering, Heidelberg, Germany) reported that peripapillary retinal blood flow and optic disc blood flow was decreased in glaucoma [12-14].

A recent OCT angiography (OCTA) study [15] focused on the hypothesis that focal ischemia at the optic disc can be a risk factor for glaucoma and demonstrated that the OCTA-based optic disc flow index can discriminate glaucomatous eyes from normal eyes with 100% sensitivity and specificity. The flow index was also strongly correlated with visual fields (VF) pattern standard deviation (PSD). Optic disc flow index represents blood inflow from two main feeding sources, namely central retinal artery (CRA), which provides retinal blood flow and posterior ciliary arteries (PCA), which perfuse the optic nerve head and the choroid. Since it is believed that the retinal circulation and the ciliary circulation do not share the same regulatory system [16-18], a study which isolates blood flow in the CRA from the blood flow in the PCA could merit the understanding of the pathogenesis of glaucoma.

This section reports an investigation on retinal circulation in eyes with primary open-angle glaucoma (POAG) with en face Doppler OCT and to define the relationship between TRBF and traditional measures of structural and functional changes in glaucoma.

3.2.2 Methods

Characteristics	Healthy	POAG	P-Value*
Patients, *n*	10	13	
Eyes, *n*	10	13	
Age (years)	62.1 ± 9.1	73.5 ± 7.8	0.014
Intraocular pressure (mmHg)	14 ± 3	15 ± 4	0.510
Systolic blood pressure (mmHg)	122 ± 20	128 ± 11	0.367
Diastolic blood pressure (mmHg)	78 ± 12	72± 8	0.110
Mean ocular perfusion pressure (mmHg)	53 ± 8	50 ± 3	0.264
RNFL mean thickness (μm)		71 ± 10	
VF mean deviation (dB)		-6.1 ± 4.2	
VF pattern standard deviation (dB)		6.7 ± 4.5	
Glaucoma staging subgroups†			
Stage 0		1	
Stage b		1	
Stage 1		2	
Stage 2		3	
Stage 3		2	
Stage 4		4	
Total retinal blood flow (μL/min)	45.2 ± 8.1	34.8 ± 6.5	0.006

*Calculated by Wilcoxon rank-sum test.

†Staged according to the enhanced glaucoma staging system (GSS 2).

Table 3.1. Characteristics of Healthy Subjects and Patients with Primary Open-Angle Glaucoma

3.2.2.1 Study Population

Patients with POAG and healthy subjects were examined at the New England Eye Center at Tufts Medical Center and the anonymized Doppler OCT images were analyzed at the

Massachusetts Institute of Technology. The research protocol was determined in accordance with the tenets of the declaration of Helsinki and approved by the international review board at Tufts University and the Committee on the Use of Humans as Experimental Subjects at the Massachusetts Institute of Technology. Written informed consent was obtained from each subject after verbal explanation of the study.

One eye from each of 10 healthy subjects (7 females, age 62.1 ± 9.1 years) and 13 patients with POAG (5 females, age 73.5 ± 7.8 years) were analyzed. Among the 13 glaucomatous eyes, 11 were perimetric, as they exhibited significant VF loss defined by the enhanced glaucoma staging system (GSS 2) [19] and optic disc changes such as increased cupping and RNFL thinning on OCT as well as disc rim defects on ophthalmoscopy. The other two glaucomatous eyes were preperimetric, retaining normal or borderline VF test results while manifesting glaucoma-like structural changes at the optic disc.

3.2.2.2 Data Acquisition and Processing

En face Doppler OCT was performed using the 1050-nm wavelength SS-OCT prototype instrument operating at 400 kHz axial scan rate by repeatedly scanning a 600 × 80-A-scan volume covering a 1.5 × 2-mm area at the optic disc. The B-scans were laterally oversampled in order to maintain a high correlation between the neighboring A-scans, so that valid Doppler phase images can be generated. 24 volumes were acquired per measurement at a rate of 7.1 volumes per second, resulting in a total acquisition time of 3.4 seconds. The image acquisition was repeated three times to assess the repeatability of mean TRBF measurement. The acquired data was analyzed by the four-step TRBF calculation algorithm described in Section 2.4.

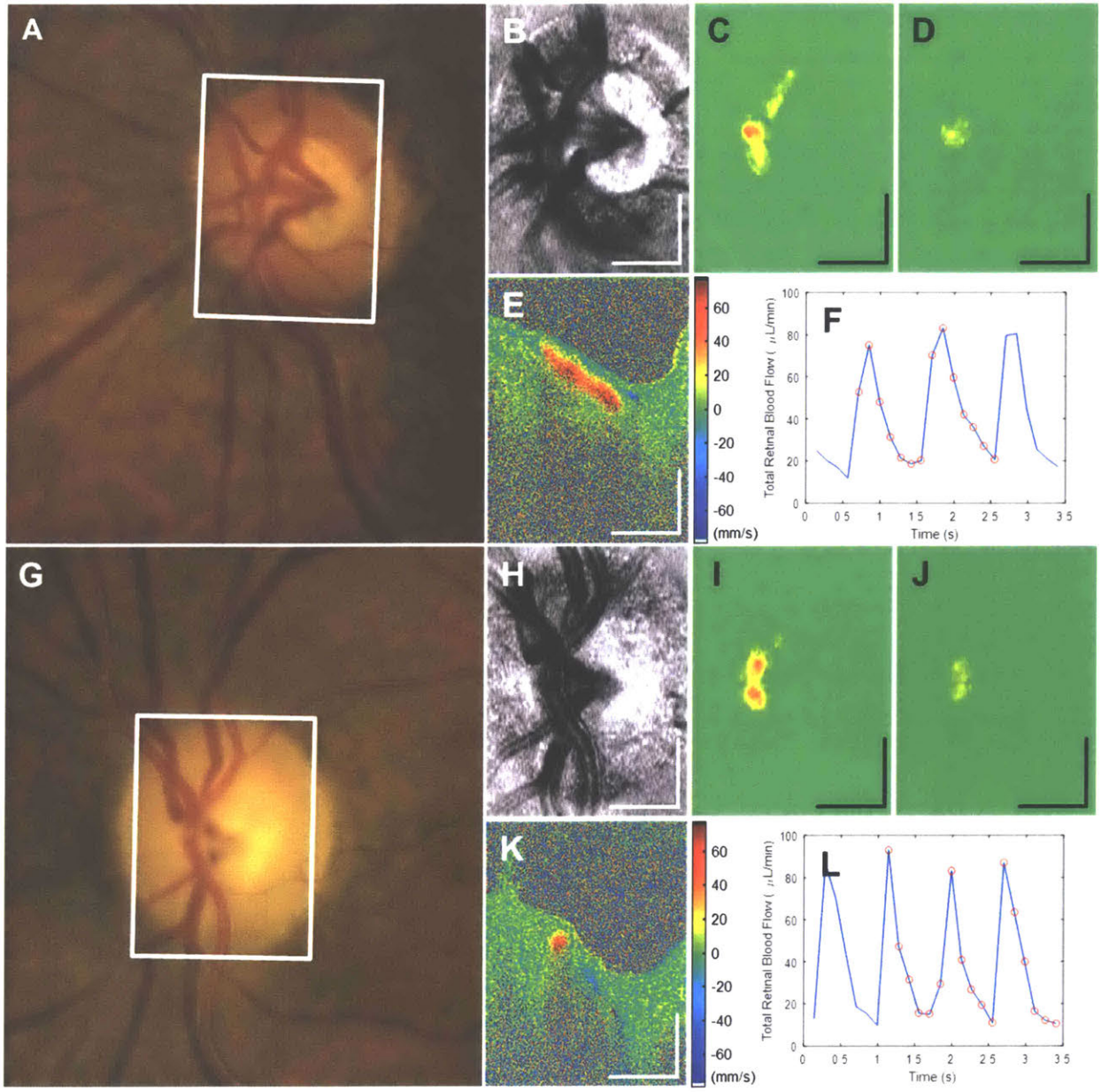

Fig. 3.1. Overview of en face Doppler OCT measurement of TRBF in eyes with preperimetric POAG (A-F) and perimetric POAG (G-L). (A, G) 1.5mm × 2mm OCT scan area marked on fundus photographs. (B, H) En face intensity projection. (C, D, I, J) En face Doppler velocity image at a systole (C, I) and a diastole (D, J). (E, K) A representative cross-sectional Doppler velocity image. (F, L) Pulsatile TRBF waveform drawn in blue and the data points used for mean TRBF calculation marked by red circles. Mean TRBF was 41.1 μL/min in the eye with preperimetric POAG and 35.0 μL/min in the eye with perimetric POAG.

3.2.2.3 SD-OCT Measurement of Peripapillary RNFL Thickness

All patients with POAG were imaged with commercial SD-OCT (Cirrus HD-OCT, Carl Zeiss Meditec, Dublin, CA) for the measurement of the peripapillary RNFL thickness. RNFL thickness was calculated in a volumetric image covering 6 × 6-mm area centered at the optic disc and extracted along the 3.4-mm diameter circle around the optic disc, in order to assess glaucomatous structural changes in the RNFL.

3.2.2.4 Visual Fields Testing

All patients with POAG underwent visual field tests to determine the mean deviation (MD) and pattern standard deviation (PSD) with the Humphrey Field Analyzer II (Carl Zeiss Meditec, Dublin, CA) set for the 24-2 threshold test using the size III white stimulus and the Swedish Interactive Threshold Algorithm.

3.2.2.5 Statistical Analysis

Wilcoxon rank-sum test was used to examine if there was a significant difference in the average values of the measurements such as blood pressure, intraocular pressure, ocular perfusion pressure, and mean TRBF between the eyes with POAG and the healthy eyes. Linear regression analysis was used to determine the relationships between TRBF and traditional measurements such as peripapillary RNFL thickness, VF MD, and VF PSD.

3.2.3 Results

There was no significant difference in IOP, blood pressure, and mean ocular perfusion pressure between the healthy subjects and the patients with POAG. The POAG group had a wide range of

disease severity, ranging from stage 0 to stage 4 according to GSS 2. Mean TRBF was 45.2 ± 8.1 μL/min in the healthy eyes and 34.8 ± 6.5 μL/min in the eyes with POAG, and the difference was statistically significant ($P \leq 0.01$). However, a considerable overlap of the mean TRBF ranges was observed as illustrated in Fig. 3.2 (A), mainly due to the large variation within the healthy group and the two eyes with preperimetric POAG which manifested normal TRBF. Excluding the preperimetric eyes, mean TRBF in the perimetric POAG group was 32.9 ± 5.0 μL/min and the difference in between the healthy group was highly significant ($P \leq 0.005$). The receiver operating characteristic of mean TRBF as a diagnostic test for POAG is shown in Fig. 3.2 (B) and the area under the curve was 0.846. Using a cutoff value of 38.6 μL/min, 77% sensitivity and 80% specificity could be attained. In 7 healthy eyes and 9 eyes with POAG, TRBF could be extracted from all three repeated measurements, and the repeatability was 2.9% and 6.3% median COV, respectively. This corresponded to ~2 μL/min intra-subject standard deviation, both in healthy eyes and in eyes with POAG; the estimated intra-subject variability was considerably smaller than the mean difference between the two groups. In the other eyes, one or two measurements were invalid due to low signal, severe eye motion, or other imaging artifacts.

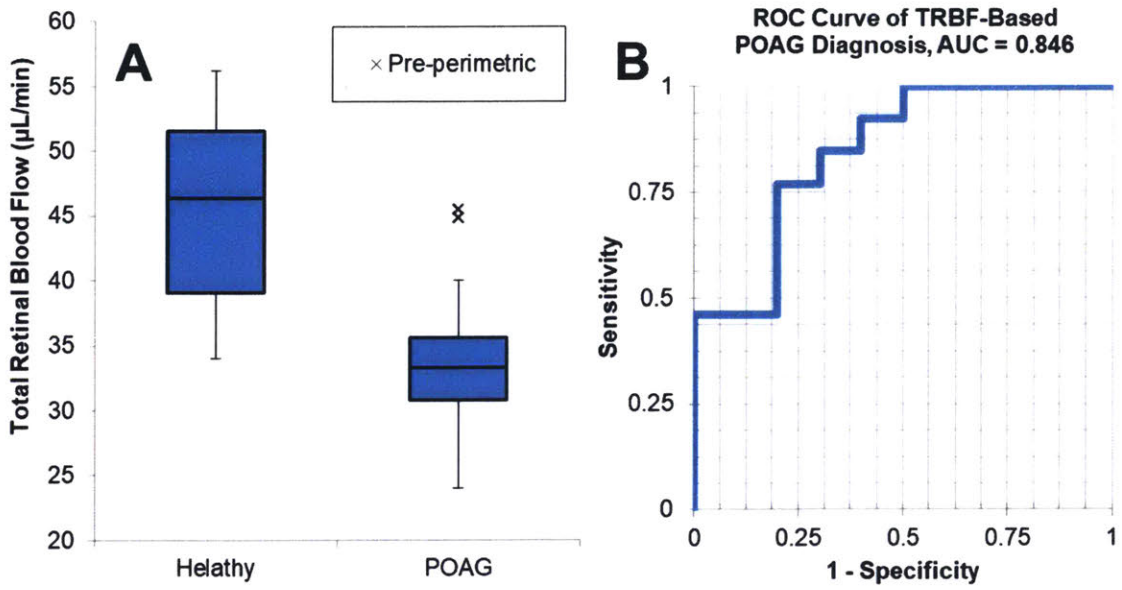

Fig. 3.2. (A) Box plot showing the maximum, minimum, and the quartile values of mean TRBF in the healthy eyes and the eyes with POAG. Pre-perimetric cases are marked as outlying points. (B) Receiver operating characteristic of hypothetical TRBF-based POAG diagnosis. AUC: area under the curve.

In the linear regression analysis within the eyes with POAG, mean TRBF was strongly correlated with VF MD ($R = 0.843$, $P \leq 0.0005$) and PSD ($R = -0.826$, $P \leq 0.001$), and did not show a significant correlation with age ($P > 0.5$). Scatter plot shown in Fig. 3.3 displays that the two preperimetric eyes with least amount of visual field damage also exhibited highest mean TRBF and the thickest RNFL. When excluding the two preperimetric eyes, RNFL was clustered around 67 ± 5 µm with a maximum of 77 µm. The correlation coefficient matrix displayed in Table 3.2 shows that RNFL did not show a significant correlation with any of TRBF, VF MD, and VF PSD in perimetric POAG patients.

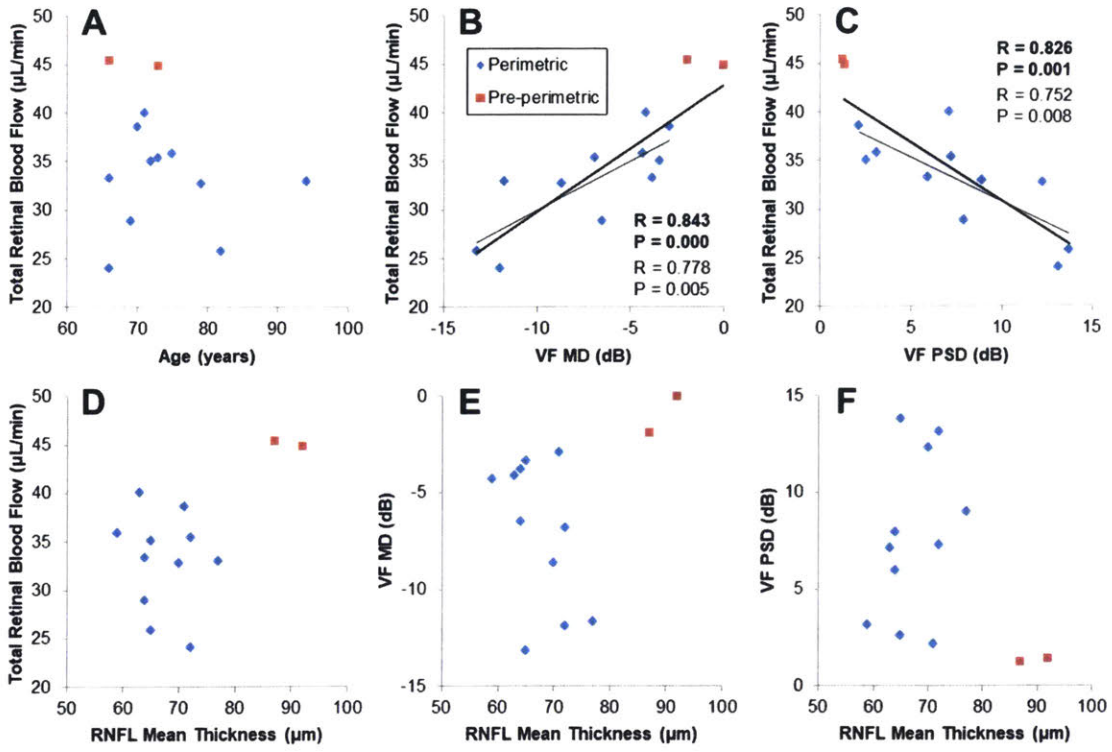

Fig. 3.3. Scatter plots showing the result of linear regression analysis within the eyes with POAG. Thick lines and R and P-values written in bold correspond to regressions for all eyes with POAG, while thin lines and R and P-values written in regular font correspond to regressions for perimetric POAG only. Regression lines represent statistically significant correlations.

R (P-Value)	TRBF	VF MD	VF PSD
VF MD	0.843 (0.000) 0.778 (0.005)		
VF PSD	-0.826 (0.001) -0.752 (0.008)	-0.915 (0.000) -0.887 (0.000)	
RNFL Mean Thickness	0.554 (0.049) -0.154 (0.651)	0.278 (0.358) -0.493 (0.123)	-0.319 (0.290) 0.325 (0.329)

Table 3.2. Correlation matrix among TRBF, visual fields, and RNFL mean thickness. In each cell, the values on the top row were calculated including all POAG and the values on the bottom row were calculated in perimetric POAG only.

3.2.4 Discussion

The key findings of the present study are twofold. First, our en face Doppler OCT measurements confirm the previous reports which suggested retinal blood flow is decreased in glaucoma [12-14, 20] and strongly correlated with visual fields damage [20]. Second, the relationships among TRBF, VF, and RNFL can be understood in accordance with the 'broken stick' model proposed by our collaborators [5]. This model was introduced in a 2010 study, where Wollstein et al. investigated 72 healthy and 40 glaucoma subjects to find that the nonlinear relationship between RNFL and VF MD can be interpreted as a piecewise linear function with two line segments meeting at 75.3 μm and subjects with RNFL thinner than 75.3 μm exhibited wide ranges of VF MD. Their results suggested that a large portion of the RNFL thinning occurs at preperimetric stage, earlier than the alterations in visual function. Although the present study population did not have enough number of preperimetric glaucoma patients to apply segmented regression, the scatter plots in Fig. 3.3 (D-F) clearly shows that there is a separation between perimetric and preperimetric groups. Perimetric POAG exhibited a large variance in TRBF, VF MD, and VF PSD but a small variance in RNFL thickness, while the two preperimetric POAG patients both had normal to boundary values of RNFL thickness, VF MD, and VF PSD as well as normal TRBF. Given the strong correlation between TRBF and VF damage and their relations with RNFL described in Fig. 3.3 (D-F), we can postulate that TRBF may as well have a "broken stick" type relationship with RNFL thickness. This hypothesis must be tested in following studies because in case it is true, it implies RNFL thinning occurs earlier than TRBF decrease in glaucomatous progression. Since determining the causal relationship between tissue mass decrease and blood flow decrease is important in studying the pathogenesis of glaucoma, further investigation will be merited.

It is important to clarify that the results of the present study does not conflict with the findings of Jia et al.'s OCTA study, where normal eyes and glaucomatous eyes were separated by the optic disc flow index without an overlap [15]. The optic disc flow index was defined as the arithmetic mean of the OCTA decorrelation values inside a manually segmented optic disc area. This included the saturated pixels inside the large retinal vessels as well as the unsaturated pixels inside the capillaries in the lamina cribrosa. Since OCTA cannot detect flow velocity changes beyond saturation, a major portion of optic disc flow index decrease in glaucoma is likely to be caused by the hypoperfusion of lamina cribrosa capillaries in the ciliary circulatory system. The present study exclusively measured blood flow through the retinal circulation, which is likely to be regulated separately from the ciliary circulation as stated in the introduction. Therefore, the difference in between the results of the OCTA study and the current en face Doppler OCT study should be understood as the difference in the targeted blood vessels.

There were two main limitations associated with en face Doppler OCT because of its optical nature. First, detection of small flow velocity was challenging due to phase artifacts caused by specular reflection. One of the key assumptions of Doppler OCT is that the speckles are separated well enough so that the sampling positions of the two neighboring A-scans can be treated as identical. If so, an optical signal with a high correlation in between the two neighboring A-scans must be from the same particle, and therefore any nonzero Doppler phase should be associated with particle motion. However, when there are specular reflections from continuous surfaces of retinal nerve fibers and hyperreflective layers such as inner segment/outer segment junction and retinal pigment epithelium (RPE), a nonzero Doppler phase can be measured even without any motion if the surface or the layer has nonzero topographic gradient. In order to remove the specular reflection phase artifact, the Doppler phase threshold used for

retinal artery detection must be set at an appropriately high value. Consequently, there is a tradeoff between robustness against specular reflection phase artifacts and detectability of vessels with low flow velocity. Second, blood vessels located deep in the tissue were not detectable due to scattering and attenuation. We could not test if the implication that RNFL thinning in early glaucoma may be associated with ciliary blood flow decrease is true because PCA is located outside of the sclera. Moreover, the heavy scattering at the RPE decorrelates the signal detected outside of the RPE, disabling phase-sensitive measurements outside of the retina. Quantitative OCTA methods measuring optic disc blood flow without including the large retinal vessels could complement the limitations of Doppler OCT in investigating the relationship among retinal circulation, ciliary circulation, optic nerve atrophy, and visual function in glaucoma.

Other limitations of the study include its observational and cross-sectional nature. As our recruitment was not guided by *a priori* information from a pilot study, the number of preperimetric glaucoma patients was insufficient to apply the 'broken stick' regression. The current study population only included two preperimetric POAG patients, both with healthy to borderline RNFL. In order to apply segmented regression and find the 'tipping point' RNFL thickness between the two line segments, additional preperimetric POAG patients with various RNFL thicknesses would be required.

In conclusion, we used high-speed en face Doppler OCT to investigate retinal blood flow in eyes with POAG and healthy eyes. Mean TRBF was lower in the POAG group compared to the healthy group, although a considerable overlap between the two groups were observed. Within the POAG group, both VF MD and PSD were strongly correlated with TRBF. Two patients with preperimetric glaucoma exhibited TRBF close to its average in the healthy group. The scatter

plot between RNFL thickness and TRBF implies that TRBF might also have 'broken-stick' type of a relationship with RNFL, similar to the nonlinear relationship between VF MD and RNFL supported by our collaborators' studies.

3.3 Diabetic Retinopathy

3.3.1 Motivation

Diabetic retinopathy (DR) is the leading cause of legal blindness among working age adults in developed countries [21-23]. Because of their important role in the development of DR, alterations of the retinal microvasculature in DR eyes have been extensively studied *in vivo* using fluorescein angiography (FA) and indocyanine green angiography (ICGA) techniques and, more recently, OCTA. These investigations have detailed a variety of microvascular alterations, including microaneurysms, capillary drop-out and remodeling; interestingly, recent studies have also found these alterations to be present in some diabetic eyes without clinically apparent retinopathy [24-26]. Despite the successes of FA/ICGA and OCTA studies in identifying important diagnostic markers for DR, the underlying mechanisms of DR pathogenesis and progression are still incompletely understood.

The importance of retinal blood flow in DR has also motivated investigations of TRBF in diabetic eyes. Researchers have used a variety of techniques to measure RBF changes in DR, including video FA [27, 28], laser Doppler velocimetry (LDV) [29-34], and ultrasound color Doppler imaging [35]. Results from these studies provided a mixed picture of RBF in diabetics. In particular, while a majority of the studies noted increased flow in nonproliferative diabetic retinopathy (NPDR) [27-32], a few noted decreased flow [33, 34, 36]. Results from studies in eyes with proliferative diabetic retinopathy (PDR) were similarly mixed [28, 33, 35, 36]. When

interpreting these conflicting results, it is important to understand the limitations of the techniques: video FA cannot measure blood flow velocity but detects the arteriovenous passage time; LDV measures maximum blood flow velocity in one vessel at a time, and requires fundus-photography-assisted vessel caliber measurements to determine TRBF; and ultrasound color Doppler imaging can detect flow velocity in the ophthalmic artery, but lacks the spatial resolution necessary to measure TRBF. Because of these limitations, the term 'retinal blood flow' is often used nonspecifically, describing alternate quantities, such as average flow velocity or arteriovenous passage time, which, while being surrogates, are not measures of true TRBF. For these reasons, more reliable and precise TRBF measurement techniques would likely be useful for investigating TRBF changes in DR.

3.3.2 Methods

The study was a comparative analysis of TRBF in eyes from diabetic patients and age-matched healthy controls. The study was conducted at the New England Eye Center at Tufts Medical Center (Boston, MA), and was approved by the Institutional Review Boards at Tufts Medical Center and the Committee on the Use of Humans as Experimental Subjects at the Massachusetts Institute of Technology (Cambridge, MA). The research adhered to the tenets of the Declaration of Helsinki and complied with the Health Insurance Portability and Accountability Act of 1996. Written informed consent was obtained before image acquisition. The collected OCT data were analyzed at the Massachusetts Institute of Technology.

A	Mild NPDR	Moderate NPDR	Severe NPDR/PDR	
No DME	9	7	7	**23**
DME	1	12	5	**18**
	10	**19**	**12**	**41**

B	Laser-Treatment-Naïve	Focal Laser	Laser PRP	
Anti-VEGF-Treatment-Naïve	7	4	0	**11**
Anti-VEGF-Treated	2	3	1	**6**
	9	**7**	**1**	**17**

Table 3.3. DR patient stratification and DME treatment history. (A) Sizes of the groups stratified by retinopathy severity and presence of DME. (B) Treatment history profile of the 17 patients with moderate or severe retinopathy and present DME. PRP: pan-retinal photocoagulation. VEGF: vascular endothelial growth factor.

3.3.2.1 Study Population

Diabetic patients with and without DR as well as healthy controls in this study were seen at the retina service of the New England Eye Center between May 23, 2014 and January 11, 2016 and were prospectively recruited to be imaged with the OCT prototype system. Blood pressure was measured during the OCT imaging session; intraocular pressure and axial eye length were recorded at the same visit. Ocular perfusion pressure was calculated as the difference between mean blood pressure and intraocular pressure.

The inclusion criteria for the DR group were diabetic patients presenting vascular changes consistent with DR, with or without diabetic macular edema (DME), as diagnosed by a retina specialist based on a complete clinical examination, including a direct fundus examination and color fundus photos. The presence and severity of DR were assessed using the Early Treatment of Diabetic Retinopathy Study (ETDRS) [37], as i) mild NPDR (presence of microaneurysms in the retina); ii) moderate NPDR (more than mild but less than severe NPDR; iii) severe NPDR (>20 intraretinal hemorrhages in each of the four quadrants, venous beading in at least two

quadrants, and intraretinal microvascular abnormalities (IRMA) in at least one quadrant in the absence of PDR); and iv) PDR (optic disc or retinal neovascularization). Exclusion criteria for the DR group were the presence of any concurrent ocular or systemic disease that would act as a confounding factor (age-related macular degeneration, hypertensive retinopathy, glaucoma, retinal vein or artery occlusion, refractive error more than 6 diopters or uveitis) and media opacity. Healthy controls were excluded if any ocular or systemic disease that potentially affects the vasculature was present.

Eyes of diabetics were classified as either with DR or without DR. Eyes with DR were stratified into two groups according to the presence or absence of DME. Each of these two groups was then further stratified into three groups according to disease severity: mild NPDR, moderate NPDR, and severe NPDR/PDR (Table 3.3).

3.3.2.2 Data Acquisition

En face Doppler OCT was performed using the 1050-nm SS-OCT prototype system operating at 400 kHz A-scan rate by repeatedly acquiring 600×80 A-scan volumes, each covering a 1.5 mm×2 mm area at the optic disc. The B-scans were laterally oversampled to maintain a high correlation between the neighboring A-scans to ensure the quality of Doppler images. For each TRBF measurement, 24 volumes were acquired at a rate of 7.1 volumes per second, requiring a total acquisition time of 3.4 seconds. The image acquisition sequence was repeated four times to assess the repeatability of the mean TRBF measurement, although one measurement was randomly chosen for data analysis because some of the repeated measurements were invalid due to low signal or excessive eye motion in some subjects. The data was analyzed by the four-step algorithm described in Section 2.4 to obtain the mean TRBF.

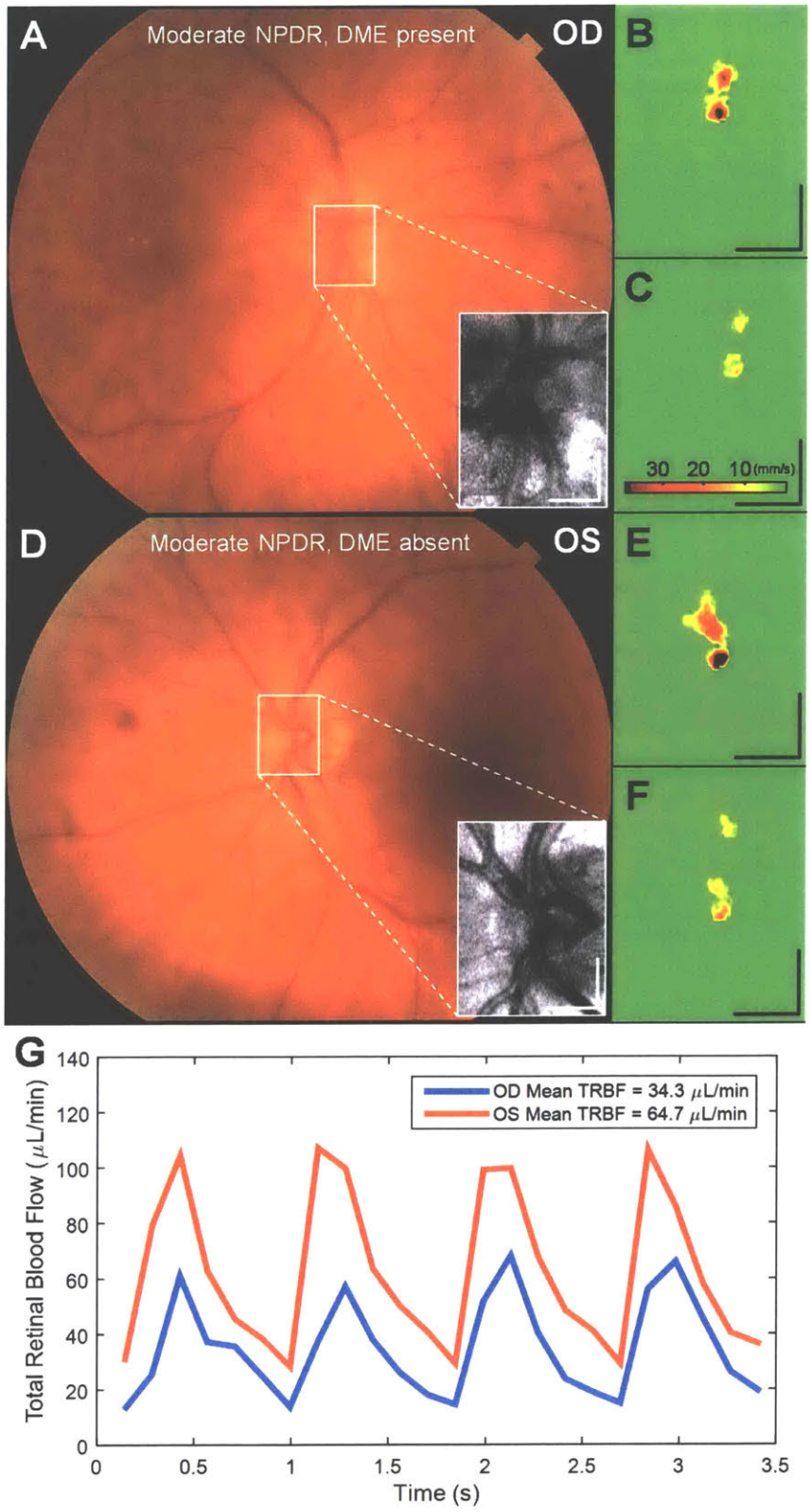

Fig. 3.4. TRBF measurement in a patient with unilateral DME. (A, D) *En face* Doppler OCT scan area marked on color fundus photographs. (B, C, E, F) Axial flow velocity *en face* profiles at systole and diastole. (G) Pulsatile TRBF in the two eyes. Scale bars 500μm.

3.3.2.3 Statistical Analysis

A linear mixed effects model was used to test the significance of TRBF difference between two groups, in order to separately consider the variation among different subjects and the variation between two eyes of the same subject. For comparison of other measurements such as blood pressure, intraocular pressure, and ocular perfusion pressure between two groups, the Mann-Whitney *U*-test was used for simplicity.

Characteristics	Control	DM no DR	DR
Patients, *n*	12	11	31
Eyes, *n*	16	20	41
Age (years)	58.8±10.1	57.9±8.1	62.8±13.4
Systolic blood pressure (mmHg)	115±17	125±7	121±16
Diastolic blood pressure (mmHg)	72±7	81±6	70±13
Mean blood pressure (mmHg)	87±10	95±8	87±13
Intraocular pressure (mmHg)	13.0±2.2	15.8±2.4	14.9±2.5
Mean ocular perfusion pressure (mmHg)	74±9	79±6	73±12
Axial Eye Length (mm)	23.5±1.1	24.1±1.4	24.0±1.1
Total Retinal Blood Flow (μL/min)	44.4±8.3	40.1±7.7	39.6±15.4

Table 3.4. Patient demographics and clinical measurements.

3.3.3 Results

Forty-one eyes with DR from 31 patients (ages 62.8±13.4 years, 12 females), 20 eyes without DR from 11 patients (ages 58.8±10.1 years, 5 females), and 16 healthy eyes from 12 subjects (ages 57.9±8.1 years, 8 females) were included in the analysis. The treatment history for the 17 eyes having DME and moderate or severe NDPR is given in Table 3.4.

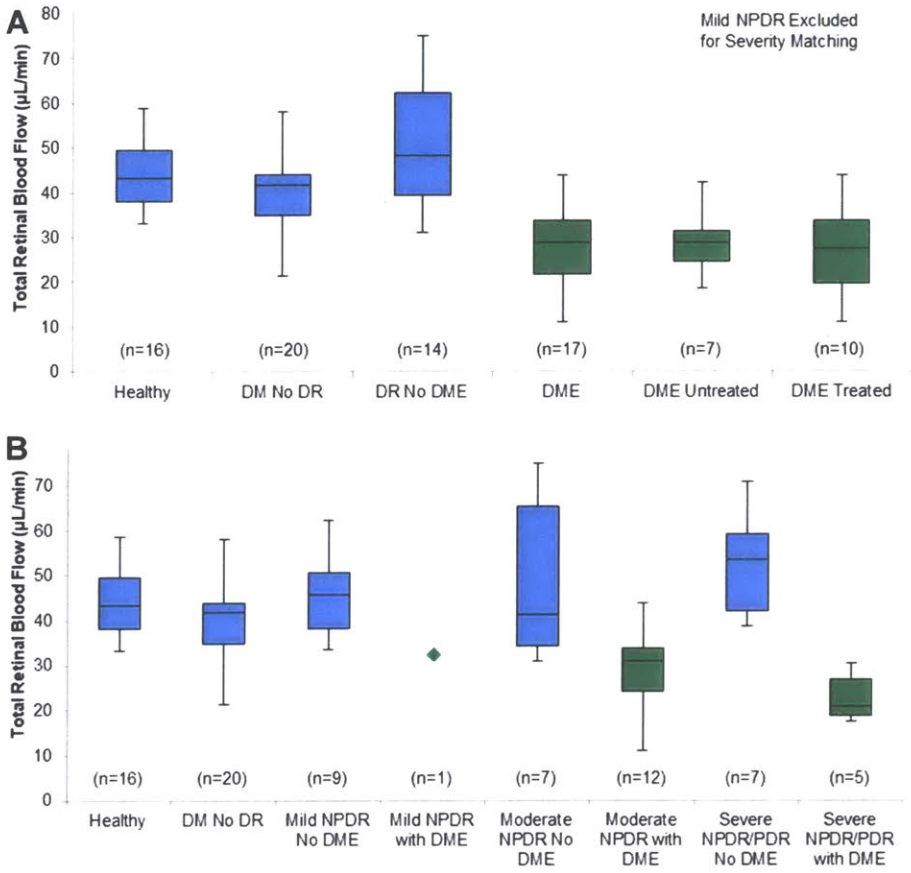

Fig. 3.5. Box plots of TRBF measurements. (A) Box plot of TRBF with respect to disease status and treatment history. Green boxes indicate the eyes with DME. Eyes with mild NPDR were excluded for DR severity matching between DR no DME and DME groups. (B) Box plot of TRBF with respect of DR severity and DME presence. Green boxes indicate the eyes with DME.

There was no significant difference in mean blood pressure or mean ocular perfusion pressure between control and DR groups. Diabetic patients without DR exhibited significantly higher mean blood pressure ($P \leq 0.05$), and mean ocular perfusion pressure ($P \leq 0.05$). The average TRBF (± standard deviation) was 44.4±8.3 µL/min in the healthy eyes, 40.1±7.7 µL/min in the eyes of diabetic patients without DR, 50.9±15.4 µL/min in the DR eyes without DME, and 27.7 ± 8.7 µL/min in the DR eyes with DME. As shown in Fig. 3.5 (A), mean TRBF was significantly decreased in DR eyes with DME compared to both the healthy control group ($P \leq 0.0001$, linear mixed effect model) and DR without DME group ($P \leq 0.0001$, linear mixed effect model). Comparison of mean TRBF between the treatment-naïve (28.7 ± 7.6 µL/min) and treated (27.0 ±

9.8 μL/min) DME groups showed no significant separation between the two groups (P>0.5). For this series of statistical tests, eyes with mild NPDR were excluded in order to match retinopathy severity between DR without DME and DR with DME groups. Fig. 3.5 (B) illustrates that eyes with DME had significantly lower TRBF than healthy range regardless of retinopathy severity.

Amongst eyes with DME, mean TRBF was 30.7 ± 10.2 μL/min (P≤0.002) for the mild/moderate NPDR group and 22.8 ± 5.6 μL/min (P≤0.002) for the severe NPDR/PDR group, both being significantly lower than in normal controls. In contrast, mean TRBF in eyes without DME was not lower compared to the controls. The eyes with mild NPDR without DME had a mean TRBF of 45.4 ± 9.2 μL/min, which was similar to the healthy group. In the eyes with severe NPDR or PDR, without DME, mean TRBF was 52.2 ± 12.2 μL/min, which is higher than in healthy controls, but not statistically significant (P>0.05). Finally, in eyes with moderate NPDR without DME, the mean TRBF was 49.5 ± 19.1 μL/min, covering a wide range from 31.1 μL/min to 75.0 μL/min.

3.3.4 Discussion

Perhaps the most noteworthy finding of this study is that DME eyes exhibit markedly reduced TRBF irrespective of treatment history or DR severity. A study by Guan *et al.* investigated RBF in the superior temporal arterioles of DR eyes using Canon laser blood flowmeter (CLBF). The ratio between the maximum and minimum flow velocities, often referred to as vascular resistivity, was suggested to be a risk factor for DME. However, significant differences were not detected in the vessel diameters, the flow velocity, or the TRBF [38]. Our results showing reduced TRBF in DME are not in agreement with these findings. However, it is important to note that the single-vessel blood flow measurement repeatability using CLBF is relatively poor—the COV in healthy subjects was reported to range from 4.8 to 39.7% and the median was 19.9%

[39]. In contrast, in a study of healthy eyes, the *en face* Doppler OCT method was reported to have a COV ranging from 0.8% to 10.9%, with a median of 6.1% [40]. In the current study, the COV in the 23 DR eyes with more than three valid TRBF measurements fell in between 1.8% and 11.0%, and its median was 7.0%. This corresponded to 3 to 4 μL/min median intra-subject variance, which was considerably smaller than the mean difference between the DME absent and DME present groups.

With regards to a potential causal relationship between reduced TRBF and DME, some groups have commented that the increased tissue hydrostatic pressure associated with DME may cause displacement and disruption of the smaller capillaries and may result in reduced TRBF. Conversely, recent studies have suggested leukostasis, the accumulation of leukocytes on the luminal surface of the retinal capillaries, could be a major contributor in blood-retinal barrier (BRB) dysfunction and the development of capillary non perfusion in diabetics [41]. Histopathologic studies have shown that microaneurysms in DR may be engorged with leukocytes, red blood cell breakdown products and eventually fibers, impeding flow in the retinal microvasculature [42]. It may be that ischemia, as measured by reduced TRBF, creates a VEGF-rich environment that precipitates DME [43]. There is now evidence in the OCTA literature demonstrating that loss of capillary perfusion is correlated with DR severity [44-46] and DME is accompanied by loss of perfusion in the retinal capillaries, especially in the deep capillary plexus, and that these changes may precede the development of edema [47-49]. Interestingly, in the moderate NPDR without DME group, a strongly skewed distribution covering a wide range of TRBF was observed (Fig. 3.6). This distribution suggests that there may be two clusters within the group: the subgroup with higher TRBF could exhibit similar TRBF as in the DME-absent severe NPDR/PDR group, and the subgroup with lower TRBF could have TRBF values

close to that in the groups with DME. However, the current study is very preliminary and it is beyond the scope of this study to draw any definitive conclusions on how DME and reduced TRBF are related.

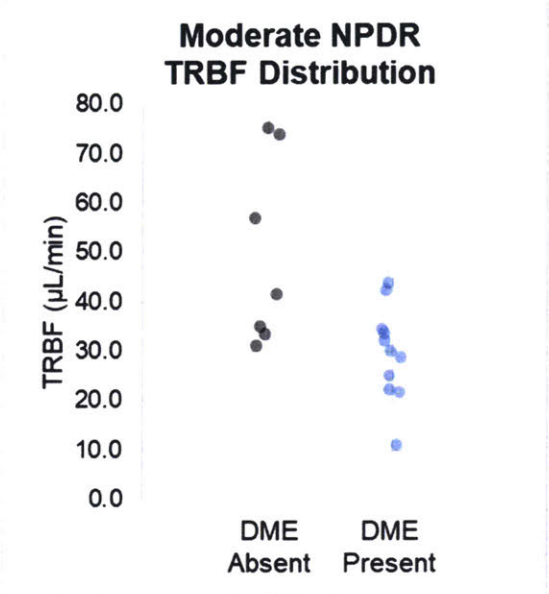

Fig. 3.6. Scatter plot of TRBF versus presence of DME in eyes with moderate NPDR.

According to the prevailing theory in the LDV literature, TRBF in eyes with NPDR is expected to be higher than normal and rising with increasing disease severity [27-32, 50, 51]. Our measurements in the DME-absent eyes with severe NPDR or PDR suggest that there could be a slight increase in TRBF in these groups, although statistical significance was not demonstrated, perhaps due to the small group sizes. Investigators have postulated increased glucose level in diabetes maybe responsible for increased TRBF. LDV studies on type 1 diabetics [52] and type 2 diabetics [53] without clinically pronounced retinopathy both showed that insulin-induced blood glucose decrease caused transient decrease in RBF. Meanwhile, one of these studies also showed that the diabetics without retinopathy presented lower temporal RBF than in normal subjects. These results must be interpreted with caution because insulin

reduces hyperglycemia and dilates the blood vessels at the same time. It is difficult to make any pathophysiological speculations considering the small size of this study.

It is worth noting the possible influence of anti-VEGF treatment on TRBF in the eyes with DME since anti-VEGF agents have been linked to transient reductions in RBF [54-58]. For the six eyes that received anti-VEGF treatment, the injections were given based on a treat-and-extend protocol. Therefore, the timing of the injections was different in all six eyes. Three eyes were treated with anti-VEGF no more than 60 days prior to the *en face* Doppler imaging and their mean TRBF was 25.3 ± 9.2 μL/min. The other three eyes had not received any anti-VEGF treatment within 120 days before the *en face* Doppler measurement and their mean TRBF was 29.4 ± 5.2 μL/min. The similarity of TRBF in the two groups is consistent with OCTA findings in the retinal capillaries [59]. Studies with larger numbers of patients are required to confirm that anti-VEGF treatment is not a major factor for the reduced flow seen in the current study.

The *en face* Doppler volumetric scanning technique used in this study has one key limitation because of its high speed: when there are reflections from hyper-reflective layers such as retinal nerve fiber layer, inner segment/outer segment ellipsoid, and retinal pigment epithelium (RPE), a nonzero Doppler phase can be detected even without any flow. Although our processing software can reduce these artifacts, it is difficult to completely remove the artifacts because the same axial flow velocity corresponds to smaller Doppler phase at higher imaging speeds. These artifacts, especially in subjects with low TRBF, can cause overestimation or underestimation of blood flow depending on the segmentation threshold. Manual inspection of the segmented flow velocity in the *en face* images is required in such cases. A solution for these artifacts is to increase the interscan time between the two A-scans paired for calculating Doppler phase. This can be achieved by doubling the density of the A-scans per unit length and pairing alternate,

rather than subsequent, A-scans. This approach may require cardiac gating [40] because the volume sampling rate of 3.5 volumes/sec may not be enough to accurately capture flow pulsatility. Other limitations of the study include its observational nature. As our recruitment was not guided by *a priori* information from a pilot study, there are subject cohorts that have excessively small group sizes for statistical testing. However, this study itself may serve as a pilot study for future *en face* Doppler OCT investigations of TRBF in DR.

This study used high-speed *en face* Doppler OCT to investigate TRBF in diabetic eyes with or without DR and healthy eyes. TRBF was found to be significantly lower in eyes with DME compared to both the control group and eyes with DR without DME, regardless of retinopathy severity. In eyes with moderate NPDR without DME we observed a strongly skewed TRBF distribution.

References

[1] H. A. Quigley, "Number of people with glaucoma worldwide," *Br J Ophthalmol,* vol. 80, pp. 389-93, May 1996.

[2] H. A. Quigley and A. T. Broman, "The number of people with glaucoma worldwide in 2010 and 2020," *Br J Ophthalmol,* vol. 90, pp. 262-7, Mar 2006.

[3] J. S. Schuman, M. R. Hee, C. A. Puliafito, C. Wong, T. Pedut-Kloizman, C. P. Lin, E. Hertzmark, J. A. Izatt, E. A. Swanson, and J. G. Fujimoto, "Quantification of nerve fiber layer thickness in normal and glaucomatous eyes using optical coherence tomography," *Arch Ophthalmol,* vol. 113, pp. 586-96, May 1995.

[4] G. Wollstein, J. S. Schuman, L. L. Price, A. Aydin, P. C. Stark, E. Hertzmark, E. Lai, H. Ishikawa, C. Mattox, J. G. Fujimoto, and L. A. Paunescu, "Optical coherence tomography longitudinal evaluation of retinal nerve fiber layer thickness in glaucoma," *Arch Ophthalmol,* vol. 123, pp. 464-70, Apr 2005.

[5] G. Wollstein, L. Kagemann, R. A. Bilonick, H. Ishikawa, L. S. Folio, M. L. Gabriele, A. K. Ungar, J. S. Duker, J. G. Fujimoto, and J. S. Schuman, "Retinal nerve fibre layer and visual function loss in glaucoma: the tipping point," *Br J Ophthalmol,* vol. 96, pp. 47-52, Jan 2012.

[6] J. Flammer and S. Orgul, "Optic nerve blood-flow abnormalities in glaucoma," *Prog Retin Eye Res,* vol. 17, pp. 267-89, Apr 1998.

[7] J. Flammer, S. Orgul, V. P. Costa, N. Orzalesi, G. K. Krieglstein, L. M. Serra, J. P. Renard, and E. Stefansson, "The impact of ocular blood flow in glaucoma," *Prog Retin Eye Res,* vol. 21, pp. 359-93, Jul 2002.

[8] G. Fuchsjager-Mayrl, B. Wally, M. Georgopoulos, G. Rainer, K. Kircher, W. Buehl, T. Amoako-Mensah, H. G. Eichler, C. Vass, and L. Schmetterer, "Ocular blood flow and systemic blood pressure in patients with primary open-angle glaucoma and ocular hypertension," *Invest Ophthalmol Vis Sci,* vol. 45, pp. 834-9, Mar 2004.

[9] A. Harris, R. C. Sergott, G. L. Spaeth, J. L. Katz, J. A. Shoemaker, and B. J. Martin, "Color Doppler analysis of ocular vessel blood velocity in normal-tension glaucoma," *Am J Ophthalmol,* vol. 118, pp. 642-9, Nov 15 1994.

[10] H. J. Kaiser, A. Schoetzau, D. Stumpfig, and J. Flammer, "Blood-flow velocities of the extraocular vessels in patients with high-tension and normal-tension primary open-angle glaucoma," *Am J Ophthalmol,* vol. 123, pp. 320-7, Mar 1997.

[11] M. Emre, S. Orgul, K. Gugleta, and J. Flammer, "Ocular blood flow alteration in glaucoma is related to systemic vascular dysregulation," *Br J Ophthalmol,* vol. 88, pp. 662-6, May 2004.

[12] H. S. Chung, A. Harris, L. Kagemann, and B. Martin, "Peripapillary retinal blood flow in normal tension glaucoma," *Br J Ophthalmol,* vol. 83, pp. 466-9, Apr 1999.

[13] J. F. Logan, S. J. Rankin, and A. J. Jackson, "Retinal blood flow measurements and neuroretinal rim damage in glaucoma," *Br J Ophthalmol,* vol. 88, pp. 1049-54, Aug 2004.

[14] M. T. Nicolela, P. Hnik, and S. M. Drance, "Scanning laser Doppler flowmeter study of retinal and optic disk blood flow in glaucomatous patients," *Am J Ophthalmol,* vol. 122, pp. 775-83, Dec 1996.

[15] Y. Jia, E. Wei, X. Wang, X. Zhang, J. C. Morrison, M. Parikh, L. H. Lombardi, D. M. Gattey, R. L. Armour, B. Edmunds, M. F. Kraus, J. G. Fujimoto, and D. Huang, "Optical

coherence tomography angiography of optic disc perfusion in glaucoma," *Ophthalmology,* vol. 121, pp. 1322-32, Jul 2014.
[16] A. Bill and G. O. Sperber, "Control of retinal and choroidal blood flow," *Eye (Lond),* vol. 4 (Pt 2), pp. 319-25, 1990.
[17] C. Delaey and J. Van De Voorde, "Regulatory mechanisms in the retinal and choroidal circulation," *Ophthalmic Res,* vol. 32, pp. 249-56, Nov-Dec 2000.
[18] J. Kur, E. A. Newman, and T. Chan-Ling, "Cellular and physiological mechanisms underlying blood flow regulation in the retina and choroid in health and disease," *Prog Retin Eye Res,* vol. 31, pp. 377-406, Sep 2012.
[19] P. Brusini and S. Filacorda, "Enhanced Glaucoma Staging System (GSS 2) for classifying functional damage in glaucoma," *J Glaucoma,* vol. 15, pp. 40-6, Feb 2006.
[20] Y. Wang, A. A. Fawzi, R. Varma, A. A. Sadun, X. Zhang, O. Tan, J. A. Izatt, and D. Huang, "Pilot study of optical coherence tomography measurement of retinal blood flow in retinal and optic nerve diseases," *Invest Ophthalmol Vis Sci,* vol. 52, pp. 840-5, Feb 2011.
[21] M. M. Engelgau, L. S. Geiss, J. B. Saaddine, J. P. Boyle, S. M. Benjamin, E. W. Gregg, E. F. Tierney, N. Rios-Burrows, A. H. Mokdad, E. S. Ford, G. Imperatore, and K. M. Narayan, "The evolving diabetes burden in the United States," *Ann Intern Med,* vol. 140, pp. 945-50, Jun 1 2004.
[22] B. Thylefors, A. D. Negrel, R. Pararajasegaram, and K. Y. Dadzie, "Global data on blindness," *Bull World Health Organ,* vol. 73, pp. 115-21, 1995.
[23] B. Thylefors, "A global initiative for the elimination of avoidable blindness," *Community Eye Health,* vol. 11, pp. 1-3, 1998.
[24] N. Takase, M. Nozaki, A. Kato, H. Ozeki, M. Yoshida, and Y. Ogura, "Enlargement of Foveal Avascular Zone in Diabetic Eyes Evaluated by En Face Optical Coherence Tomography Angiography," *Retina,* vol. 35, pp. 2377-83, Nov 2015.
[25] T. S. Hwang, Y. Jia, S. S. Gao, S. T. Bailey, A. K. Lauer, C. J. Flaxel, D. J. Wilson, and D. Huang, "Optical Coherence Tomography Angiography Features of Diabetic Retinopathy," *Retina,* vol. 35, pp. 2371-6, Nov 2015.
[26] T. E. de Carlo, A. T. Chin, M. A. Bonini Filho, M. Adhi, L. Branchini, D. A. Salz, C. R. Baumal, C. Crawford, E. Reichel, A. J. Witkin, J. S. Duker, and N. K. Waheed, "Detection of Microvascular Changes in Eyes of Patients with Diabetes but Not Clinical Diabetic Retinopathy Using Optical Coherence Tomography Angiography," *Retina,* vol. 35, pp. 2364-70, Nov 2015.
[27] E. M. Kohner, A. M. Hamilton, S. J. Saunders, B. A. Sutcliffe, and C. J. Bulpitt, "The retinal blood flow in diabetes," *Diabetologia,* vol. 11, pp. 27-33, Feb 1975.
[28] J. G. Cunha-Vaz, J. R. Fonseca, J. R. de Abreu, and J. J. Lima, "Studies on retinal blood flow. II. Diabetic retinopathy," *Arch Ophthalmol,* vol. 96, pp. 809-11, May 1978.
[29] G. T. Feke, H. Tagawa, A. Yoshida, D. G. Goger, J. J. Weiter, S. M. Buzney, and J. W. McMeel, "Retinal circulatory changes related to retinopathy progression in insulin-dependent diabetes mellitus," *Ophthalmology,* vol. 92, pp. 1517-22, Nov 1985.
[30] A. Yoshida, G. T. Feke, J. Morales-Stoppello, G. D. Collas, D. G. Goger, and J. W. McMeel, "Retinal blood flow alterations during progression of diabetic retinopathy," *Arch Ophthalmol,* vol. 101, pp. 225-7, Feb 1983.

[31] J. E. Grunwald, C. E. Riva, J. Baine, and A. J. Brucker, "Total retinal volumetric blood flow rate in diabetic patients with poor glycemic control," *Invest Ophthalmol Vis Sci,* vol. 33, pp. 356-63, Feb 1992.

[32] V. Patel, S. Rassam, R. Newsom, J. Wiek, and E. Kohner, "Retinal blood flow in diabetic retinopathy," *BMJ,* vol. 305, pp. 678-83, Sep 19 1992.

[33] N. P. Blair, G. T. Feke, J. Morales-Stoppello, C. E. Riva, D. G. Goger, G. Collas, and J. W. McMeel, "Prolongation of the retinal mean circulation time in diabetes," *Arch Ophthalmol,* vol. 100, pp. 764-8, May 1982.

[34] Z. Burgansky-Eliash, D. A. Nelson, O. P. Bar-Tal, A. Lowenstein, A. Grinvald, and A. Barak, "Reduced retinal blood flow velocity in diabetic retinopathy," *Retina,* vol. 30, pp. 765-73, May 2010.

[35] A. Mendivil, V. Cuartero, and M. P. Mendivil, "Ocular blood flow velocities in patients with proliferative diabetic retinopathy and healthy volunteers: a prospective study," *Br J Ophthalmol,* vol. 79, pp. 413-6, May 1995.

[36] T. J. Fallon, P. Chowiencyzk, and E. M. Kohner, "Measurement of retinal blood flow in diabetes by the blue-light entoptic phenomenon," *Br J Ophthalmol,* vol. 70, pp. 43-6, Jan 1986.

[37] "Grading diabetic retinopathy from stereoscopic color fundus photographs--an extension of the modified Airlie House classification. ETDRS report number 10. Early Treatment Diabetic Retinopathy Study Research Group," *Ophthalmology,* vol. 98, pp. 786-806, May 1991.

[38] K. Guan, C. Hudson, T. Wong, M. Kisilevsky, R. K. Nrusimhadevara, W. C. Lam, M. Mandelcorn, R. G. Devenyi, and J. G. Flanagan, "Retinal hemodynamics in early diabetic macular edema," *Diabetes,* vol. 55, pp. 813-8, Mar 2006.

[39] K. Guan, C. Hudson, and J. G. Flanagan, "Variability and repeatability of retinal blood flow measurements using the Canon Laser Blood Flowmeter," *Microvasc Res,* vol. 65, pp. 145-51, May 2003.

[40] B. Lee, W. Choi, J. J. Liu, C. D. Lu, J. S. Schuman, G. Wollstein, J. S. Duker, N. K. Waheed, and J. G. Fujimoto, "Cardiac-Gated En Face Doppler Measurement of Retinal Blood Flow Using Swept-Source Optical Coherence Tomography at 100,000 Axial Scans per Second," *Invest Ophthalmol Vis Sci,* vol. 56, pp. 2522-30, Apr 2015.

[41] X. Zhang, H. Zeng, S. Bao, N. Wang, and M. C. Gillies, "Diabetic macular edema: new concepts in patho-physiology and treatment," *Cell Biosci,* vol. 4, p. 27, 2014.

[42] A. W. Stitt, T. A. Gardiner, and D. B. Archer, "Histological and ultrastructural investigation of retinal microaneurysm development in diabetic patients," *Br J Ophthalmol,* vol. 79, pp. 362-7, Apr 1995.

[43] Q. D. Nguyen, S. M. Shah, E. Van Anden, J. U. Sung, S. Vitale, and P. A. Campochiaro, "Supplemental oxygen improves diabetic macular edema: a pilot study," *Invest Ophthalmol Vis Sci,* vol. 45, pp. 617-24, Feb 2004.

[44] S. A. Agemy, N. K. Scripsema, C. M. Shah, T. Chui, P. M. Garcia, J. G. Lee, R. C. Gentile, Y. S. Hsiao, Q. Zhou, T. Ko, and R. B. Rosen, "Retinal Vascular Perfusion Density Mapping Using Optical Coherence Tomography Angiography in Normals and Diabetic Retinopathy Patients," *Retina,* vol. 35, pp. 2353-63, Nov 2015.

[45] A. Y. Kim, Z. Chu, A. Shahidzadeh, R. K. Wang, C. A. Puliafito, and A. H. Kashani, "Quantifying Microvascular Density and Morphology in Diabetic Retinopathy Using

Spectral-Domain Optical Coherence Tomography Angiography," *Invest Ophthalmol Vis Sci,* vol. 57, pp. OCT362-70, Jul 1 2016.

[46] D. Bhanushali, N. Anegondi, S. G. Gadde, P. Srinivasan, L. Chidambara, N. K. Yadav, and A. Sinha Roy, "Linking Retinal Microvasculature Features With Severity of Diabetic Retinopathy Using Optical Coherence Tomography Angiography," *Invest Ophthalmol Vis Sci,* vol. 57, pp. OCT519-25, Jul 1 2016.

[47] N. Hasegawa, M. Nozaki, N. Takase, M. Yoshida, and Y. Ogura, "New Insights Into Microaneurysms in the Deep Capillary Plexus Detected by Optical Coherence Tomography Angiography in Diabetic Macular Edema," *Invest Ophthalmol Vis Sci,* vol. 57, pp. Oct348-Oct355, Jul 2016.

[48] T. E. de Carlo, A. T. Chin, T. Joseph, C. R. Baumal, A. J. Witkin, J. S. Duker, and N. K. Waheed, "Distinguishing Diabetic Macular Edema From Capillary Nonperfusion Using Optical Coherence Tomography Angiography," *Ophthalmic Surg Lasers Imaging Retina,* vol. 47, pp. 108-14, Feb 2016.

[49] R. F. Spaide, "Volume-Rendered Optical Coherence Tomography of Diabetic Retinopathy Pilot Study," *Am J Ophthalmol,* vol. 160, pp. 1200-10, Dec 2015.

[50] B. Pemp, E. Polska, G. Garhofer, M. Bayerle-Eder, A. Kautzky-Willer, and L. Schmetterer, "Retinal blood flow in type 1 diabetic patients with no or mild diabetic retinopathy during euglycemic clamp," *Diabetes Care,* vol. 33, pp. 2038-42, Sep 2010.

[51] H. T. Nguyen, E. van Duinkerken, F. D. Verbraak, B. C. Polak, P. J. Ringens, M. Diamant, and A. C. Moll, "Retinal blood flow is increased in type 1 diabetes mellitus patients with advanced stages of retinopathy," *BMC Endocr Disord,* vol. 16, p. 25, May 26 2016.

[52] S. E. Bursell, A. C. Clermont, B. T. Kinsley, D. C. Simonson, L. M. Aiello, and H. A. Wolpert, "Retinal blood flow changes in patients with insulin-dependent diabetes mellitus and no diabetic retinopathy," *Invest Ophthalmol Vis Sci,* vol. 37, pp. 886-97, Apr 1996.

[53] J. E. Grunwald, C. E. Riva, D. B. Martin, A. R. Quint, and P. A. Epstein, "Effect of an insulin-induced decrease in blood glucose on the human diabetic retinal circulation," *Ophthalmology,* vol. 94, pp. 1614-20, Dec 1987.

[54] P. Bonnin, J. A. Pournaras, Z. Lazrak, S. Y. Cohen, J. F. Legargasson, A. Gaudric, B. I. Levy, and P. Massin, "Ultrasound assessment of short-term ocular vascular effects of intravitreal injection of bevacizumab (Avastin((R))) in neovascular age-related macular degeneration," *Acta Ophthalmol,* vol. 88, pp. 641-5, Sep 2010.

[55] A. Mete, O. Saygili, K. Gungor, M. Bayram, and N. Bekir, "Does ranibizumab (Lucentis(R)) change retrobulbar blood flow in patients with neovascular age-related macular degeneration?," *Ophthalmic Res,* vol. 47, pp. 141-5, 2012.

[56] H. Hosseini, M. Lotfi, M. H. Esfahani, N. Nassiri, M. R. Khalili, M. R. Razeghinejad, and K. Nouri-Mahdavi, "Effect of intravitreal bevacizumab on retrobulbar blood flow in injected and uninjected fellow eyes of patients with neovascular age-related macular degeneration," *Retina,* vol. 32, pp. 967-71, May 2012.

[57] Y. B. Sakalar, S. Senturk, M. Yildirim, U. Keklikci, M. F. Alakus, and K. Unlu, "Evaluation of retrobulbar blood flow by color doppler ultrasonography after intravitreal ranibizumab injection in patients with neovascular age-related macular degeneration," *J Clin Ultrasound,* vol. 41, pp. 32-7, Jan 2013.

[58] P. Bonnin, J. A. Pournaras, K. Makowiecka, V. Krivosic, A. W. Kedra, J. F. Le Gargasson, A. Gaudric, B. I. Levy, Y. S. Cohen, R. Tadayoni, and P. Massin,

"Ultrasound assessment of ocular vascular effects of repeated intravitreal injections of ranibizumab for wet age-related macular degeneration," *Acta Ophthalmol,* vol. 92, pp. e382-7, Aug 2014.

[59] V. Mané, B. Dupas, A. Gaudric, S. Bonnin, A. Pedinielli, E. Bousquet, A. Erginay, R. Tadayoni, and A. Couturier, "Correlation Between Cystoid Spaces in Chronic Diabetic Macular Edeme and Capillary Nonperfusion Detected by Optical Coherence Tomography Angiography," *Retina,* Sep 2016.

Chapter 4
Photoreceptor Layer Imaging using Ultrahigh-Resolution SD-OCT with Reference Arm Length Modulation

4.1 Motivation

OCT imaging of the human retina has substantially impacted the diagnosis, monitoring, and treatment of retinal and optic nerve diseases. In OCT, unlike in conventional microscopy, the axial resolution is determined not by the scanning optics but by the spectral bandwidth. Using this property, ultrahigh-resolution spectral/Fourier-domain OCT (UHR SD-OCT) employs wideband light sources to achieve axial resolutions below the standard, ~5 μm, axial resolutions of commercial SD-OCT instruments [1-3]. Compared to contemporaneous OCT developments, such as high-speed imaging, the clinical adoption of UHR SD-OCT has been relatively tepid, despite studies demonstrating that UHR SD-OCT provides improved visualization of structural details, such as drusen and pigment migration, that are important markers of age-relative macular degeneration (AMD) progression [4-7].

The relatively slow adoption of UHR SD-OCT is likely due in part to certain technical limitations not present in standard-resolution SD-OCT. First, the imaging speed of SD-OCT is governed by the line-scan rate of the camera. While some camera products allow the line rate to be increased at the tradeoff of using fewer pixels, the increased spectral bandwidth of UHR SD-OCT necessitates more pixels-per-A-scan to maintain the same depth range, resulting in either slower A-scan rates or shorter depth ranges [8]. Neither of these compromises is desirable, particularly considering that swept-source/Fourier-domain OCT (SS-OCT)—the main technological competitor to SD-OCT—allows for both high A-scan rates and long depth ranges [9, 10]. Moreover, the curvature of the retina introduces a natural depth variation in the OCT

image, which puts a lower limit on the needed depth range. Second, compared to standard resolution SD-OCT, UHR SD-OCT requires more complex spectrometer designs with multi-element f-θ lenses to achieve diffraction-limited optical performance across the extended spectral bandwidth. Third, the ergonomics of UHR SD-OCT imaging are more challenging than standard resolution OCT: the shortened depth range and increased depth-dependent signal roll-off, which, all else being equal, increases with optical bandwidth, make UHR SD-OCT sensitive to precise alignment. Lastly, post-processing and image calibration of UHR SD-OCT requires precise compensation of group delay dispersion ("dispersion") across the extended optical bandwidth.

In this chapter, we present a UHR SD-OCT imaging instrument with improved A-scan rate and extendable effective depth range. The instrument is based on a custom spectrometer design that achieves 2.4 μm raw-spectrum axial resolution and 3.1 μm spectrally-shaped axial resolution over 1.4 mm depth range (in tissue) by attaining diffraction-limited spectral resolution over 767-915 nm wavelength range, projected onto a line-scan camera that allowed high-speed imaging at from 80 kHz to 250 kHz line rates. In order to overcome the limitation on the depth range, reference arm length modulation (ReALM), described in the *Optical Instrumentation* section, was developed to extend the effective depth range. Healthy subjects and patients with AMD or proliferative diabetic retinopathy (PDR) were imaged to demonstrate feasibility.

4.2 Methods

4.2.1 Optical Instrumentation

The overall schematic diagram of the system is shown in Fig. 4.1 (A). The major components of the instrument are: a broadband light source, a fiber-optic coupler, a patient imaging interface

with a two-axis scanning mirror system, a reference arm with a rapidly tunable optical path length, a spectrometer, and a computer for data acquisition and system controlling.

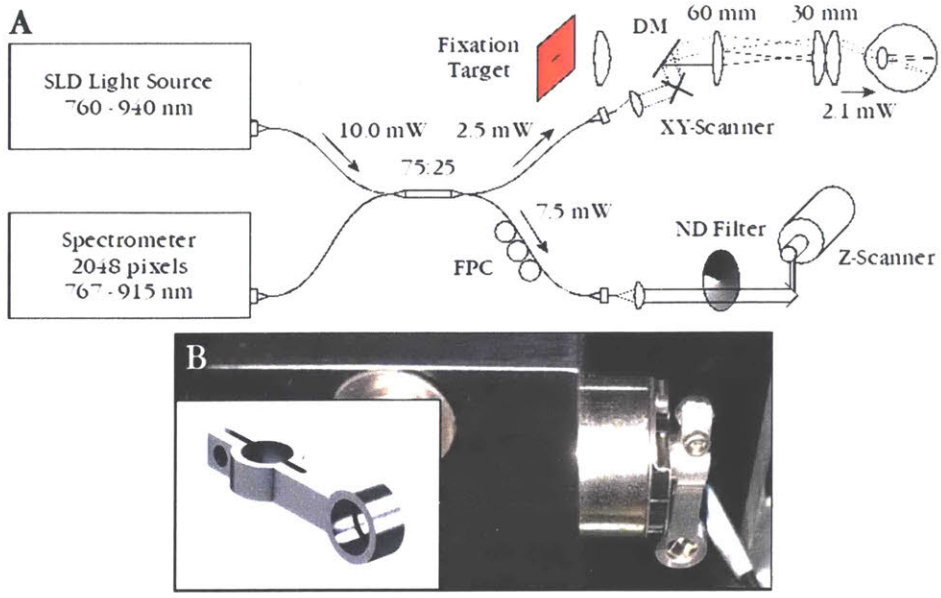

Fig. 4.1. (A) Schematic diagram of the UHR OCT system. DM: dichroic mirror, FPC: fiber polarization controller. (B) Photo of the corner cube retroreflector mounted to the Z-scanner and the 3D model of the mounting arm.

The broadband light source was a commercially available superluminescent diode array (cBLMD-T-850-HP-I, Superlum, Ireland) emitting ~10 mW output power distributed over a 760 nm to 940 nm wavelength range; the power spectral density is shown in Fig. 4.2 (A). The light source module was equipped with a built-in isolator for feedback damage prevention and a USB virtual serial port for control. The light source output was sent to a broadband fiber-optic coupler with a 75:25 coupling ratio (TW850R2A2, Thorlabs, Newton, NJ), which distributed the power to the sample and reference arms. Since the source had sufficient power, a high coupling ratio was chosen to maximize the power transfer efficiency from the sample backscattering to the spectrometer. The patient imaging interface in the sample arm comprised a collimator lens with a 20 mm focal length, a pair of galvanometric mirror scanners, a scan lens with a 30 mm diameter and a 60 mm focal length, and an eyepiece with a 25 mm diameter and a 30 mm effective focal

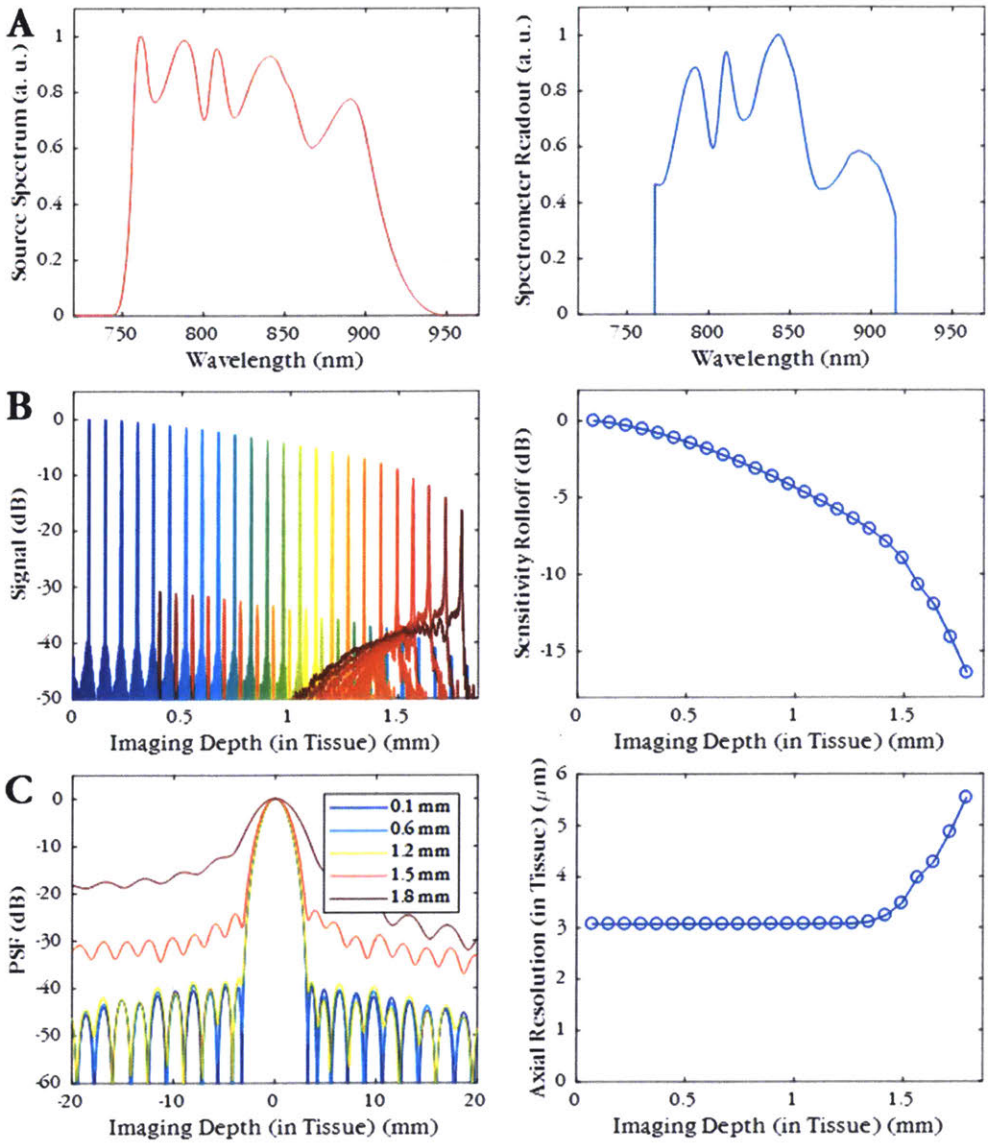

Fig. 4.2. (A) Source power spectrum measured at the laser output and reference arm power spectrum received by the OCT spectrometer. (B) Signal roll-off with imaging depth represented by declining point spread functions and their peak magnitudes plotted as a function of depth. (C) Depth profile of the point spread function at various depths and the full width at half-maximum (FWHM) axial resolution plotted as a function of depth.

length. The incident beam onto the cornea had a 1.8 mm beam diameter and carried 2.1 mW of power, lower than the safety limit for a 10-second exposure to a stationary beam according to the American National Standards Institute (ANSI). Laser interlock using an independent microcontroller was connected to the mirror scanner monitor channels and an external optical

power monitor so that the illumination beam will be cut off in cases where the mirror scanners stop or the laser power increases.

The spectrometer (Cobra-S C-00359, Wasatch Photonics, Durham, NC) was based on a 2048-pixel line-scan CMOS camera (Octopus, e2v, Chelmsford, England) which operates at line rates from 80 kHz to 250 kHz. The spectrometer was aligned to read the output power spectrum from 767 nm to 915 nm, cutting out the longer wavelengths from 915 nm to 940 nm to achieve an adequate depth range. The resulting axial resolution in terms of the full-width at half-maximum (FWHM) amplitude in tissue (n = 1.3375) was 2.4 μm with the raw spectrum and 3.1 μm with a Taylor-windowed spectrum. The signal roll-off was 6 dB at 1.2 mm imaging depth in tissue, as shown in Fig. 4.2 (B). With appropriate image processing, the axial point spread function was nearly constant up to 1.4 mm imaging depth in tissue, as plotted in Fig 2 (C). The camera readout was transferred to the computer by a frame grabber (Xcelera-CL+ PX8 Full, Teledyne DALSA, Billerica, MA) with a maximum data width of 80 bits, capable of capturing the full 12 bits of the camera pixel readout at speeds of up to 128 kHz, and the first 10 bits up to 250 kHz through the Camera Link interface. Using an illumination power of 2.1 mW, the imaging sensitivity defined by the signal-to-noise ratio limit was 102.4 dB at the top of the imaging range at a 128 kHz A-scan rate and 99.1 dB at a 250 kHz A-scan rate.

4.2.2 Reference Arm Length Modulation (ReALM)

4.2.2.1 Physical Implementation of ReALM

The curvature of the retina, combined with UHR SD-OCT's inherently short depth range, results in axial variation in imaging depth, causing "wrap-around" artifacts at the volume's corners and/or signal loss near the volume's center; these imperfections are exacerbated by larger fields-

of-view. To overcome this limitation, we developed reference arm length modulation (ReALM), which performs intra-acquisition adjustment of the reference arm's optical path length to compensate for changes in axial position caused by retinal curvature. We implemented ReALM using a small corner-cube retroreflector prism mounted on a custom mechanical part attached to a high-torque galvanometer scanner (6240H, Cambridge Technologies, MA); the 3D model of the custom mechanical part used for mounting the corner cube is shown in Fig. 4.1 (B). With reference to Fig. 4.1 (A), the z-scan galvanometer rotation results in a corresponding adjustment of the reference arm optical path length. Fig. 4.3 shows how ReALM can move the axial imaging window to keep the retina within the high-signal range, while avoiding signal "wrap-around." Although used for a different purpose, this adjustment mechanism is the same as the longitudinal scanner in time-domain OCT [11] and the phase-shifter for full-range OCT [12].

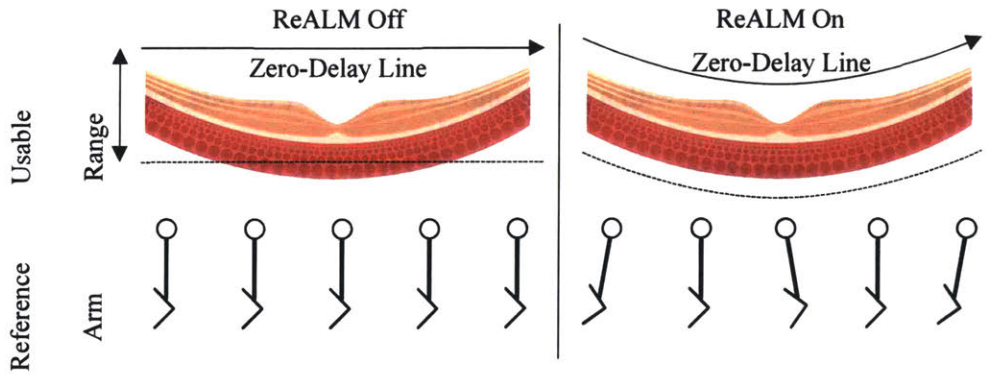

Fig. 4.3. Visual explanation of reference arm length modulation (ReALM). Changing the reference arm optical path length during OCT scan moves the axial imaging window to keep the retina within the high-signal zone close to, but strictly below, the zero-delay line.

4.2.2.2 Estimation of Retinal Curvature

The tilt and curvature of the retina was estimated upon real-time user request based on the image in the horizontal and vertical preview scans for image acquisition. This estimation process was performed in four steps. First, the image was filtered with a Gaussian kernel with sigma of 10

pixels. Second, the image was binarized using a preset threshold. Third, for every A-scan, the weighted average of the axial position of the "white" pixels was calculated with the weights being the pixel values in the filtered image. Lastly, the axial position data was fit with a quadratic curve using least squares method. The horizontal and vertical "tilt" corresponded to the first order terms in the regression formula. The second order coefficients calculated in the horizontal and vertical previews, respectly, were averaged to determine the final retinal curvature. Then, the ReALM scanner's trajectories for both preview scan and the data acquisition scan was updated according to the estimated retinal curvature and tilt. This whole process was almost instantaneous and could be re-evaluated at any time point in the imaging session depending on the operator's judgement.

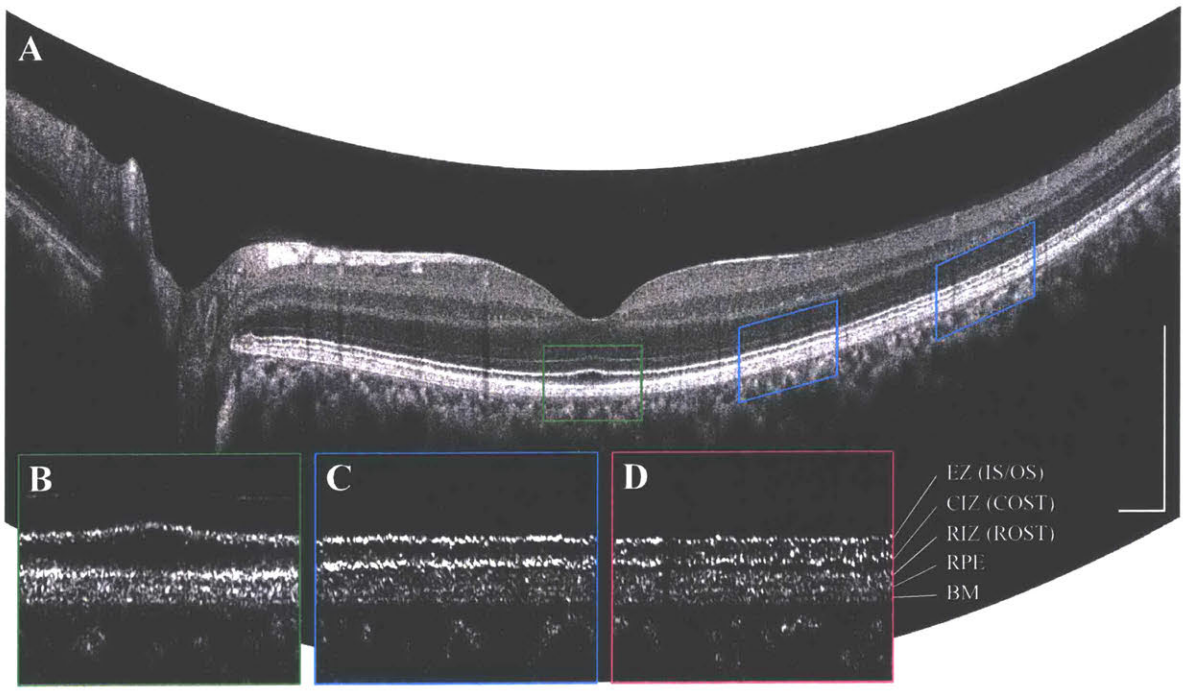

Fig. 4.4. (A) 12 mm horizontal scan comprising 12,000 A-scans, acquired with inter-B-scan ReALM. (B-D) BM-flattened, amplitude-scale, 1 mm×200 μm images of the outer retina in the area demarcated by the colored lines. CIZ (COST) appeared the brightest at the fovea (B), while RIZ (ROST) appeared the brightest 4mm temporal to the fovea (D). Scale bars: 500 μm.

4.2.2.3 Inter-B-scan and Intra-B-scan ReALM

For volumetric scans with high B-scan rates, the reference arm length is only modulated inter-B-scan, not intra-B-scan: the tuning speeds required for intra-B-scan modulation of a high-speed acquisition cause fringe washout [13]. However, for high-density scans with slower B-scan-rates, inter- and intra-B-scan ReALM can be performed without substantial fringe washout. Limitations related to fringe washout effects are further discussed in *Discussion*. The high-density B-scan featured in Fig. 4.4 was acquired with intra-B-scan ReALM and the retinal curvature was restored in post-processing. Fig. 4.4 (B-D) shows a magnified view of the outer retina flattened with respect to Bruch's membrane (BM). The highly scattering bands corresponding to inner segment-outer segment junction (IS/OS), which is also known as ellipsoid zone (EZ), cone outer segment tips (COST), which is also known as cone interdigitation zone (CIZ), rod outer segment tips (ROST), which is also known as rod interdigitation zone (RIZ), retinal pigment epithelium (RPE), and BM are clearly distinguishable. Imaging of the photoreceptor layer in healthy eyes and eyes with AMD is presented in *Results*.

4.2.3 SD-OCT Image Processing

The process of converting spectrometer readout into an OCT A-scan can be broken into four steps: background subtraction, resampling into uniform-in-wavenumber space, dispersion compensation, and discrete Fourier transform. These four steps are outlined below.

For data acquired with ReALM, we found that simple subtraction of the pre-acquired reference arm power spectrum is not sufficiently accurate, often leaving residual line artifacts near the top of the processed images; the likely culprit is the high-torque galvanometer scanner, which introduces small rotations and lateral displacements of the corner-cube prism, causing

time-variations in the back-coupled optical power. Fortunately, we can utilize the fluctuations in the power spectral density of the broadband light source to perform a regression, with the averaged reference arm spectrum as the independent variable and the interference fringe as the dependent variable. Using this method, corner cube alignment changes and air flow perturbations can be computationally removed, leaving interferometric terms only. The regression formula was modeled as below:

$$(y_i - d) = (a_0 + a_1 i + a_2 i^2)(x_i - d),$$

where y_i is the interference fringe, x_i is the averaged pre-acquired reference arm spectrum, d is the dark current, and $a_i = a_0 + a_1 i + a_2 i^2$ is the scaling factor, which is a quadratic function of the pixel index i. The quadratic function was chosen for two reasons: first, small misalignment of the corner cube caused by ReALM may cause linear or quadratic spectral skew of the background; second, the sample arm's power spectrum, which also contributes to the background, is typically somewhat different from the reference arm's power spectrum, potentially due to the spectral variation of the tissue scattering and the fiber-optic coupler's coupling ratio. Under the assumptions $a_1 i, a_2 i^2 \square\ a_0$ for all i, this equation can be approximated by the following regression equation:

$$y_i = (a_0 + a_1 i + a_2 i^2) x_i + b,$$

where $b = (1 - a_0)d$. Once the coefficients a_0, a_1, a_2 and b are determined by the least squares method, the adaptively scaled background line $\hat{y}_i$ can be calculated by

$$\hat{y}_i = (a_0 + a_1 i + a_2 i^2) x_i + b.$$

The background-subtracted interference fringes were resampled at uniform-in-wavenumber locations, which were estimated from the extracted phase delay of an air gap. More specifically,

the fringes were eight times upsampled by zero-padding, and were then resampled via linear interpolation. The upsampling factor and the interpolation method were empirically determined according to the signal roll-off performance. After resampling, the group delay dispersion mismatch between the sample and reference arms was compensated using an image-based algorithm previously implemented by our group [14]. The interference fringe was then rescaled to match a Taylor window—a variant of the Chebyshev window that allows the power tradeoff between the main lobe and the side lobes while minimizing the main lobe width—with seven nearly constant side lobes. Finally, the interference fringes were converted into OCT images by taking the magnitude of their discrete Fourier transforms.

4.2.4 Motion Correction

The motion correction algorithm previously developed by our group [15, 16] can be applied to an orthogonal raster scan pair with symmetric dimensions along the fast-scan and slow-scan directions. This motion correction algorithm extracts the eye motion based on the assumption that the A-scans are acquired at constant rate and that the speed of eye motion has an upper bound. The algorithm estimates the three-dimensional displacement vector of the retinal image as a function of time, or A-scan index, and removes motion. Then, it merges the two motion-corrected volumes to create a motion-free, signal-enhanced volume.

While this technique has been demonstrated previously, and is currently used in some commercial SD-OCT systems [17, 18], its compatibility with UHR OCT and ReALM is not *a priori* evident. Fig. 4.5 shows two orthogonal raster scan volumes acquired with ReALM and the resulting motion-free volume after applying the image registration and merging, which attests to a global-scale compatibility of both ReALM and our motion correction algorithm. This

compatibility can be understood by noting that small displacements of the reference optical path length, such as those induced by ReALM, are equivalent to slow-axis eye motion. The first two rows of Fig. 4.5 show that the retinal image in the slow-scan cross-sections extracted from the uncorrected volumes is nearly flat because the retinal curvature was tracked by ReALM; the final row shows that the retinal curvature was restored in the merged volume by motion correction.

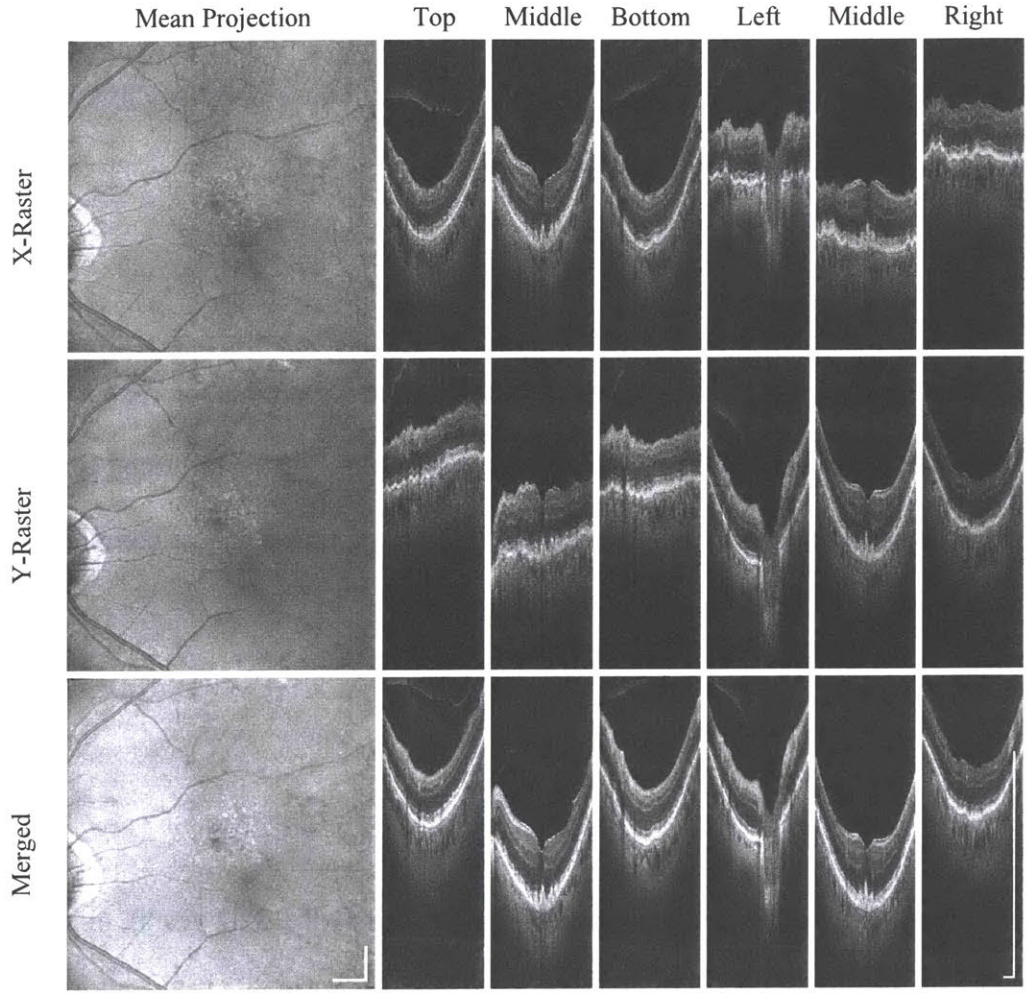

Fig. 4.5. Demonstration of UHR OCT image acquisition and processing with inter-B-scan ReALM and motion correction of a 500 × 500 A-scan volume over 9 mm × 9 mm macular area of an eye with dry AMD. Top two rows: ReALM automatically compensates for the variation in the axial position of the retinal image across different B-scans; if the middle B-scan is aligned within the axial imaging range, the top and bottom B-scans would also be within the range. Bottom row: motion correction removes the axial displacement introduced either by patient motion or by ReALM. The result is motion-free merged volume with enhanced signal. Scale bars: 1 mm.

4.2.5 Layer Segmentation for en Face Image Analysis

An algorithm based on Dijkstra's minimum-weight-path search was used to segment contours representing the IS/OS (EZ), RPE, and BM were automatically segmented in each B-scan of the 6 mm×6 mm motion-corrected volumes acquired from two dry AMD eyes with clearly visible drusen. For one healthy eye, IS/OS, COST (CIZ), ROST (RIZ), RPE, and BM were segmented to generate en face maps of backscattering from the COST (CIZ), and ROST (RIZ). This algorithm was similar to the seven-layer segmentation [19, 20] developed by Chiu, et al. but only searched for three outer retinal bands for time efficiency.

4.2.6 Subject Recruitment

Images of healthy control eyes and eyes with dry AMD were acquired at the New England Eye Center at Tufts Medical Center (Boston, Massachusetts, USA). Written informed consent was received from the patients prior to imaging and the recruiting procedure was compliant to the declaration of Helsinki.

4.3 Results

4.3.1 Overview

We imaged six healthy eyes from six subjects (1 female, age 41.8 ± 22.2 years), nine eyes with dry AMD from eight patients (1 female, age 78.0 ± 9.9 years), and three eyes with proliferative diabetic retinopathy (PDR) from three patients (3 female, age 37, 38, 68 years), all at 128 kHz A-scan rate. The imaging results are reported below.

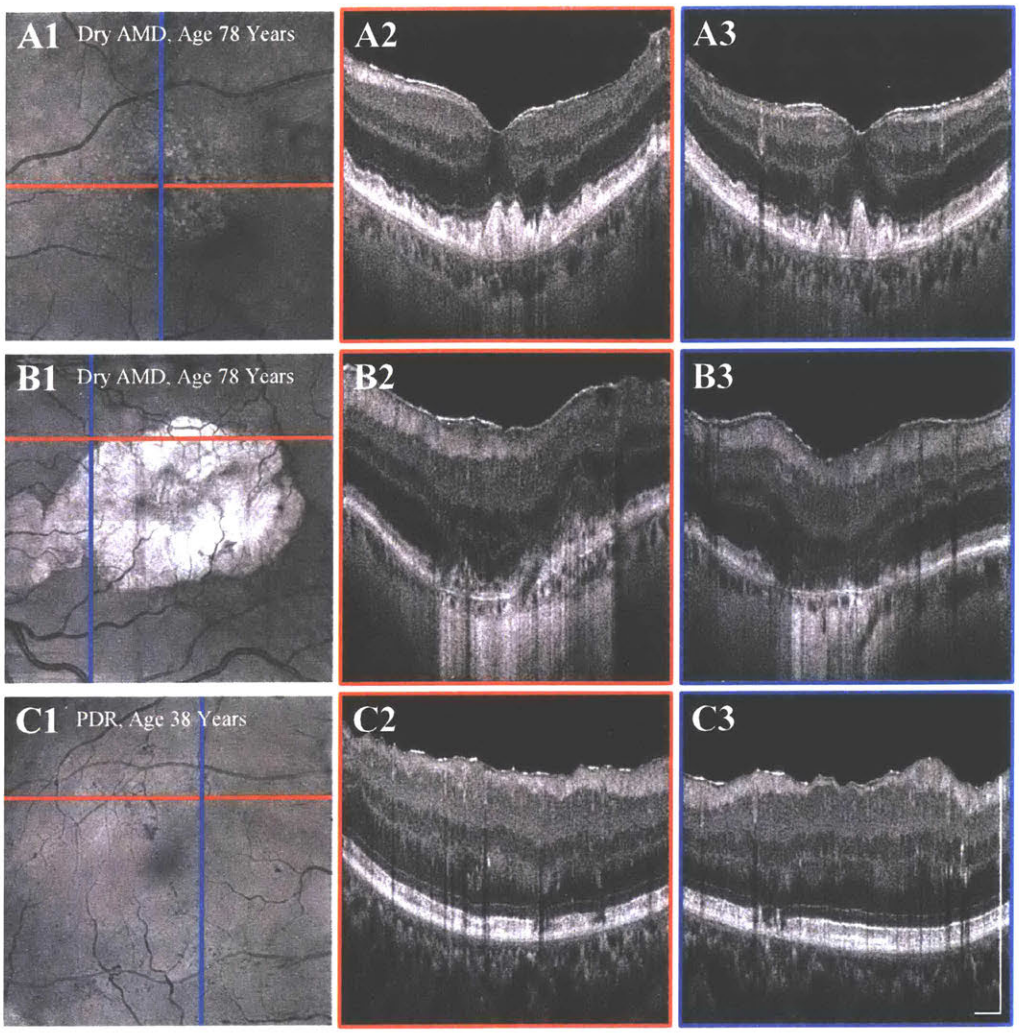

Fig. 4.6. Examples of motion-corrected UHR-OCT images comprising 500×500 A-scans covering 6 mm×6 mm macular area in eyes with (A) dry AMD with drusen, (B) dry AMD with geographic atrophy, (C) proliferative diabetic retinopathy. Vertical and horizontal B-scan excerpts are labeled with red and blue lines, respectively. Scale bars: 500 μm.

4.3.2 UHR OCT Imaging of Eyes with Retinal Disease

The perceived signal strength and axial resolution was evaluated in eyes with dry AMD and eyes with PDR, where backscattering can be lower than in healthy eyes [21, 22]. Fig. 4.6 shows extracted horizontal and vertical cross-sections as well as the en face projections of 6 mm × 6 mm motion-corrected volumes taken from two eyes with dry AMD—one with drusen, one with geographic atrophy (GA)—and an eye with PDR. These examples represent typical imaging performance of UHR SD-OCT with ReALM in eyes with retinal disease. Note that the ROST

(RIZ), RPE, and BM in (A2, A3) and areas outside of GA lesion in (B2, B3) are not as clearly resolved as in (C2, C3) or in Fig. 4.4. Sharpness of the photoreceptor layer in UHR OCT is further discussed in the following *Imaging of the Photoreceptor Layer* section.

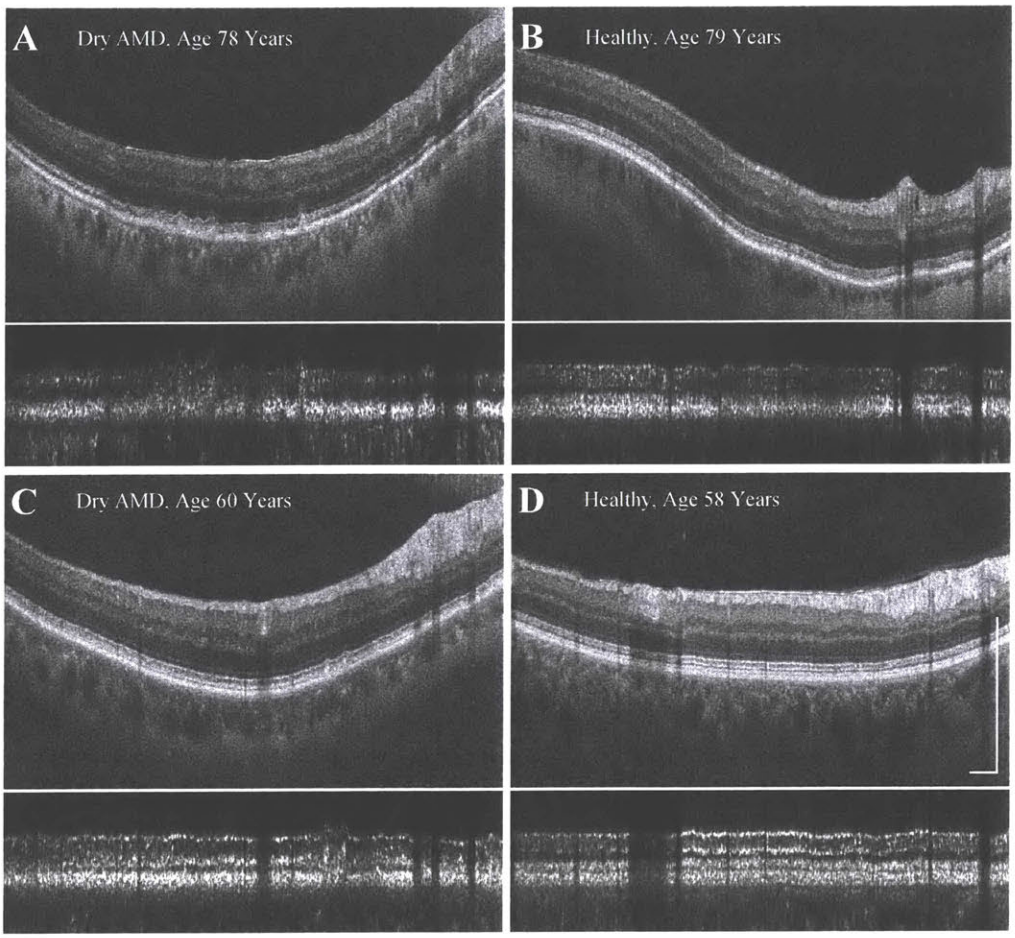

Fig. 4.7. High-density horizontal B-scans at the position 2mm superior to the fovea, taken from 1800×241 raster scans covering 9 mm×6 mm macular area. BM-flattened, amplitude-scale images of a 125 um outer retinal slab shows that the photoreceptor layer tends to be less sharp in the eyes with dry AMD (A, C) compared to the age-matched healthy eyes (B, D). Scale bars: 500 μm.

4.3.3 Photoreceptor Layer Imaging

Imaging of the bright bands in the photoreceptor layer is a potential clinical research application of UHR SD-OCT [23-26]. In order to test the imaging performance of the photoreceptor layer in healthy eyes and in eyes with AMD, we imaged subjects with high-density raster scans with

1800×241 A-scans covering a 9 mm×6 mm area. Fig. 4.7 shows example images from two eyes with dry AMD in parallel with images from age-matched healthy eyes. Amongst the small number of eyes imaged by the UHR instrument, we have observed that the photoreceptor layer structures, especially the three outermost bright bands corresponding to ROST (RIZ), RPE, and BM, were less clearly resolved in the eyes with AMD compared to healthy eyes or eyes with diabetic retinopathy, if the ages of the subjects are similar. Additional comments on photoreceptor layer sharpness are in *Potential Clinical Investigations* section in *Discussion.*

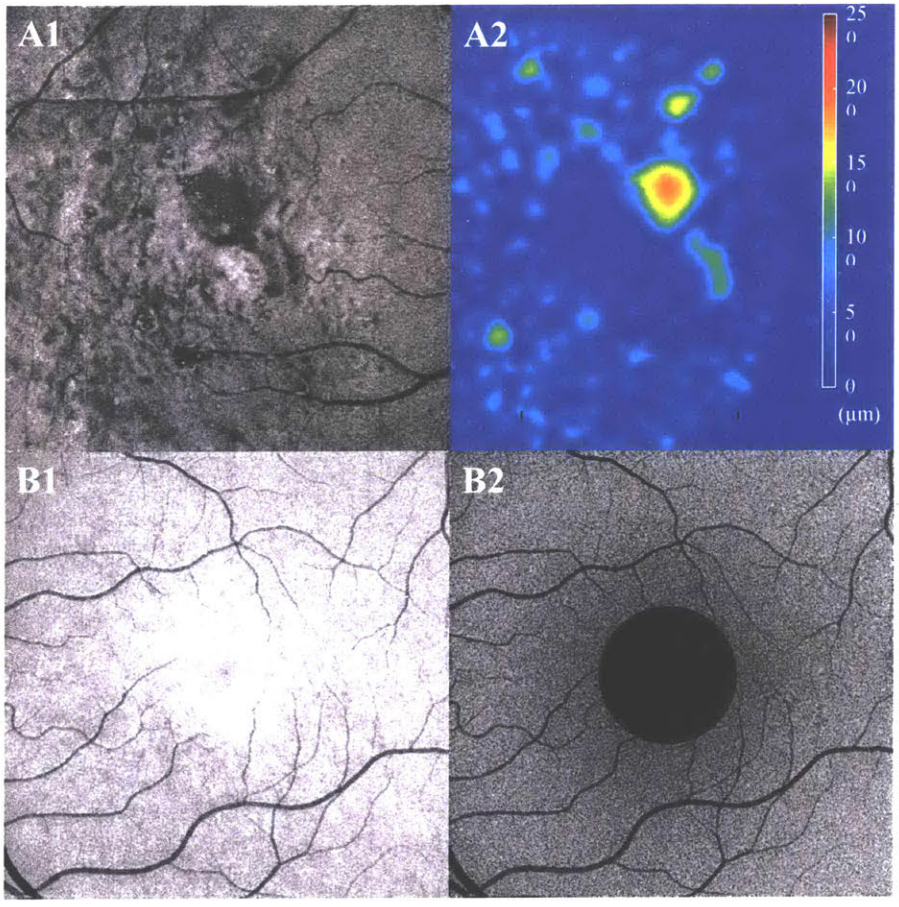

Fig. 4.8. Example of en face image analysis with image segmentation techniques in using 6 mm×6 mm, 500×500-A-scan motion-corrected UHR OCT volumes taken from (A1-A2) an eye with intermediate dry AMD and (B1-B2) a healthy eye. (A1) Mean log amplitude of a 10-μm-thick slab centered at the segmented IS/OS (EZ). (A2) Drusen thickness map calculated as the distance between the segmented RPE and BM. (B1) Mean log amplitude of the signal from COST (CIZ) and (B2) Mean log amplitude of the signal from ROST (RIZ) in a healthy subject.

4.3.4 En Face Image Analysis of Segmented Layers

Accurate outer retinal segmentation combined with motion correction can provide valuable information by generating a series of en face image maps [27-31]. The examples of Fig. 4.8 (A1, A2) show that standard en face analyses such as IS/OS (EZ) signal strength and drusen thickness can be also performed with our prototype in eyes with dry AMD. The examples of Fig. 4.8 (B1, B2) suggest that for healthy eyes or eyes with early dry AMD, intra-photoreceptor-layer bands such as COST (CIZ) and ROST (RIZ) could possibly be segmented to enable various en face analyses.

4.4 Discussion

4.4.1 Advantages of Depth Range Extension using ReALM

As shown in Fig. 4.4 and Fig. 4.5, the variation in the axial position of the retinal image can be reduced using ReALM; this strategy has two, not entirely separate, practical advantages. First, the raster scan procedure is easier from the operator's viewpoint, as the axial alignment of the instrument becomes less sensitive: ReALM removes the need for paying attention to the edge B-scan previews and only requires aligning the retinal image in the central preview to be within the depth range. Second, the signal strength in the deepest part of the retinal image is improved, as the image is generally placed closer to the zero-delay line. These advantages are particularly beneficial for imaging subjects with myopia, astigmatism, or ocular opacity. For the 9 mm×9 mm scan shown in Fig. 4.5, we have observed that the retina, without an extensive alignment procedure, can be positioned in the upper two thirds of the usable depth range of 1.4 mm in tissue. Therefore, the signal roll-off in the retinal image was theoretically less than 5 dB.

While effective depth range extension using ReALM is beneficial for UHR SD-OCT, it may be also applicable to SS-OCT depending on the application. In SS-OCT, the depth range is determined by the tradeoff between electronic factors, such as the sampling rate of the digitizer and the analog bandwidth of the photodetector, and imaging performance factors, such as the axial scan rate and the axial resolution. For SS-OCT instruments developed for applications requiring high A-scan rates and high axial resolutions, the depth range must be compromised, unless the data acquisition electronics are upgraded. ReALM can be useful in these scenarios because it can actively compensate for the retinal curvature to extend effective depth range without changing data acquisition electronics.

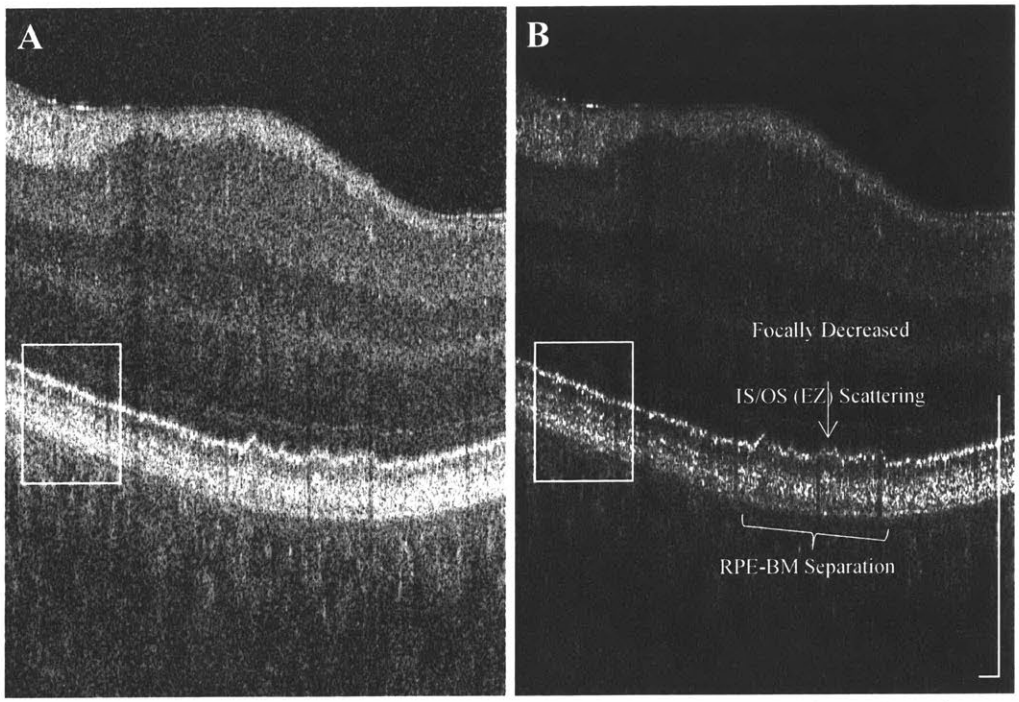

Fig 4.9. Comparison of display scales for UHR OCT images. The same B-scan, extracted from a 6 mm×6 mm, 500×500-A-scan volume taken from an eye with early dry AMD, was plotted in (A) log-of-amplitude scale and (B) amplitude scale. Scale bars: 250 μm.

4.4.2 Image Display Scales

The log-of-amplitude scale is commonly used for viewing retinal OCT images because the amount of backscattering can be orders of magnitude different across different retinal layers. Meanwhile, in Figs. 4.4 and 4.7, BM-flattened, axially magnified, amplitude-scale images were shown in along with the standard log-of-amplitude scale images for enhanced visualization of the outer retina. While the log-of-amplitude scale is well-suited for viewing images with a wide range of signal levels, it is less appropriate than amplitude scale for analyzing fine structures because the signal from highly scattering structures is compressed into a small display range by the logarhithmic curve. In Fig. 4.9, the areas demarcated by the rectangles show that some of the detailed bright band structures observed in the amplitude scale image are not visible in the log-of-amplitude scale image. Furthermore, the small separation between the RPE and BM bands and the focally decreased scattering of the IS/OS (EZ) appear more obvious in the amplitude scale image. Based on our observations, partially shown in Figs. 4.4, 4.7, and 4.9, parallel display of log-of-amplitude-scale images and amplitude-scale images is beneficial for reading UHR OCT images.

4.4.3 Axial Resolution in Motion-Corrected Volumes

Since the preservation of axial resolution is critical for UHR imaging studies, the axial precision of the motion correction technique described in *Methods* must be tested. To evaluate this, we compared the sharpness of the photoreceptor layer in the volumes without motion correction to the resulting motion-corrected volume. In all six healthy eyes, the sharpness of the photoreceptor layer was unaffected by motion correction; Fig. 4.10 shows that in some regions, the averaging step of the motion correction volume actually improved the perceivable sharpness by reducing

speckle noise. However, in order to confirm that the axial resolution is preserved, a systematic analysis on axial point spread functions in individual depth profiles would be needed.

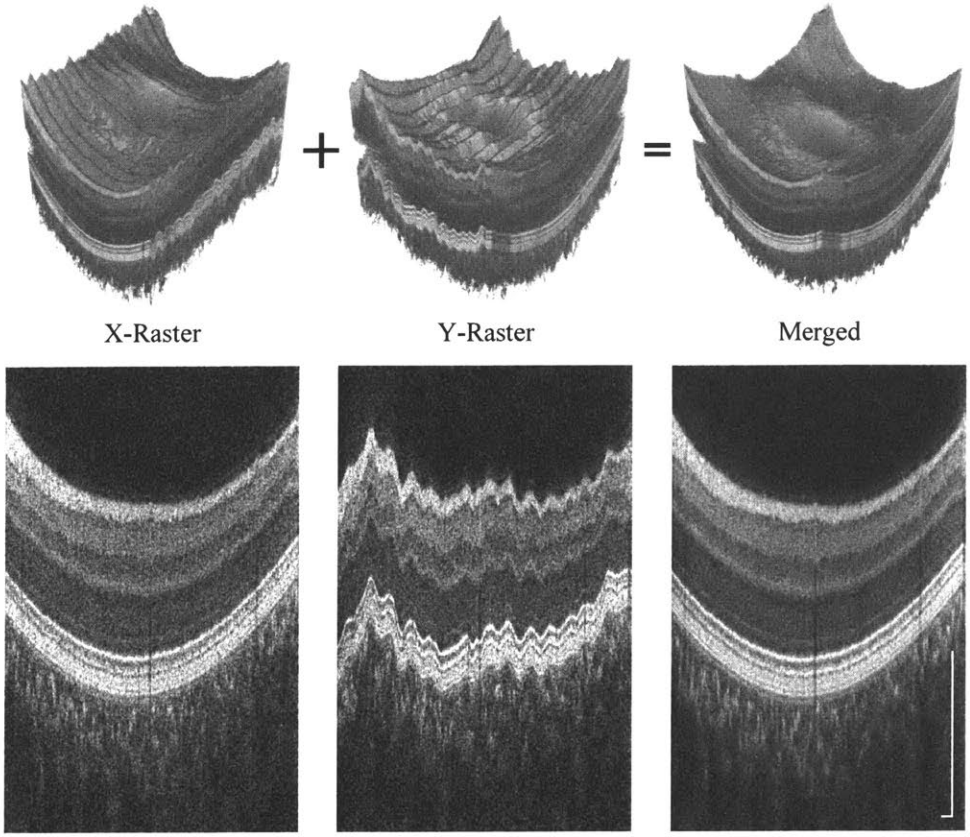

Fig. 4.10. Comparison of the cross-sections from 6 mm×6 mm volumes before and after motion correction. The correction was precise enough to maintain the sharpness of the outer retinal layers. Scale bars: 250 μm.

4.4.4 Comparison between 128 kHz and 250 kHz A-Scan Rates

A healthy eye was imaged at 128 kHz and 250 kHz A-scan rate on the same day to compare the imaging performance of the UHR prototype at the two imaging speeds. The imaging sensitivity at 250 kHz was 99.1 dB, which would be sufficient only for imaging subjects with high ocular transparency and no/negligible astigmatism. While not as robust as 128 kHz for imaging aged subjects, 250 kHz may be useful in a small cohort with high signal strength because high speed

allows denser scanning of the same area or scanning of a wider area. Furthermore, high speed enables blood flow imaging modalities such as OCT angiography (OCTA) and Doppler OCT.

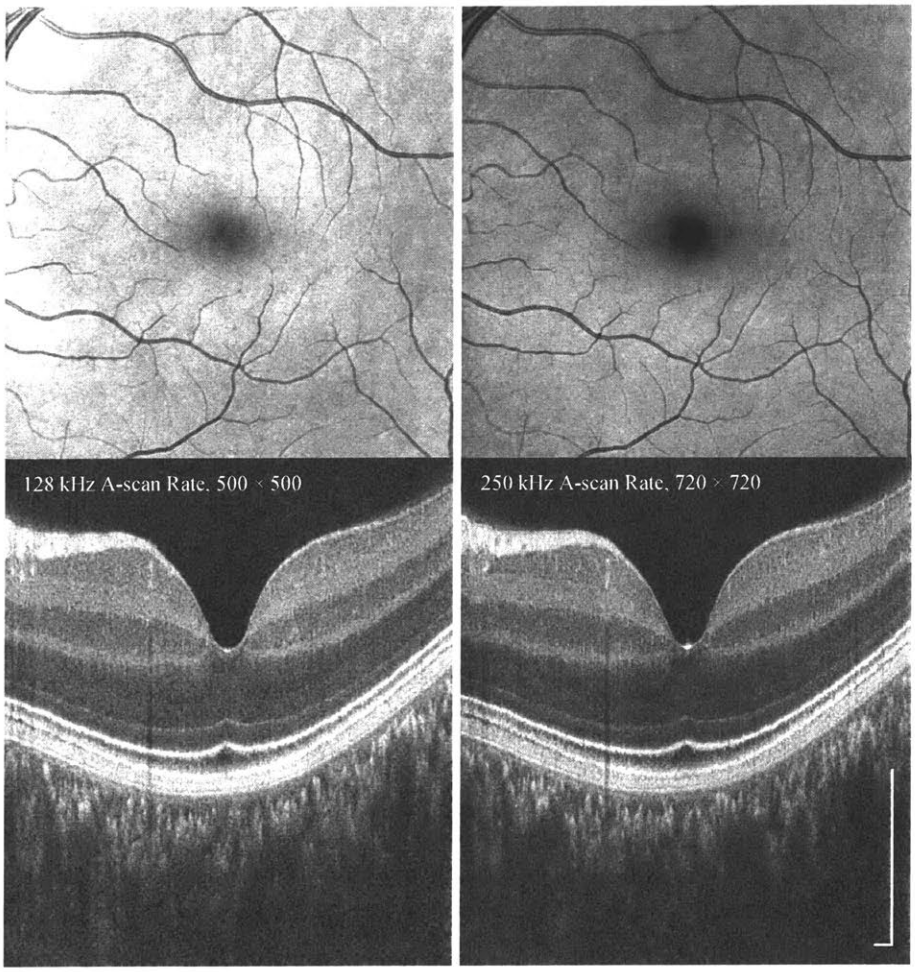

Fig. 4.11. Comparison of motion-corrected volumes acquired at 128 kHz and 250 kHz A-scan rates. A 6 mm×6 mm macular area of a healthy eye was scanned by 500×500 raster scans at 128 kHz A-scan rate and 720×720 raster scans at 250 kHz A-scan rate, respectively. Acquisition time per scan was similar, 2.3 seconds at 128 kHz and 2.4 seconds at 250 kHz. Scale bars: 250 μm.

A 6 mm × 6 mm area was scanned by an orthogonal pair of volumetric raster scans that enabled subsequent motion correction. Each raster scan comprised 500 × 500 A-scans for 128 kHz speed and 720 × 720 for 250 kHz speed, while the acquisition time was roughly matched, namely 2.3 seconds for 128 kHz and 2.4 seconds for 250 kHz. While the B-scans show a noticeable difference in signal strength, the en face projections suggest that the factor of 1.44

advantage in sampling interval is helpful for enhancing the details of lateral structures such as the retinal blood vessels. Furthermore, the extra sampling density may have enhanced the lateral accuracy of motion correction since the algorithm introduces sub-pixel shifts of the A-scan lines into the volume.

4.4.5 Limitations

There are several known limitations of our presented UHR SD-OCT instrument. As mentioned in section 2.1, ReALM's modulation speed is limited by fringe washout, with rapid ReALM introducing non-negligible phase modulation within the integration time of a single A-scan. To avoid this effect, for high B-scan-rate acquisitions, only inter-B-scan ReALM was used. This reduces roughly half of the depth variation caused by the curvature of the retinal image: if we approximate the depth variation, z, of a retinal OCT image by a paraboloid, we may write

$$z = cr^2 = c(x^2 + y^2) = cx^2 + cy^2 = z_x + z_y$$

where r is the distance from the fovea or the center of the scan, and x and y are the lateral coordinates. Then, for x-raster scan of a square area, ReALM compensates only for z_y, the inter-B-scan depth variation; this leaves z_x, the intra-B-scan depth variation, uncompensated. Since the magnitude of the axial variation of the paraboloid is the same in x and y directions, half of the maximum depth variation would remain in the image, if eye motion is excluded. Special scan patterns, such as spirals, are necessary to fully compensate for both z_x and z_y. However, clinical utility of such scan patterns is questionable as a clear approach for motion correction in post-processing is yet to be developed.

The tradeoff between depth range and axial resolution forces the depth range of UHR SD-OCT to be inherently shorter than standard resolution OCT. Therefore, even with ReALM, there

may be instances of insufficient depth range. The fundamental way to increase the depth range without compromising axial resolution is to re-design the spectrometer to have more pixels. Previous implementations of UHR SD-OCT used more than 2048 pixels [8, 26] to maintain depth ranges longer than 2 mm in tissue, although the camera line rate did not reach 128 kHz. Since depth range is related to signal roll-off in SD-OCT, increasing the number of camera pixels and the data width of frame grabbers would be one of the design goals of the future generation hardware for UHR SD-OCT.

Image segmentation algorithms used for generating maps shown in Fig. 4.8 were based on an already existing algorithm for standard-resolution OCT; in order to ensure the segmented layers to be anatomically correct for UHR OCT, the algorithm parameters had to be modified per each individual dataset. Further work must be done to make the segmentation accurate in UHR OCT for a general group of eyes with or without retinal disease, without manually adjusting any parameters. In principle, since there are more axial details revealed in UHR OCT than in standard OCT, the precision of the layer segmentation could be better for UHR OCT than for standard-resolution OCT. Developing a precise layer segmentation algorithm would be critical for both structural en face analytics, such as layer brightness and drusen volume, and functional en face analytics such as the alterations in photoreceptor layer thickness during light or dark adaptation [25, 26].

4.4.6 Potential Clinical Investigations

A recent investigation from our group showed significant changes in the distances between photoreceptor layer bright bands during dark adaptation [26]. The time course of photoreceptor layer thickness, the axial distance from IS/OS (EZ) to BM, were found to be similar to that of

photosensitivity or electrooculogram (EOG). This measurement is particularly important because the recovery of photosensitivity during dark adaptation is hypothesized to be affected in early stages of dry AMD. Therefore, continuing investigation on the response of the photoreceptor layer thicknesses during the process of dark adaptation would be desired.

Amongst the limited number of healthy eyes and the AMD eyes scanned by the UHR instrument, we have observed that the resolvability of the bright bands corresponding to ROST (RIZ), RPE, and BM was diminished in the AMD eyes. One possible hypothesis is that the AMD-associated changes in the rod photoreceptors may have cell-to-cell variance; since the illumination spot size of our UHR OCT instrument is much larger than the lateral extent of the rods, simultaneously illuminating a multitude of rods with anatomical variation would cause blurring and blending of the ROST(RIZ)-RPE-BM complex. However, qualitative remarks on the photoreceptor layer images must be made with caution because the separations between these bands are on the same order of magnitude as the axial resolution. For instance, the sharpness of ROST (RIZ)-RPE-BM complex may seem either different or similar between Fig. 4.7 (B) and (C), depending on the reader. Moreover, it is not safe to assume that the eyes of healthy volunteers, especially the aged ones, are entirely free from AMD-associated changes because subclinical changes undetectable by standard-resolution OCT may be visible in UHR OCT images. A pilot study with a reasonable hypothesis would benefit better understanding of this phenomenon. Since these alterations could be attributed to either normal age-related changes or AMD-specific changes, one of the most immediate studies would be the evaluation of the sharpness of photoreceptor layer in sizable groups of AMD patients and age-matched normal controls. Ultrahigh-lateral-resolution imaging techniques such as adaptive optics OCT [21] may be necessary to reliably estimate the amount of the rod-to-rod anatomical variability and to study

its physiological cause. The feasibility of such measurements, however, must be validated in healthy subjects before planning for subject recruitment.

4.4.7 Summary

We have implemented a UHR SD-OCT instrument which operates at A-scan rates from 80 kHz to 250 kHz. The in-tissue axial resolution in terms of FWHM amplitude was 2.4 μm with raw spectrum and 3.1 μm with spectral shaping. A hardware-software technique, reference arm length modulation (ReALM), was developed to mitigate for the characteristically limited depth range of UHR SD-OCT systems. The instrument could resolve the fine structures in the photoreceptor layer across a wide imaging area. UHR SD-OCT at 128 kHz A-scan rate was validated in a small cohort of healthy eyes and eyes with dry AMD or PDR, and feasibility of 250 kHz A-scan rate UHR SD-OCT was demonstrated in a healthy young subject. High-speed UHR SD-OCT imaging combined with ReALM provides a robust method for motion-corrected UHR imaging of the human retina and thereby opens up possibilities for future studies of the photoreceptor layer in healthy and diseased eyes.

References

[1] W. Drexler, U. Morgner, F. X. Kartner, C. Pitris, S. A. Boppart, X. D. Li, E. P. Ippen, and J. G. Fujimoto, "In vivo ultrahigh-resolution optical coherence tomography," *Opt Lett,* vol. 24, pp. 1221-3, Sep 1 1999.

[2] W. Drexler, U. Morgner, R. K. Ghanta, F. X. Kartner, J. S. Schuman, and J. G. Fujimoto, "Ultrahigh-resolution ophthalmic optical coherence tomography," *Nat Med,* vol. 7, pp. 502-7, Apr 2001.

[3] M. Wojtkowski, V. Srinivasan, T. Ko, J. Fujimoto, A. Kowalczyk, and J. Duker, "Ultrahigh-resolution, high-speed, Fourier domain optical coherence tomography and methods for dispersion compensation," *Opt Express,* vol. 12, pp. 2404-22, May 31 2004.

[4] C. G. Pieroni, A. J. Witkin, T. H. Ko, J. G. Fujimoto, A. Chan, J. S. Schuman, H. Ishikawa, E. Reichel, and J. S. Duker, "Ultrahigh resolution optical coherence tomography in non-exudative age related macular degeneration," *Br J Ophthalmol,* vol. 90, pp. 191-7, Feb 2006.

[5] Y. Chen, L. N. Vuong, J. Liu, J. Ho, V. J. Srinivasan, I. Gorczynska, A. J. Witkin, J. S. Duker, J. Schuman, and J. G. Fujimoto, "Three-dimensional ultrahigh resolution optical coherence tomography imaging of age-related macular degeneration," *Opt Express,* vol. 17, pp. 4046-60, Mar 2 2009.

[6] A. J. Witkin, L. N. Vuong, V. J. Srinivasan, I. Gorczynska, E. Reichel, C. R. Baumal, A. H. Rogers, J. S. Schuman, J. G. Fujimoto, and J. S. Duker, "High-speed ultrahigh resolution optical coherence tomography before and after ranibizumab for age-related macular degeneration," *Ophthalmology,* vol. 116, pp. 956-63, May 2009.

[7] J. Ho, A. J. Witkin, J. Liu, Y. Chen, J. G. Fujimoto, J. S. Schuman, and J. S. Duker, "Documentation of intraretinal retinal pigment epithelium migration via high-speed ultrahigh-resolution optical coherence tomography," *Ophthalmology,* vol. 118, pp. 687-93, Apr 2011.

[8] B. Potsaid, I. Gorczynska, V. J. Srinivasan, Y. Chen, J. Jiang, A. Cable, and J. G. Fujimoto, "Ultrahigh speed spectral / Fourier domain OCT ophthalmic imaging at 70,000 to 312,500 axial scans per second," *Opt Express,* vol. 16, pp. 15149-69, Sep 15 2008.

[9] I. Grulkowski, J. J. Liu, B. Potsaid, V. Jayaraman, C. D. Lu, J. Jiang, A. E. Cable, J. S. Duker, and J. G. Fujimoto, "Retinal, anterior segment and full eye imaging using ultrahigh speed swept source OCT with vertical-cavity surface emitting lasers," *Biomed Opt Express,* vol. 3, pp. 2733-51, Nov 1 2012.

[10] R. Huber, M. Wojtkowski, and J. G. Fujimoto, "Fourier Domain Mode Locking (FDML): A new laser operating regime and applications for optical coherence tomography," *Opt Express,* vol. 14, pp. 3225-37, Apr 17 2006.

[11] E. A. Swanson, J. A. Izatt, M. R. Hee, D. Huang, C. P. Lin, J. S. Schuman, C. A. Puliafito, and J. G. Fujimoto, "In vivo retinal imaging by optical coherence tomography," *Opt Lett,* vol. 18, pp. 1864-6, Nov 1 1993.

[12] M. Wojtkowski, A. Kowalczyk, R. Leitgeb, and A. F. Fercher, "Full range complex spectral optical coherence tomography technique in eye imaging," *Opt Lett,* vol. 27, pp. 1415-7, Aug 15 2002.

[13] H. C. Hendargo, R. P. McNabb, A. H. Dhalla, N. Shepherd, and J. A. Izatt, "Doppler velocity detection limitations in spectrometer-based versus swept-source optical coherence tomography," *Biomed Opt Express,* vol. 2, pp. 2175-88, Aug 1 2011.

[14] W. Choi, B. Baumann, E. A. Swanson, and J. G. Fujimoto, "Extracting and compensating dispersion mismatch in ultrahigh-resolution Fourier domain OCT imaging of the retina," *Opt Express,* vol. 20, pp. 25357-68, Nov 5 2012.

[15] M. F. Kraus, B. Potsaid, M. A. Mayer, R. Bock, B. Baumann, J. J. Liu, J. Hornegger, and J. G. Fujimoto, "Motion correction in optical coherence tomography volumes on a per A-scan basis using orthogonal scan patterns," *Biomed Opt Express,* vol. 3, pp. 1182-99, Jun 1 2012.

[16] M. F. Kraus, J. J. Liu, J. Schottenhamml, C. L. Chen, A. Budai, L. Branchini, T. Ko, H. Ishikawa, G. Wollstein, J. Schuman, J. S. Duker, J. G. Fujimoto, and J. Hornegger, "Quantitative 3D-OCT motion correction with tilt and illumination correction, robust similarity measure and regularization," *Biomed Opt Express,* vol. 5, pp. 2591-613, Aug 1 2014.

[17] D. Huang, Y. L. Jia, S. S. Gao, B. Lumbroso, and M. Rispoli, "Optical Coherence Tomography Angiography Using the Optovue Device," *Oct Angiography in Retinal and Macular Diseases,* vol. 56, pp. 6-12, 2016.

[18] A. Camino, M. Zhang, S. S. Gao, T. S. Hwang, U. Sharma, D. J. Wilson, D. Huang, and Y. Jia, "Evaluation of artifact reduction in optical coherence tomography angiography with real-time tracking and motion correction technology," *Biomed Opt Express,* vol. 7, pp. 3905-3915, Oct 1 2016.

[19] S. J. Chiu, X. T. Li, P. Nicholas, C. A. Toth, J. A. Izatt, and S. Farsiu, "Automatic segmentation of seven retinal layers in SDOCT images congruent with expert manual segmentation," *Opt Express,* vol. 18, pp. 19413-28, Aug 30 2010.

[20] S. J. Chiu, J. A. Izatt, R. V. O'Connell, K. P. Winter, C. A. Toth, and S. Farsiu, "Validated automatic segmentation of AMD pathology including drusen and geographic atrophy in SD-OCT images," *Invest Ophthalmol Vis Sci,* vol. 53, pp. 53-61, Jan 5 2012.

[21] R. De Natale, J. Flammer, M. Zulauf, and T. Bebie, "Influence of age on the transparency of the lens in normals: a population study with help of the Lens Opacity Meter 701," *Ophthalmologica,* vol. 197, pp. 14-8, 1988.

[22] B. E. Klein, R. Klein, and K. L. Linton, "Prevalence of age-related lens opacities in a population. The Beaver Dam Eye Study," *Ophthalmology,* vol. 99, pp. 546-52, Apr 1992.

[23] A. Chan, J. S. Duker, H. Ishikawa, T. H. Ko, J. S. Schuman, and J. G. Fujimoto, "Quantification of photoreceptor layer thickness in normal eyes using optical coherence tomography," *Retina,* vol. 26, pp. 655-60, Jul-Aug 2006.

[24] D. G. Birch, Y. Wen, K. Locke, and D. C. Hood, "Rod sensitivity, cone sensitivity, and photoreceptor layer thickness in retinal degenerative diseases," *Invest Ophthalmol Vis Sci,* vol. 52, pp. 7141-7, Sep 9 2011.

[25] M. D. Abramoff, R. F. Mullins, K. Lee, J. M. Hoffmann, M. Sonka, D. B. Critser, S. F. Stasheff, and E. M. Stone, "Human photoreceptor outer segments shorten during light adaptation," *Invest Ophthalmol Vis Sci,* vol. 54, pp. 3721-8, May 1 2013.

[26] C. D. Lu, B. Lee, J. Schottenhamml, A. Maier, E. N. Pugh, Jr., and J. G. Fujimoto, "Photoreceptor Layer Thickness Changes During Dark Adaptation Observed With Ultrahigh-Resolution Optical Coherence Tomography," *Invest Ophthalmol Vis Sci,* vol. 58, pp. 4632-4643, Sep 1 2017.

[27] F. B. Sallo, T. Peto, C. Egan, U. E. Wolf-Schnurrbusch, T. E. Clemons, M. C. Gillies, D. Pauleikhoff, G. S. Rubin, E. Y. Chew, and A. C. Bird, ""En face" OCT imaging of the

IS/OS junction line in type 2 idiopathic macular telangiectasia," *Invest Ophthalmol Vis Sci,* vol. 53, pp. 6145-52, Sep 14 2012.

[28] R. P. Nunes, G. Gregori, Z. Yehoshua, P. F. Stetson, W. Feuer, A. A. Moshfeghi, and P. J. Rosenfeld, "Predicting the progression of geographic atrophy in age-related macular degeneration with SD-OCT en face imaging of the outer retina," *Ophthalmic Surg Lasers Imaging Retina,* vol. 44, pp. 344-59, Jul-Aug 2013.

[29] C. A. D. Garcia, Z. Yehoshua, G. Gregori, R. P. Nunes, F. M. Penha, A. A. Moshfeghi, K. Zhang, W. Feuer, and P. J. Rosenfeld, "Change in Drusen Volume as a Novel Clinical Trial Endpoint for the Study of Complement Inhibition in Age-related Macular Degeneration," *Ophthalmic Surgery Lasers & Imaging,* vol. 45, pp. 18-31, Jan-Feb 2014.

[30] N. S. Abdelfattah, H. Y. Zhang, D. S. Boyer, P. J. Rosenfeld, W. J. Feuer, G. Gregori, and S. R. Sadda, "Drusen Volume as a Predictor of Disease Progression in Patients With Late Age-Related Macular Degeneration in the Fellow Eye," *Invest Ophthalmol Vis Sci,* vol. 57, pp. 1839-1846, Apr 2016.

[31] Z. Yehoshua, C. A. Garcia Filho, F. M. Penha, G. Gregori, P. F. Stetson, W. J. Feuer, and P. J. Rosenfeld, "Comparison of geographic atrophy measurements from the OCT fundus image and the sub-RPE slab image," *Ophthalmic Surg Lasers Imaging Retina,* vol. 44, pp. 127-32, Mar-Apr 2013.

Chapter 5
Conclusion

5.1 Future Work

5.1.1 Flicker-Induced Changes in TRBF

Comparison of total retinal blood flow (TRBF) before and after application of flicker is a measure representing functional response of retinal vasculature to visual stimuli, often called retinal neurovascular coupling. Since blood-retinal barrier breakdown and retinal ganglion cell changes are characteristics of early diabetic retinopathy (DR), assessment of retinal neurovascular coupling may provide a promising strategy to assess early DR. Numerous studies found that neuroretinal impairment precedes clinically evident DR [1-5]. Compromised neural function in the early diabetic retina was found in multifocal electroretinogram (mfERG) studies, where delays in the first-order implicit times (IT) were associated with diabetes and DR [6, 7] or anticipated subsequent lesions of DR [8]. In a longitudinal study a multivariate analysis on 78 eyes of 41 diabetic patients showed that mfERG IT delays predicted zones of DR development within an average follow-up period of 3 years, with 80% sensitivity and 74% specificity [9]. Since arterial neurovascular response is likely to be compromised both by capillary smooth muscle loss and by neural impairment, numerous studies examined alterations in neurovascular coupling by measuring flicker-induced vascular diameter response with the Dynamic Vessel Analyzer (DVA) [10-15]. These studies demonstrated that flicker-induced vessel response was significantly reduced in diabetic eyes compared with controls and the difference was greater in arteries than in veins. A recent study investigated flicker-induced retinal vessel diameter response measured by the DVA and flow velocity measured by laser Doppler velocimetry in 50 early type 1 diabetic patients compared to 50 age-matched normal controls. Flow velocity

response was 19±7% vs 43±19% (P<0.001) in the diabetic and control groups respectively whereas no significant difference in checkerboard pattern ERG IT was detected [16]. This result suggests that neurovascular response measured by flicker-induced blood flow increase may potentially be more sensitive to early NPDR changes than the neural response measured by pattern ERG IT.

Small scale studies investigated changes in total retinal flow to flicker stimulus using Doppler OCT with circumpapillary scanning and indicated at 22.2% (p=0.004) increase in flow in normal subjects. However, the study had very small enrollment and was limited to normal subjects. In an internal en face Doppler OCT investigation on three healthy young subjects, we have used 8-Hz full-field illumination flicker stimuli to measure 15% to 20% increase in TRBF. Development of efficient and robust experimental protocol to measure flicker-induced TRBF response would lead to clinical studies of retinal neurovascular coupling in early stages of DR. Flicker parameters such as power exposure, duration, frequency, and pattern should be thoroughly experimented in healthy young subjects to determine the optimal flicker settings before scanning patients.

5.1.2 Inter-B-Scan en Face Doppler OCT for Capillary Imaging

En face Doppler OCT for TRBF used inter-A-scan Doppler phase to measure fast-flowing retinal vessels at the optic nerve head. In contrast, en face Doppler OCT using inter-B-scan Doppler phase may be useful for detecting axial flow velocities in certain retinal capillaries, for select applications. One example is detection of flow velocities in feeding and draining vessels in between retinal capillary plexuses. Considering that the inflow and outflow of retinal circulation is centralized at the optic nerve head, the entire retinal blood flow has to be provided from the

large arteries in the superficial capillary plexus and ultimately collected by the large veins in the superior plexus. Inter-plexus arterioles and venules connect the superficial, intermediate, and deep plexuses to assure perfusion in the whole inner retina.

The distinct roles of the three retinal capillary plexuses and their interrelations are not thoroughly understood. Recently proposed was the "hammock" model [17], where the three plexuses are communicating through vertically oriented major arteries and veins that are shown to connect with all three plexuses. The results from recent OCTA investigations using commercial instruments have supported a hypothesis that the deep capillary plexus (DCP) primarily serves as sites of venous outflow [18, 19]. However, these studies had two limitations. First, since OCTA is not sensitive to the direction of the axial flow velocity, they relied on reader interpretations on the determination of flow direction in the capillaries in the DCP. Second, the studies used standard 3 mm × 3 mm and/or 6 mm × 6 mm scans, which may not have sufficient spatial oversampling for analyzing details of microvasculature.

For this particular topic, Doppler phase can be calculated in between adjacent B-scans to set the detectable flow velocity range to on the order of capillary flow velocity (1 mm/s to 5 mm/s). This is only possible with high axial scan rate and rapid scanning of the mirrors over a small area. Both Doppler phase image and OCTA image can be generated and analyzed in en face plane view. The resulting image will reveal both the connectivity among the three plexuses and the blood flow direction in the capillaries in the DCP. Volumetric analysis of inter-B-scan en face Doppler OCT may contribute to advancing the understanding of interrelations among the three retinal capillary plexuses.

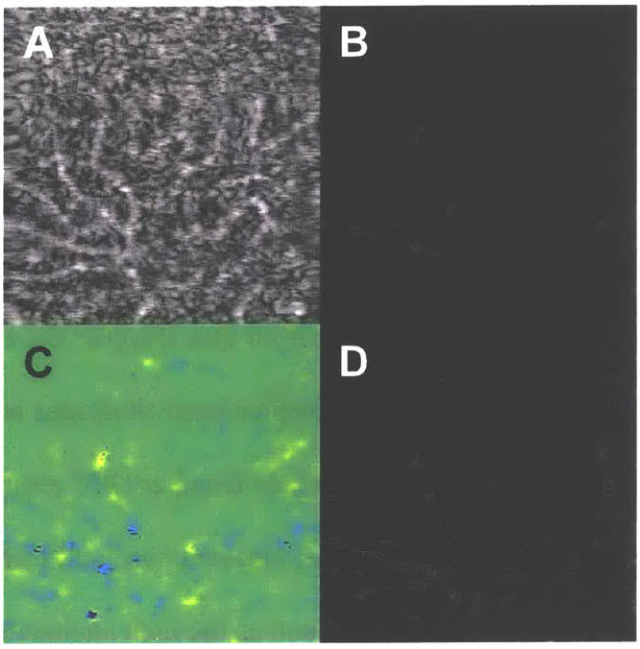

Fig. 5.1. Preliminary results of parallel visualization of the deep plexus using inter-B-scan en face Doppler OCT and OCTA. 500 um 500 um area was scanned with 200 200 A-scans and 10 repeated B-scans at 800 kHz A-scan rate. (A) Log of the mean amplitude. (B) OCTA with 0.35 ms interscan time. (C) en face Doppler OCT with 0.35 ms interscan time. (D) OCTA with 0.7 ms interscan time.

5.1.3 Development of Photoreceptor Metric and Dark Adaptation Imaging Procedures

In subsection 4.3.3, decreased resolvability of the outermost three bands in the photoreceptor layer was mentioned. Qualitative observations on larger groups of AMD patients and age-matched cohorts may suffice for initial validation of this hypothesis. However, in order to perform any systematic, objective investigation on the appearance of intra-photoreceptor-layer bands in UHR OCT, developing automatically evaluated image metrics which represent the integrity of the photoreceptor layer would be critical. Some metrics may aim to represent the photoreceptor layer sharpness while other metrics can be the axial distance from a certain band to another band. Intra-photoreceptor-layer band segmentation software must be enhanced so that it reliably segments the inner segment/outer segment junction (IS/OS), also called the ellipsoid

zone (EZ), and the Bruch's membrane (BM), in healthy and diseased eyes prior to the development of the mentioned image metrics.

5.2 Conclusion

Novel hardware and software technologies such as en face Doppler OCT for measurement of TRBF and UHR OCT for assessment of photoreceptor layer sharpness and its behavior during dark adaptation were described in this thesis. En face Doppler OCT requires deliberately designed processing steps such as the tilted plane, mosaic plane, and NaN-median filtering because of inherent OCT signal characteristics such as the high attenuation in blood and the speckle structure. Results from clinical studies of TRBF validate the software approach in eyes with retinal pathologies. System design choices for UHR OCT sacrifices depth range for axial resolution, raising the need for a method to extend the effective depth range. A hardware-software approach named reference arm length modulation (ReALM), which measures the axial position variation due to the tilt and the curvature of the retinal image and compensates for them with physical modulation of reference arm optical path length, was introduced to solve this problem. Preliminary results in eyes with retinal disease promises potential clinical studies of the photoreceptor layer bands and the time course of their inter-distance in dark adaptation.

Continuing work on improving these new technologies and applying them to clinical studies is desired. The technical details of the described methods have a room can be improved and polished largely because the methods are newly devised and tested only on a small group of patients. Extensive effort on setting appropriate hypotheses and testing them with effective scan protocols would be critical for finding novel early diagnostic markers or surrogate endpoints which can impact the standard of care in ophthalmic practice.

References

[1] A. J. Barber, E. Lieth, S. A. Khin, D. A. Antonetti, A. G. Buchanan, and T. W. Gardner, "Neural apoptosis in the retina during experimental and human diabetes. Early onset and effect of insulin," *J Clin Invest,* vol. 102, pp. 783-91, Aug 15 1998.

[2] E. Lieth, A. J. Barber, B. Xu, C. Dice, M. J. Ratz, D. Tanase, and J. M. Strother, "Glial reactivity and impaired glutamate metabolism in short-term experimental diabetic retinopathy. Penn State Retina Research Group," *Diabetes,* vol. 47, pp. 815-20, May 1998.

[3] E. Lieth, T. W. Gardner, A. J. Barber, and D. A. Antonetti, "Retinal neurodegeneration: early pathology in diabetes," *Clin Exp Ophthalmol,* vol. 28, pp. 3-8, Feb 2000.

[4] M. Mizutani, C. Gerhardinger, and M. Lorenzi, "Muller cell changes in human diabetic retinopathy," *Diabetes,* vol. 47, pp. 445-9, Mar 1998.

[5] W. Whitmire, M. M. Al-Gayyar, M. Abdelsaid, B. K. Yousufzai, and A. B. El-Remessy, "Alteration of growth factors and neuronal death in diabetic retinopathy: what we have learned so far," *Mol Vis,* vol. 17, pp. 300-8, Jan 28 2011.

[6] B. Fortune, M. E. Schneck, and A. J. Adams, "Multifocal electroretinogram delays reveal local retinal dysfunction in early diabetic retinopathy," *Invest Ophthalmol Vis Sci,* vol. 40, pp. 2638-51, Oct 1999.

[7] K. W. Bronson-Castain, M. A. Bearse, Y. Han, M. E. Schneck, S. Barez, and A. J. Adams, "Association between multifocal ERG implicit time delays and adaptation in patients with diabetes," *Invest Ophthalmol Vis Sci,* vol. 48, pp. 5250-5256, Nov 2007.

[8] Y. Han, M. A. Bearse, Jr., M. E. Schneck, S. Barez, C. H. Jacobsen, and A. J. Adams, "Multifocal electroretinogram delays predict sites of subsequent diabetic retinopathy," *Invest Ophthalmol Vis Sci,* vol. 45, pp. 948-54, Mar 2004.

[9] W. W. Harrison, M. A. Bearse, Jr., J. S. Ng, N. P. Jewell, S. Barez, D. Burger, M. E. Schneck, and A. J. Adams, "Multifocal electroretinograms predict onset of diabetic retinopathy in adult patients with diabetes," *Invest Ophthalmol Vis Sci,* vol. 52, pp. 772-7, Feb 2011.

[10] G. Garhofer, C. Zawinka, H. Resch, P. Kothy, L. Schmetterer, and G. T. Dorner, "Reduced response of retinal vessel diameters to flicker stimulation in patients with diabetes," *Br J Ophthalmol,* vol. 88, pp. 887-91, Jul 2004.

[11] T. T. Nguyen, R. Kawasaki, A. J. Kreis, J. J. Wang, J. Shaw, W. Vilser, and T. Y. Wong, "Correlation of light-flicker-induced retinal vasodilation and retinal vascular caliber measurements in diabetes," *Invest Ophthalmol Vis Sci,* vol. 50, pp. 5609-13, Dec 2009.

[12] A. Mandecka, J. Dawczynski, M. Blum, N. Muller, C. Kloos, G. Wolf, W. Vilser, H. Hoyer, and U. A. Muller, "Influence of flickering light on the retinal vessels in diabetic patients," *Diabetes Care,* vol. 30, pp. 3048-52, Dec 2007.

[13] B. Pemp, G. Garhofer, G. Weigert, K. Karl, H. Resch, M. Wolzt, and L. Schmetterer, "Reduced retinal vessel response to flicker stimulation but not to exogenous nitric oxide in type 1 diabetes," *Invest Ophthalmol Vis Sci,* vol. 50, pp. 4029-32, Sep 2009.

[14] A. Lecleire-Collet, I. Audo, M. Aout, J. F. Girmens, R. Sofroni, A. Erginay, J. F. Le Gargasson, S. Mohand-Said, T. Meas, P. J. Guillausseau, E. Vicaut, M. Paques, and P. Massin, "Evaluation of retinal function and flicker light-induced retinal vascular response in normotensive patients with diabetes without retinopathy," *Invest Ophthalmol Vis Sci,* vol. 52, pp. 2861-7, May 2 2011.

[15] G. T. Dorner, G. Garhofer, K. H. Huemer, C. E. Riva, M. Wolzt, and L. Schmetterer, "Hyperglycemia affects flicker-induced vasodilation in the retina of healthy subjects," *Vision Res,* vol. 43, pp. 1495-500, Jun 2003.

[16] M. Lasta, B. Pemp, D. Schmidl, A. Boltz, S. Kaya, S. Palkovits, R. Werkmeister, K. Howorka, A. Popa-Cherecheanu, G. Garhofer, and L. Schmetterer, "Neurovascular dysfunction precedes neural dysfunction in the retina of patients with type 1 diabetes," *Invest Ophthalmol Vis Sci,* vol. 54, pp. 842-7, Jan 30 2013.

[17] J. P. Campbell, M. Zhang, T. S. Hwang, S. T. Bailey, D. J. Wilson, Y. Jia, and D. Huang, "Detailed Vascular Anatomy of the Human Retina by Projection-Resolved Optical Coherence Tomography Angiography," *Sci Rep,* vol. 7, p. 42201, Feb 10 2017.

[18] S. T. Garrity, M. Paques, A. Gaudric, K. B. Freund, and D. Sarraf, "Considerations in the Understanding of Venous Outflow in the Retinal Capillary Plexus," *Retina,* vol. 37, pp. 1809-1812, Oct 2017.

[19] P. L. Nesper and A. A. Fawzi, "Human Parafoveal Capillary Vascular Anatomy and Connectivity Revealed by Optical Coherence Tomography Angiography," *Invest Ophthalmol Vis Sci,* vol. 59, pp. 3858-3867, Aug 1 2018.

List of Publications

[1] Z. Wang, H. C. Lee, O. O. Ahsen, B. Lee, W. Choi, B. Potsaid, J. Liu, V. Jayaraman, A. Cable, M. F. Kraus, K. Liang, J. Hornegger, and J. G. Fujimoto, "Depth-encoded all-fiber swept source polarization sensitive OCT," *Biomedical Optics Express,* vol. 5, pp. 2931-49, Sep 1 2014.

[2] E. Moult, W. Choi, N. K. Waheed, M. Adhi, B. Lee, C. D. Lu, V. Jayaraman, B. Potsaid, P. J. Rosenfeld, J. S. Duker, and J. G. Fujimoto, "Ultrahigh-speed swept-source OCT angiography in exudative AMD," *Ophthalmic Surg Lasers Imaging Retina,* vol. 45, pp. 496-505, Nov-Dec 2014.

[3] B. Lee, W. Choi, J. J. Liu, C. D. Lu, J. S. Schuman, G. Wollstein, J. S. Duker, N. K. Waheed, and J. G. Fujimoto, "Cardiac-Gated En Face Doppler Measurement of Retinal Blood Flow Using Swept-Source Optical Coherence Tomography at 100,000 Axial Scans per Second," *Invest Ophthalmol Vis Sci,* vol. 56, pp. 2522-30, Apr 2015.

[4] G. Liu, O. Tan, S. S. Gao, A. D. Pechauer, B. Lee, C. D. Lu, J. G. Fujimoto, and D. Huang, "Postprocessing algorithms to minimize fixed-pattern artifact and reduce trigger jitter in swept source optical coherence tomography," *Optics Express,* vol. 23, pp. 9824-34, Apr 20 2015.

[5] W. Choi, E. M. Moult, N. K. Waheed, M. Adhi, B. Lee, C. D. Lu, T. E. de Carlo, V. Jayaraman, P. J. Rosenfeld, J. S. Duker, and J. G. Fujimoto, "Ultrahigh-Speed, Swept-Source Optical Coherence Tomography Angiography in Nonexudative Age-Related Macular Degeneration with Geographic Atrophy," *Ophthalmology,* vol. 122, pp. 2532-44, Dec 2015.

[6] D. D. John, C. B. Burgner, B. Potsaid, M. E. Robertson, B. K. Lee, W. J. Choi, A. E. Cable, J. G. Fujimoto, and V. Jayaraman, "Wideband Electrically-Pumped 1050 nm MEMS-Tunable VCSEL for Ophthalmic Imaging," *Journal of Lightwave Technology,* vol. 33, pp. 3461-3468, Aug 15 2015.

[7] E. A. Novais, M. Adhi, E. M. Moult, R. N. Louzada, E. D. Cole, L. Husvogt, B. Lee, S. Dang, C. V. Regatieri, A. J. Witkin, C. R. Baumal, J. Hornegger, V. Jayaraman, J. G. Fujimoto, J. S. Duker, and N. K. Waheed, "Choroidal Neovascularization Analyzed on Ultrahigh-Speed Swept-Source Optical Coherence Tomography Angiography Compared to Spectral-Domain Optical Coherence Tomography Angiography," *American Journal of Ophthalmology,* vol. 164, pp. 80-8, Apr 2016.

[8] M. Lane, E. M. Moult, E. A. Novais, R. N. Louzada, E. D. Cole, B. Lee, L. Husvogt, P. A. Keane, A. K. Denniston, A. J. Witkin, C. R. Baumal, J. G. Fujimoto, J. S. Duker, and N. K. Waheed, "Visualizing the Choriocapillaris Under Drusen: Comparing 1050-nm Swept-Source Versus 840-nm Spectral-Domain Optical Coherence Tomography Angiography," *Invest Ophthalmol Vis Sci,* vol. 57, pp. OCT585-90, Jul 1 2016.

[9] W. Choi, N. K. Waheed, E. M. Moult, M. Adhi, B. Lee, T. De Carlo, V. Jayaraman, C. R. Baumal, J. S. Duker, and J. G. Fujimoto, "Ultrahigh Speed Swept Source Optical Coherence Tomography Angiography of Retinal and Choriocapillaris Alterations in Diabetic Patients with and without Retinopathy," *Retina,* vol. 37, pp. 11-21, Jan 2017.

[10] E. M. Moult, N. K. Waheed, E. A. Novais, W. Choi, B. Lee, S. B. Ploner, E. D. Cole, R. N. Louzada, C. D. Lu, P. J. Rosenfeld, J. S. Duker, and J. G. Fujimoto, "Swept-Source Optical Coherence Tomography Angiography Reveals Choriocapillaris Alterations in

Eyes with Nascent Geographic Atrophy and Drusen-Associated Geographic Atrophy," *Retina,* vol. 36 Suppl 1, pp. S2-S11, Dec 2016.

[11] S. B. Ploner, E. M. Moult, W. Choi, N. K. Waheed, B. Lee, E. A. Novais, E. D. Cole, B. Potsaid, L. Husvogt, J. Schottenhamml, A. Maier, P. J. Rosenfeld, J. S. Duker, J. Hornegger, and J. G. Fujimoto, "TOWARD QUANTITATIVE OPTICAL COHERENCE TOMOGRAPHY ANGIOGRAPHY: Visualizing Blood Flow Speeds in Ocular Pathology Using Variable Interscan Time Analysis," *Retina,* vol. 36 Suppl 1, pp. S118-S126, Dec 2016.

[12] J. Schottenhamml, E. M. Moult, S. Ploner, B. Lee, E. A. Novais, E. Cole, S. Dang, C. D. Lu, L. Husvogt, N. K. Waheed, J. S. Duker, J. Hornegger, and J. G. Fujimoto, "An Automatic, Intercapillary Area-Based Algorithm for Quantifying Diabetes-Related Capillary Dropout Using Optical Coherence Tomography Angiography," *Retina,* vol. 36 Suppl 1, pp. S93-S101, Dec 2016.

[13] B. Lee, E. A. Novais, N. K. Waheed, M. Adhi, T. E. de Carlo, E. D. Cole, E. M. Moult, W. Choi, M. Lane, C. R. Baumal, J. S. Duker, and J. G. Fujimoto, "En Face Doppler Optical Coherence Tomography Measurement of Total Retinal Blood Flow in Diabetic Retinopathy and Diabetic Macular Edema," *Jama Ophthalmology,* vol. 135, pp. 244-251, Mar 1 2017.

[14] C. D. Lu, B. Lee, J. Schottenhamml, A. Maier, E. N. Pugh, Jr., and J. G. Fujimoto, "Photoreceptor Layer Thickness Changes During Dark Adaptation Observed With Ultrahigh-Resolution Optical Coherence Tomography," *Invest Ophthalmol Vis Sci,* vol. 58, pp. 4632-4643, Sep 1 2017.

[15] E. D. Cole, E. M. Moult, S. Dang, W. Choi, S. B. Ploner, B. Lee, R. Louzada, E. Novais, J. Schottenhamml, L. Husvogt, A. Maier, J. G. Fujimoto, N. K. Waheed, and J. S. Duker, "The Definition, Rationale, and Effects of Thresholding in OCT Angiography," *Ophthalmol Retina,* vol. 1, pp. 435-447, Sep-Oct 2017.

[16] C. B. Rebhun, E. M. Moult, E. A. Novais, C. Moreira-Neto, S. B. Ploner, R. N. Louzada, B. Lee, C. R. Baumal, J. G. Fujimoto, J. S. Duker, N. K. Waheed, and D. Ferrara, "Polypoidal Choroidal Vasculopathy on Swept-Source Optical Coherence Tomography Angiography with Variable Interscan Time Analysis," *Transl Vis Sci Technol,* vol. 6, p. 4, Nov 2017.

[17] A. H. Skalet, Y. Li, C. D. Lu, Y. Jia, B. Lee, L. Husvogt, A. Maier, J. G. Fujimoto, C. R. Thomas, Jr., and D. Huang, "Optical Coherence Tomography Angiography Characteristics of Iris Melanocytic Tumors," *Ophthalmology,* vol. 124, pp. 197-204, Feb 2017.